Application and method development in computational systems biology: Petri nets to study knockouts and dynamics of *Salmonella* infection

Dissertation
zur Erlangung des Doktorgrades
der Naturwissenschaften
im Fach Bioinformatik

vorgelegt beim Fachbereich Informatik und Mathematik
der Johann Wolfgang Goethe-Universität
in Frankfurt am Main

von
Jennifer Hannig
aus Mannheim

Frankfurt (2018)
(D 30)

vom Fachbereich Informatik und Mathematik der

Johann Wolfgang Goethe - Universität als Dissertation angenommen.

Dekan:	Prof. Dr. Andreas Bernig
Gutachter:	Prof. Dr. Ina Koch
	Prof. Dr. Dr. Ivan Dikic

Datum der Disputation: 25.10.2018

Abstract

Antimicrobial resistance became a serious threat to the worldwide public health in this century. A better understanding of the mechanisms, by which bacteria infect host cells and how the host counteracts against the invading pathogens, is an important subject of current research and will encourage the development of new therapeutic treatments of bacterial infections. Intracellular bacteria of the *Salmonella* genus have been frequently used as a model system for bacterial infections. *Salmonella* are ingested by contaminated food or water and cause gastroenteritis and typhoid fever in animals and humans. Once inside the gastrointestinal tract, *Salmonella* can invade intestinal epithelial cells by the induction of membrane ruffles, which enclose bacteria in vesicles named *Salmonella*-containing vacuoles. A fraction of these bacteria disrupts their vacuoles and enters the host cytosol. The host cell can fight against intracellular pathogens by a process called xenophagy. For complex systems, such as processes involved in the bacterial infection of cells, computational systems biology provides approaches to describe mathematically how these intertwined mechanisms in the cell function. Computational systems biology allows the analysis of biological systems at different levels of abstraction. Functional dependencies as well as dynamic behavior can be studied. In this thesis, we used the Petri net formalism to gain a better insight into bacterial infections and host defense mechanisms and to predict cellular behavior that can be tested experimentally. We also focused on the development of new computational methods.

In this work, the first realization of a mathematical model of the xenophagic capturing of *Salmonella enterica* serovar Typhimurium in epithelial cells was developed. The existing literature provided a rich repertoire of

molecular interactions and functional mechanisms. We manually compiled these multiple data into a consensus model to obtain a holistic representation of how the bacterium is recognized and targeted for xenophagic degradation. The mathematical model expressed in the Petri net formalism was constructed in an iterative way of modeling and analyses. During the Petri net development, we found a missing part in the knowledge about the regulation of xenophagic capturing. So far, the source of TBK1 activation has not been enlightened, though TBK1 seems to play an important role in xenophagy. To fill this gap in the understanding of the pathway, we suggested a new mechanism of TBK1 activation upon *Salmonella* infection, assuming an autoactivation of TBK1 regulated by high local concentration. For the model verification, we analyzed the Petri net, including a computational performance of knockout experiments named *in silico* knockouts, which was established in this work. The *in silico* knockouts of the proposed Petri net are consistent with the published experimental perturbation studies and, thus, ensures the biological credibility of the Petri net. *In silico* knockouts that have not been experimentally investigated yet provide hypotheses for future investigations of the pathway.

To study the dynamic behavior of an epithelial cell infected with *Salmonella enterica* serovar Typhimurium, a stochastic Petri net was constructed. In experimental research, a decision like "Which incubation time and multiplicity of infection is needed to infect half of the epithelial cells with *Salmonella*?" is based on experience or practicability. A mathematical model can help to answer these questions and improve experimental design. The stochastic Petri net models the cell at different stages of the *Salmonella* infection, including the invasion of *Salmonella* into the epithelial cells by a cooperative strategy and the bacterial proliferation in the cytosol and the *Salmonella*-containing vacuole. Moreover, the xenophagic degradation of cytosolic bacteria was included. We parameterized the model by a set of experimental data derived from different literature sources. The kinetic parameters of the stochastic Petri net determine the time evolution of the bacterial infection of a cell. The model captures the stochastic variation and heterogeneity of the cytosolic and vacuolar *Salmonella* population of a single cell over time. For some infected cells, the Petri net predicts the

success of xenophagy by capturing all cytosolic bacteria, and for other cells, xenophagy is predicted to fail. The high proportion of vacuolar bacteria in the first period of the infection becomes outnumbered by fast-replicating, cytosolic bacteria at later stages of the infection. The model can be applied to predict experimental parameters. For example, the stochastic Petri net predicted the infection efficiency of epithelial cells with *Salmonella*, depending on the two factors, incubation time and multiplicity of infection. Thus, the model generated valuable information for future experiments to study *Salmonella* infections. Furthermore, we provided first estimations for the kinetic parameters of the different processes involved in *Salmonella*-infected cells. The stochastic Petri net is a valuable tool to examine the dynamics of *Salmonella* infections in epithelial cells.

In the last part of this thesis, a novel theoretical method was introduced to perform knockout experiments *in silico*. Experimental manipulation through gene knockout or knockdown experiments has been frequently and widely used to reveal the functional dependencies of signaling pathways. The new concept of *in silico* knockouts is based on the computation of signal flows at steady state and allows the determination of knockout behavior that is comparable to experimental perturbation behavior. In this context, we established the concept of Manatee invariants and demonstrated the suitability of their application for *in silico* knockouts by reflecting biological dependencies from the signal initiation to the response. As a proof of principle, we applied the proposed concept of *in silico* knockouts to the Petri net of the xenophagic recognition of *Salmonella enterica* serovar Typhimurium in epithelial cells. To enable the application of *in silico* knockouts for the scientific community, we implemented the novel method in the software isiKnock. isiKnock allows the automatized performance and visualization of *in silico* knockouts in signaling pathways expressed in the Petri net formalism. In conclusion, the knockout analysis provides a valuable method to verify computational models of signaling pathways, to detect inconsistencies in the current knowledge of a pathway, and to predict unknown pathway behavior.

In summary, the main contributions of this thesis are the Petri net of the xenophagic capturing of *Salmonella enterica* serovar Typhimurium in epithelial cells to study the knockout behavior and the stochastic Petri net

of an epithelial cell infected with *Salmonella enterica* serovar Typhimurium to analyze the infection dynamics. Moreover, we established a new method for *in silico* knockouts, including the concept of Manatee invariants and the software isiKnock to automatically perform *in silico* knockouts. The results of these studies are useful to a better understanding of bacterial infections and provide valuable model analysis techniques for the field of computational systems biology.

Zusammenfassung

In diesem Jahrhundert wurden Antibiotika-Resistenzen zu einer zunehmenden Bedrohung der öffentlichen Gesundheit auf der ganzen Welt. Die bakteriellen Erreger verändern sich ständig und werden gegen immer mehr Medikamente resistent. Ein wichtiger Aspekt der aktuellen Forschung ist, die Prozesse der bakteriellen Infektion in Wirtszellen sowie deren Verteidigungsstrategien gegen eingedrungene Pathogene zu untersuchen. Ein besseres Verständnis dieser Mechanismen wird die Entwicklung neuer therapeutischer Behandlungen gegen bakterielle Infektionen fördern und ist somit ein wichtiger Beitrag im Kampf gegen die Antibiotika-Resistenz von Bakterien.

Ein ideales Modellsystem für die Erforschung bakterieller Infektionen ist das häufig verwendete, intrazelluläre Bakterium *Salmonella*. Bakterien der Gattung *Salmonella* werden durch kontaminierte Nahrung oder Wasser aufgenommen und verursachen bei Tieren und Menschen Gastroenteritis und Typhus. Sobald Salmonellen in den Magen-Darm-Trakt gelangen, können sie in die Epithelzellen des Darms eindringen. Hierbei kommt es zu einer bakteriell-induzierten Umorganisation des Cytoskeletts der Wirtszelle. Es bilden sich wellenförmige Aufwerfungen der Zellmembran, sogenannte *Ruffle*. Salmonellen werden von diesen Membranaufwerfungen umflossen und sind folglich in Vesikeln, den *Salmonella*-beinhaltenden Vakuolen, eingeschlossen. Bei einem Teil dieser vakuolären Bakterien kommt es zu einem Aufbrechen der *Salmonella*-beinhaltenden Vakuolen und die Salmonellen dringen in das Cytosol der Zelle vor. Im Cytosol finden die Salmonellen optimale Lebensbedingungen vor, wie ausreichend Nährstoffe und einen neutralen pH-Wert. Bei diesen Lebensbedingungen können sich die Bakterien

mit hohen Raten replizieren. Ein Verteidigungsmechanismus der Wirtszelle gegen intrazelluläre Pathogene ist die sogenannte antibakterielle Autophagie oder auch Xenophagie.

Für komplexe Prozesse, wie sie beispielsweise bei der bakteriellen Infektion vorzufinden sind, liefert das Forschungsgebiet der theoretischen Systembiologie Ansätze. Mit Hilfe der theoretischen Systembiologie kann mathematisch beschrieben werden, wie diese ineinandergreifenden Mechanismen der Bakterien und des Wirts in der Zelle funktionieren. Die theoretische Systembiologie ermöglicht die Analyse von biologischen Systemen auf unterschiedlichen Abstraktionsebenen. Sowohl funktionale Abhängigkeiten eines Signalwegs als auch dynamisches Verhalten kann erforscht werden. In dieser Arbeit wurde der Petri-Netz-Formalismus angewendet, um ein besseres Verständnis der bakteriellen Infektion und der Abwehrmechanismen der Wirtszellen zu erhalten und um zelluläres Verhalten vorherzusagen. Ein weiterer Fokus der Arbeit lag auf der Entwicklung neuer computergestützter Methoden für die Systembiologie.

Das in dieser Arbeit erstellte Petri-Netz repräsentiert ein erstes mathematisches Modell der Erkennung von *Salmonella enterica* serovar Typhimurium für den xenophagischen Abbau in Epithelzellen. Die vorhandene Literatur liefert ein großes Repertoire an molekularen Interaktionen und funktionalen Mechanismen dieses Prozesses. Um ein ganzheitliches Bild der Erkennung von *Salmonellen* für den xenophagischen Abbau zu erhalten, wurden die zahlreichen Informationen aus der Literatur manuell zusammengetragen. Das Modell beinhaltet die Ubiquitinierung von Salmonellen im Cytosol, die Bindung der sogenannten Autophagie-Rezeptoren NDP52, OPTN und p62 zwischen der autophagosomalen Membran und den Ubiquitinketten am Bakterium oder Galectin-8 an der aufgebrochenen Membran der *Salmonella*-beinhaltenden Vakuole sowie regulatorische Prozesse. Bei der Modellentwicklung konnten Lücken im Verständnis über die Regulationsmechanismen der xenophagischen Erkennung aufgedeckt werden. Bisher wurde die Quelle der TBK1-Aktivierung noch nicht gefunden, obwohl die Kinase TBK1 eine wichtige Rolle bei der Xenophagie zu spielen scheint. Um diese Lücke im Verständnis des Signalwegs zu schließen, wurde in dieser Arbeit ein neuer Mechanismus der TBK1-Aktivierung vorgeschlagen. Die Ver-

mutung ist, dass es zu einer Autoaktivierung von TBK1 kommen kann, die durch eine hohe lokale Konzentration von TBK1 reguliert wird. Zur Modell-Verifikation wurde das Petri-Netz analysiert. Hierbei wurde unter anderem eine computergestützte Vorhersage von Knockout-Experimenten etabliert und angewendet, die sogenannte *in silico* Knockout-Analyse. Die Vorhersagen der *in silico* Knockout-Analyse stimmen mit den publizierten experimentellen Knockout-Studien überein. Diese Übereinstimmung unterstreicht die biologische Glaubwürdigkeit des Petri-Netz-Modells. Vorhersagen der *in silico* Knockout-Analyse, die noch nicht durch ein entsprechendes experimentelles Pendant in der Literatur untermauert wurden, liefern Hypothesen für zukünftige Experimente.

Um das dynamische Verhalten einer mit Salmonellen infizierten Zelle zu untersuchen, wurde ein stochastisches Petri-Netz erstellt, das die Infektion von *Salmonella enterica* serovar Typhimurium in Epithelzellen beschreibt. Entscheidungen in der experimentellen Forschung, wie beispielsweise "Wie lange sollte die Inkubationszeit und die Multiplizität der Infektion sein, um die Hälfte der Epithelzellen mit Salmonellen zu infizieren?" basieren in der Regel auf Erfahrungswerten oder Durchführbarkeit der Experimente. Ein mathematisches Modell einer Salmonellen-infizierten Zelle kann dabei helfen, diese Fragen zu beantworten und somit die experimentelle Planung zu verbessern. Das stochastische Petri-Netz modelliert die Epithelzelle zu verschiedenen Stadien der Infektion mit Salmonellen. Dieses beinhaltet das Landen und Abheben von Salmonellen auf der Oberfläche der Epithelzelle, die Invasion von Salmonellen in Epithelzellen an den *Ruffle* durch einen kooperativen Effekt, sowie die Replikation von Salmonellen im Cytosol und den *Salmonella*-beinhaltenden Vakuolen. Des Weiteren beschreibt das Modell die Zerstörung von cytosolischen Bakterien mittels Xenophagie. Darüber hinaus wurden experimentelle Vorgänge in das Modell integriert, wie die Inkubation von den zu infizierenden Epithelzellen mit dem Infektionsmedium zu unterschiedlichen Multiplizitäten der Infektion und das Wegwaschen des Infektionsmediums nach einer festgelegten Zeitdauer. Für die Bestimmung der kinetischen Parameter des stochastischen Petri-Netz-Modells wurden experimentelle, zeitaufgelöste Daten aus unterschiedlichen Literaturquellen verwendet. Mit Hilfe der kinetischen Parameter des Modells konnte

die zeitliche Entwicklung der bakteriellen Infektion in einer Epithelzelle simuliert werden. Das Modell ist in der Lage, die stochastische Variation und Heterogenität der cytosolischen und vakuolären Salmonellen-Population in einer einzelnen Zelle über die Zeit zu erfassen und abzubilden. Das intrazelluläre Wachstum ist ein Produkt der vakuolären und der cytosolischen Proliferation. Der hohe Anteil an vakuolären Salmonellen in der ersten Phase der Infektion wird durch schnell replizierende Salmonellen im Cytosol zu späteren Zeitpunkten der Infektion zahlenmäßig übertroffen. Für einige der infizierten Epithelzellen wurde vorhergesagt, dass mittels Xenophagie alle Salmonellen im Cytosol zerstört wurden. Wiederrum in anderen Epithelzellen ist es nicht gelungen, das Cytosol von sich schnell teilenden Salmonellen zu befreien. Das stochastische Petri-Netz der Infektion von Salmonellen in Epithelzellen kann zur Vorhersage experimenteller Parameter verwendet werden. Zum Beispiel wurde die Infektionseffizienz von Salmonellen in Epithelzellen in Abhängigkeit von den Faktoren Inkubationszeit und Multiplizität der Infektion vorhergesagt. Dies sind wichtige Informationen für die Planung von Experimenten. Darüber hinaus wurden erste Abschätzungen der kinetischen Parameter für die verschiedenen Prozesse der Salmonellen-Infektion gegeben. Insgesamt stellt das Modell ein wertvolles Werkzeug zur Untersuchung und Vorhersage der Dynamik der Salmonellen-Infektion in Epithelzellen dar.

Im Rahmen dieser Arbeit wurde eine neue Methode der *in silico* Knockout-Analyse vorgestellt. Die experimentelle Manipulation von Genen und deren Produkten mittels Knockout- oder Knockdown-Experimenten wird häufig genutzt, um die funktionalen Abhängigkeiten eines Signalwegs aufzudecken. Die Bestimmung von Komponenten des Signalwegs, auf die das System besonders sensitiv reagiert, oder die Vorhersage der Auswirkung eines Knockouts auf die Komponenten, sind besonders wichtige Anhaltspunkte, um das Wissen über den Signalweg zu verbessern und um damit beispielsweise neue Ansätze für die therapeutische Behandlung zu erlangen. Die Methode der *in silico* Knockout-Analyse basiert auf der Berechnung von Signalflüssen im Gleichgewichtszustand und erlaubt die Vorhersage des Verhaltens nach einem Knockout, das mit experimentellem Knockout-Verhalten vergleichbar ist. In diesem Zusammenhang wurde das Konzept der so-

genannten Manatee-Invarianten entwickelt. Mittels Manatee-Invarianten können die biologischen Abhängigkeiten von der Initiierung zur Zellantwort eines Signalwegs aufgedeckt werden. Deshalb eignen sich Manatee-Invarianten besonders zur Verwendung bei der *in silico* Knockout-Analyse. Die *in silico* Knockout-Analyse stellt eine wertvolle Methode zur Aufdeckung von Widersprüchlichkeiten im aktuellen Kenntnisstand über einen Signalweg dar. Durch den Vergleich von experimentellem und vorhergesagtem Knockout-Verhalten können Inkonsistenzen erkannt werden. Des Weiteren erlauben *in silico* Knockout-Analysen die Vorhersage von unbekanntem Systemverhalten und unterstützen somit die experimentelle Planung. Als *Proof-of-Principle* für das in dieser Arbeit vorgestellte Konzept der *in silico* Knockout-Analyse wurde die Methode auf das Petri-Netz zur Erkennung von Salmonellen für die Zerstörung mittels Xenophagie angewendet. Um die Anwendung der *in silico* Knockout-Analyse für weitere biologische Fragestellungen zu ermöglichen, wurde die neue Methode in der Software isiKnock implementiert. isiKnock bietet eine grafische Benutzeroberfläche für eine nutzerfreundliche Bedienung und ermöglicht die automatisierte Durchführung und Visualisierung der *in silico* Knockout-Analyse für Signalwege, die im Petri-Netz-Formalismus beschrieben sind. Hierbei können sowohl einzelne Komponenten eines Signalwegs als auch mehrere Komponenten auf einmal ausgeschaltet werden. Darüber hinaus bietet die Software die Möglichkeit der Manatee-Invarianten-Analyse.

Zusammenfassend sind die Hauptbestandteile dieser Arbeit das Petri-Netz-Modell der Erkennung von Salmonellen für den xenophagischen Abbau in Epithelzellen zur Analyse des Knockout-Verhaltens und das stochastische Petri-Netz-Modell einer mit Salmonellen infizierten Epithelzelle zur Vorhersage des dynamischen Verhaltens. Zudem wurde eine neue Methode für *in silico* Knockout-Analysen entwickelt, einschließlich des Konzepts der Manatee-Invarianten und der Software isiKnock zur automatisierten Durchführung von *in silico* Knockout-Analysen. Die Ergebnisse dieser Studien tragen zu einem besseren Verständnis der bakteriellen Infektion bei. Darüber hinaus wurden wertvolle Methoden zur Modellanalyse im Bereich der theoretischen Systembiologie vorgestellt.

Contents

List of Figures

List of Tables

Nomenclature

AA	amino acid
ARIH1	ariadne RBR E3 ubiquitin protein ligase 1
Atg8	autophagy-related protein 8
ATG13	autophagy-related protein 13
ATG101	autophagy-related protein 101
BRENDA	BRaunschweig ENzyme DAtabase
CPI	covered by place invariants
CRISPR	clustered regularly interspaced short palindromic repeats
CSV	comma-separated values
CTI	covered by transition invariants
DAG	diacylglycerol
DUB	deubiquitinating enzyme
EFM	elementary flux mode
FIP200	focal adhesion kinase family interacting protein of 200 kD
GABARAP	γ-aminobutyric acid receptor-associated protein
GUI	graphical user interface

h	hours
HOIP	HOIL-1-interacting protein
IEC	intestinal epithelial cell
INA	Integrated Net Analyzer
K	lysine
KEGG	Kyoto Encyclopedia of Genes and Genomes
LAMP1	lysosomal-associated membrane protein 1
LAP	LC3-associated phagocytosis
LC3	microtubule-associated protein 1 light chain 3
LIR	LC3-interacting region
LPS	lipopolysaccharides
LRSAM1	leucine-rich repeat and sterile α motif-containing 1
MCT-sets	maximal common transition sets
MEF	mouse embryonic fibroblasts
min	minutes
mLST8	mammalian lethal with SEC13 protein 8
MOI	multiplicity of infection
mTOR	mammalian target of rapamycin
mTORC1	mammalian target of rapamycin complex 1
M1	N-terminal methionine
NAP1	NAK-associated protein 1
NDP52	nuclear dot protein 52
NF-κB	nuclear factor-κB

OPTN	optineurin
OTULIN	OTU deubiquitinase with linear linkage specificity
PN	Petri net
PNG	portable network graphics
PPI	protein-protein interaction
p.i.	post infection
P/T net	place/transition net
P-invariant	place invariant
Raptor	regulatory-associated protein of mTOR
Salmonella Typhi	*Salmonella enterica* serovars Typhi
Salmonella Typhimurium	*Salmonella enterica* serovars Typhimurium
SBML	systems biology markup language
SCV	*Salmonella*-containing vacuole
sec	seconds
shRNA	small hairpin ribonucleic acid
siGal8	siRNA against galectin-8
siLRSAM1	siRNA against LRSAM1
siNDP52	siRNA against NDP52
SINTBAD	similar to NAP1 TBK1 adaptor
siRNA	small interfering ribonucleic acid
siTBK1	siRNA against TBK1
SPI-1	*Salmonella* pathogenicity island-1
SPI-2	*Salmonella* pathogenicity island-2

SPN	stochastic Petri net
SSA	stochastic simulation algorithm
SVG	scalable vector graphics
TALEN	transcription activator-like effector nucleases
TAX1BP1	Tax1-binding protein 1
TBK1	TANK-binding kinase 1
TLR4	Toll-like receptor 4
T3SS	type III secretion system
T6SS	type VI secretion system
T-invariant	transition invariant
UBAN	ubiquitin binding in ABIN and NEMO
ULK1	uncoordinated 51-like kinase 1

Chapter 1

Introduction

This chapter is divided into five parts and intends to give an introduction and motivation to the topics of this thesis, which focuses on the application and development of theoretical methods in computational systems biology. The aim of the first part is to introduce the biological application – the bacterial infection with *Salmonella*. The importance of research on this pathogen as a model system for bacterial infections is highlighted. The next part provides an introduction and motivation to computational systems biology. The third part gives an overview of the state of the art in the research fields. Current methods to perform *in silico* knockouts are discussed and their limitations are highlighted. Moreover, existing mathematical models of biological processes associated with *Salmonella* infections and autophagy are presented. The fourth part emphasizes the aim of the work. The course of this thesis is pointed out in the last part.

1.1 *Salmonella* infection

Gram-negative bacteria of the *Salmonella* genus have been frequently used as an exemplary model organism to study the general mechanisms involved in bacterial infections [1, 2]. Most *Salmonella* infections are self-limited diseases, i.e., no medical treatment is required. However, in infants, elderly, or immunocompromised patients, severe invasive infections with *Salmonella* occur that require antibiotic treatment [3]. Antimicrobial-resistance of *Salmo-*

nella has increased over recent decades and became a serious health problem, especially in endemic developing countries with limited treatment options [4, 5].

Salmonella infections are caused by contaminated food or water and are responsible for millions of infections and thousands of deaths across the world every year [6, 7]. The most common clinical syndromes associated with *Salmonella* infections are enteric fever and gastroenteritis. In human, the typhoidal *Salmonella enterica* serovars Typhi (*Salmonella* Typhi) and Paratyphi cause enteric fever. Gastroenteritis is induced in human by many non-typhoidal *Salmonella enterica* serovars, such as Enteritidis and Typhimurium (*Salmonella* Typhimurium). Additionally, *Salmonella* Typhimurium is responsible for an illness, resembling enteric fever in inbred mouse strains and thus serves as a suitable model organism to study host-pathogen interactions.

After oral intake, bacteria pass through the gastrointestinal tract where they encounter the anatomical barrier of the intestinal epithelium, see Figure 1.1. *Salmonella* Typhimurium can enter epithelial cells of the intestine by deforming the epithelial membrane, a process named membrane ruffling [8]. The membrane ruffles enclose the invading bacteria and form the vacuolar membrane surrounding the bacterium termed the *Salmonella*-containing vacuole (SCV) [9]. The SCV is a specialized intracellular compartment and constitutes a replication niche for the bacterium. Most of the bacteria stay inside the protective enclosing of the SCV. However, a small fraction disrupts its vacuolar membrane and inhabits the host cell cytosol, as shown in tissue culture and inbred mouse strains [10–14]. *Salmonella* Typhimurium inside the cytosol proliferates at higher rates than inside the surrounding membrane of the SCV [11, 14–17]. For an overview of the significant host responses that are triggered by *Salmonella* infections, we refer to Coburn *et al.* and de Jong *et al.* [18, 19].

The host cells can capture and eliminate intracellular pathogens by autophagy, a process that has been termed xenophagy and is also known as antibacterial autophagy [20–24]. In general, macroautophagy (thereafter called autophagy) is a conserved cellular process, which is characterized by lysosomal degradation of cytosolic components, such as protein aggregates and

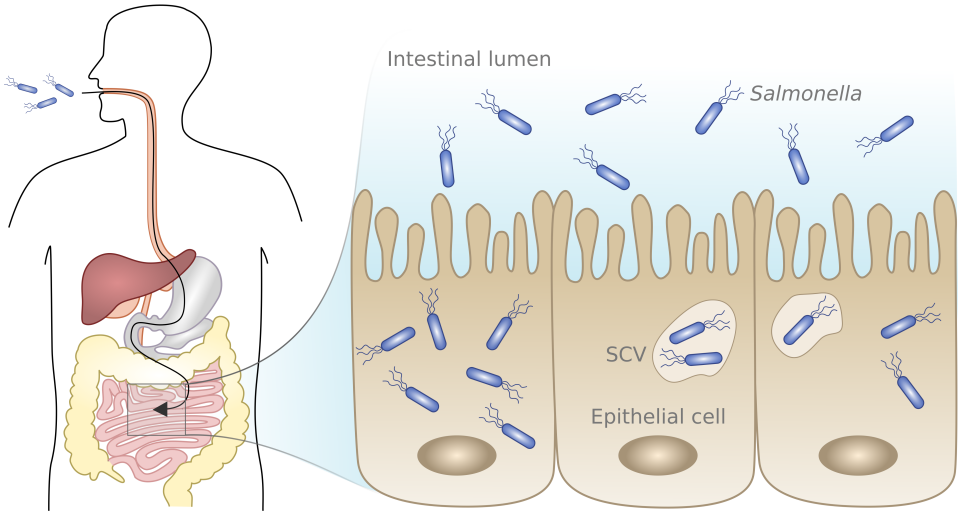

Figure 1.1 ***Salmonella*** **infection.** After oral intake, the bacteria of the *Salmonella* genus come to the gastrointestinal tract. Here, the bacteria infiltrate epithelial cells of the intestinal epithelium. Inside epithelial cells, the bacterium is enclosed by the vacuolar membrane of the SCV. The disruption of the SCV leads to the escape of *Salmonella* into the cytosol.

damaged organelles [25–27]. The cytosolic cargo is engulfed by an isolated membrane termed phagophore or autophagosomal membrane [28]. The autophagosomal membrane elongates and forms a double-membrane compartment termed autophagosome. The autophagosome can fuse with lysosomes, resulting in the destruction of the cargo. This process requires autophagy receptors, proteins that bridge the binding between the cargo and the autophagosomal membrane [29–31]. Inside the host cell, the bacteria gets coated by ubiquitin chains [12]. The attachment of ubiquitin to a substrate is known as ubiquitination [32,33] and is a type of post-translational modification, like phosphorylation and acetylation. Ubiquitination is controlled by the cooperation of three types of enzymes, E1 ubiquitin-activating enzymes, E2 ubiquitin-conjugating enzymes, and E3 ubiquitin-protein ligases. The ubiquitin moieties can form chains via the linkage of the seven lysine (K) residues K6, K11, K27, K29, K33, K48, and K63 or the N-terminal methionine (M1) called linear linkage. The labeling of intracellular bacteria with ubiquitin leads to their recognition by the autophagic machinery [12,34]. In cell culture and in mice, xenophagy has been reported to repress the dissemination of cytosol-invaded *Salmonella* [30, 31, 34–36]. Also, other bacteria

have been demonstrated to be recognized by xenophagy, such as *Streptococcus pyogenes* [37] and *Mycobacterium tuberculosis* [38]. The xenophagy pathway has recently been discovered, and a better understanding of the molecular mechanisms, by which bacteria are captured and destructed, may lead to novel hints of potential therapeutic treatment of bacterial infectious diseases.

1.2 Computational systems biology

Computational systems biology deals with the mathematical modeling of biological systems, such as signaling pathways, metabolic pathways, or gene regulatory networks [39]. Biological systems are complex and intertwined events composed of multiple interacting and dependent components. The main aim of computational systems biology is to describe, how these molecular mechanism in the cell function, and to predict cellular behavior that can be tested experimentally.

There are different modeling approaches available, depending on the biological question, the availability of information, and the desired level of detail. Kinetic models are typically based on systems of ordinary differential equations and can be used to simulate the behavior of the system over time [40, 41]. For kinetic modeling, a rather detailed knowledge of concentrations and kinetic parameters is necessary, but this information is often sparse, especially for signaling pathways. For this purpose, kinetic modeling is only suitable for processes of a manageable size that are well-understood and with known kinetic data. For example, a kinetic model of substrate ubiquitination and its deubiquitination has been constructed to study the substrate discrimination by deubiquitinating enzyme (DUB) activity [42].

For many signaling pathways, a growing amount of molecular interactions and functional mechanisms are known. Here, mathematical models can capture the mechanistic insights and the relationships between the pathway components, which are highly dependent and intertwined. A promising modeling approach that is based on graph theory and focuses on the network topology is the Petri net (PN) formalism. PN has been developed to model systems of concurrent, nondeterministic processes. The PN formalism based

on a well-founded mathematical theory provides well-established analysis techniques [43, 44]. PN offer the advantage of revealing information about the dynamic behavior and even quantitative properties of a biological system without any prior kinetic knowledge. For example, the analysis of transition invariants (T-invariants) reveals functional modules that act at steady state [45]. The intuitive graphical representation of PN simplifies the dialog between experimental and theoretical researchers. Furthermore, PN can be extended by quantitative data of concentrations and kinetic parameters, thus supporting hybrid modeling [46]. Since the first application of PN for a metabolic pathway by Reddy *et al.* [47], PN have been increasingly used to model and simulate biological systems. Besides metabolic pathways [47–53], PN have been successfully applied to signaling pathways [54–58] and gene regulatory networks [59, 60].

In summary, computational systems biology is of particular importance for testing conditions that are too elaborate or unsuitable to test experimentally. The models can be used to improve experimental design and to generate testable predictions. Additionally, mathematical models help to organize and interpret existing experimental data to detect inconsistencies and gaps in the present knowledge of the biological system and to predict the system's behavior.

1.3 State of the art

1.3.1 Computational systems biology of *Salmonella* infection and autophagy

In the field of bacterial infections with *Salmonella*, many mathematical models have been published, applying different computational approaches. An overview about systems biological modeling of the metabolism of *Salmonella* inside the host cells has been provided by Dandekar *et al.*, including flux balance analyses and elementary flux modes approaches [61]. For example, the metabolic network of *Salmonella* Typhimurium has been reconstructed by a community-based approach [62]. Recently, a proteomic study combined with a protein-protein interaction (PPI) network has been presented by Fiskin *et*

al., providing a global view of the ubiquitinome of the host and the bacterium in response to infections with *Salmonella* Typhimurium [63]. A PPI network based on gene expression data of human peripheral blood from patients infected with *Salmonella* Typhi, other bacterial infections, or leukemia (non-infected) has been proposed by Dhal *et al.* [64]. A Gene Ontology enrichment analysis [65] and graph theoretical methods has been applied to identify *Salmonella* Typhi-specific hubs and subnetworks. Das *et al.* presented a Boolean network of the communication between the three pathogenicity islands located in the genome of *Salmonella*, type VI secretion system (T6SS), type III secretion system (T3SS) encoded by *Salmonella* pathogenicity island-1 (SPI-1), and T3SS encoded by *Salmonella* pathogenicity island-2 (SPI-2) [66]. A kinetic model has been presented to study several strategies of *Salmonella* Typhimurium accumulation in solid tumors [67]. To investigate the distribution of the bacterial amount within a host cell population, a stochastic model has been published by Brown *et al.* [68]. Grant *et al.* constructed a stochastic model to investigate the dynamics of bacterial growth over the first days of an acute *Salmonella* infection in mice [69].

Plenty of studies have been presented to investigate the quantitative microbial behavior in food – the field of predictive microbiology [70–74]. For an overview of mathematical modeling in predictive microbiology, see McMeekin *et al.* and McDonald *et al.* [75,76]. The aim of this research area is to objectively evaluate the food quality with respect to their contamination by microorganisms.

For the infection of *Salmonella* in epithelial cells two mathematical models have been presented so far. Firstly, Misselwitz *et al.* presented a model to study different strategies of target site selection by *Salmonella* Typhimurium [77]. The model simulates *Salmonella* Typhimurium as linear moving particles in a three dimensional landscape, including a spherical object, which is partially immersed into a flat surface. Misselwitz *et al.* demonstrated that the accumulation of particles on the spherical object can be achieved by the strategy of swimming in close proximity to the surface called *near surface swimming*. The second model describes the invasion of *Salmonella* Typhimurium in epithelial cells and is based on a system of ordinary differential equations [78]. Five basic steps of *Salmonella* invasion

have been considered in the model: attachment to the cell, formation of ruffles, attachment to a ruffle, invasion via SCV, and the vacuolar escape. The presented model reproduces experimental measurements and thus provides a valuable model to study the complex processes of bacterial infection. The proliferation of bacteria in the cytosol and the SCV as well as the effects of xenophagy on bacterial replication have not been included in the model. The low number of invaded bacteria in a single cell causes significant stochastic effects and leads to a high heterogeneity in the bacterial population between individual cells [16, 17, 77, 79]. Deterministic models, such as a system of ordinary differential equations, fail to predict the variability of the bacterial population. Only stochastic models can capture the variations in bacterial growth at the single-cell level.

In the research field of autophagy, particularly, PPI networks have been applied reviewed by Ng [80]. Behrends *et al.* presented a global autophagy interaction network by a proteomic analysis and the usage of existing protein interaction databases [81]. Recently, Kramer *et al.* have introduced a procedure of progressive iterations of data integration, hierarchical modeling, and the generation of new data, which they called *Active Interaction Mapping* [82]. The method has been applied to the autophagy pathway. The outcome was a hierarchical PPI network of the autophagy process.

With regard to the xenophagic capturing of *Salmonella*, to our knowledge, no computational systems biology approach has been presented so far. Today, *Salmonella* Typhimurium is one of the best studied model organism for xenophagic recognition. The existing literature provides a rich repertoire of molecular interactions and functional mechanisms of this pathway and thereby offers an ideal basis for the development of a mathematical model.

1.3.2 *In silico* knockouts and other Petri net analysis techniques

A common practice, when studying the functionality of signaling pathways, is to perform genetic perturbations, such as gene knockouts or knockdowns. For an overview of experimental perturbation strategies, such as small in-

terfering ribonucleic acid (siRNA), small hairpin ribonucleic acid (shRNA), transcription activator-like effector nucleases (TALEN), and the clustered regularly interspaced short palindromic repeats (CRISPR)/Cas9, we refer to Yao *et al.* [83]. The identification of components, to which the pathway is particularly sensitive or insensitive and the prediction of how a perturbation can affect the system, are important issues to improve the knowledge of the pathway and to reveal, e.g., unexpected aspects of potential therapeutic treatments. The computational performance of perturbation experiments, here after called *in silico* knockouts, provides an opportunity to predict the biological dependencies of the pathway components.

The first knockout analysis of a model in the PN formalism has been applied by Grunwald *et al.* in 2008 to investigate the Duchenne muscular dystrophy [59]. The general concept says that if a reaction of a PN is not functional, i.e., knocked out, all T-invariants that contain the knocked out reaction are affected and are not functional at steady state. The impact of a reaction on the network can be measured by the number of T-invariants the reaction is part of. The software MonaLisa performs knockouts and visualizes the affected T-invariants [84]. Additionally, Grunwald *et al.* have introduced a new data structure and visualization of T-invariants in form of a binary tree called *Mauritius maps* [59]. Mauritius maps clearly display the impact of reactions on the network in case of a knockout and the dependencies of T-invariants.

Similar to the knockout of reactions, maximal common transition sets (MCT-sets) has been knocked out [51,59,85]. MCT-sets are sets of reactions that exclusively participate in a set of T-invariants [54]. In Minervini *et al.*, a PN of the pathways of the Von Hippel-Lindau tumor suppressor has been presented and *in silico* knockouts have been performed [51]. Besides the knockout based on T-invariants or MCT-sets, simulations have been used to analyze knockout behavior of the regulation of angiogenesis [85].

Similar to the concept of T-invariants is the concept of elementary flux modes (EFM) [45,86,87] and extreme pathways [88] in traditional biochemical modeling. For a detailed comparison between T-invariants and EFM, we refer to Zevedei-Oancea *et al.*, Schuster *et al.* and Voss *et al.* [52,89–91]. A comparison between EFM and extreme pathways is given by Klamt *et al.*

and Palsson *et al.* [92, 93]. EFM and extreme pathways are predominantly applied to metabolic pathways [86, 87, 94–99]. Wilhem *et al.* have introduced the term *structural robustness* of metabolic pathways based on the determination of EFM [100]. The measure of structural robustness is based on the ratio of the number of EFM in the baseline situation and the number of EFM after the knockout. Structural robustness has been intensively studied [101–106]. A similar concept is the fragility coefficient introduced by Klamt and Gilles [107]. The fragility coefficient of a biological component is the reciprocal of the mean size of all minimal cut sets in which the component is part of. Minimal cut sets are based on EFM and can be considered as the smallest group of reactions in the network, whose simultaneous knockout ensures the breakdown of an objective reaction [107].

All these attempts, T-invariants, EFM, or extreme pathways, are based on structural network properties and reaction stoichiometries. They aim to decompose the network into functional modules at steady state [45]. These modules do not necessarily function independently of the rest of the network. The knockout analysis based on structural network properties and reaction stoichiometry reveals dependencies between these modules. However, the functional modules, defined by T-invariants, EFM, or extreme pathways, do not necessarily yield the biological causal dependencies of a pathway from its initiation to the response. The inability of EFM to reflect causal dependencies has been previously described by Klamt *et al.* [108]. The detection of all signal flows from the receptor initiation to the cell response in signaling pathways is still a challenge. In consequence, the results of *in silco* knockouts using the existing methods are not comparable with experimental perturbation data derived from gene knockout or knockdown experiments. Questions like "Which effects on the pathway would have a selective removal of pathway components by siRNA?" can not be answered by these approaches, because they do not reveal the biological functional dependencies. Sackmann *et al.* have introduced the concept of feasible T-invariants [54], which aims to find signal flows in signaling pathways by the combination of T-invariants.

Beside the analysis of structural network properties, *in silico* knockouts are broadly applied to logical models to analyze gene regulatory net-

works [109–111]. For logical models, various software tools exist to perform *in silico* knockouts, e.g., GINsim [112] and BooleanNet [113]. Another graph-theoretical approach to study biological systems are interaction graphs [114]. Interaction graphs are directed graphs with positive and negative interactions. A limitation of interaction graphs is their inability to model logical AND relations. Klamt *et al.* introduced the dependency matrix [108, 115], which is based on the calculation of shortest paths of an interaction graph. The dependency matrix is a graphical representation that illustrates the pairwise dependencies between the network components. The software CellNetAnalyzer can be applied to analyze the dependencies of interaction graphs [115]. The analysis of interdependencies has been applied, e.g., to the T cell receptor signaling pathway [116] and the EGFR/ErbB signaling pathway [117]. The matrix representation is an appropriate graphical display of the effects of perturbations and has been frequently used in computational systems biology [108, 118] as well as in experimental systems biology [119].

The reverse approach, to infer the network topology based on experimental perturbations, has been a subject of many studies [120, 121]. For comprehensive reviews about network inference, we refer to Albert [122] and Markowetz and Spang [123]. The approaches often rely on methods based on Bayesian networks. The bottleneck of these methods is the requirement of a huge amount of data and the complexity of network inference caused by the combinatorial explosion of the search space, meaning possible network structure [124].

1.4 Aim of the work

The main aim of this thesis was to investigate processes that are involved in bacterial infections using computational systems biology approaches. In this context, one focus was the development of novel computational methods in systems biology.

The first objective of this work was the realization of a PN of the xenophagic capturing of *Salmonella*. The compilation of the known reactions into one network gives a holistic mathematical representation of

the pathway. To the best of our knowledge, no mathematical model has been presented so far, describing the process of the xenophagic capturing of *Salmonella*. The construction and analysis of the model will highlight gaps in the state-of-the-art knowledge of the pathway and aims to improve the understanding. Particularly, the analysis of *in silico* knockouts can verify the correctness and consistency of the PN model and will provide hypothesis for future experiments. A better insight about the mechanisms involved in this key defense pathway can help to counteract against antimicrobial resistance.

A further aim of this thesis was to investigate the dynamic behavior of *Salmonella* infection in epithelial cells by a stochastic PN model. A bulk of experimental studies exists, quantifying the intracellular bacterial population. These data enable the development of mathematical models to predict and examine the population dynamics. Due to the high variability of the intracellular bacterial population in the cytosol and the SCV, non-deterministic models, such as stochastic PN, are particularly suitable to capture the stochastic nature of bacterial proliferation on the single cell level. Such a stochastic model of a *Salmonella*-infected cell can be applied as a tool to improve experimental design and to gain insights into intracellular population dynamics.

Another goal of this work was to postulate a novel concept of *in silico* knockouts that considers the biological dependencies of signaling pathways. The available approaches to perform *in silico* knockouts do not necessarily predict effects that are comparable with experimental perturbations. For the *in silico* knockout analysis, the effects of knockouts on the steady-state behavior of the model has to be considered and a mathematical concept is required for the identification of all possible signal flows in signaling pathways. Predictions of *in silico* knockout behavior that can be compared with experimental perturbation studies will provide a worthwhile method to verify the topology of the network and to predict unknown knockout behavior for the network validation by future experimental investigations. In this context, a further objective of this work was the development of a software to provide the automatized prediction of *in silico* knockout behavior for the scientific community.

1.5 Course of the work

The thesis is divided into five chapters. Chapter 1 provides an introduction and a motivation to the topic of bacterial infection with *Salmonella* and to the field of computational systems biology. Here, an overview is given of the state of the art of academic research in these areas, and the aims of this work are set. Chapter 2 presents the basic concept of the PN formalism and thus provides the theoretical background of the thesis. Chapter 3 gives a short explanation about the processes involved in model construction, the experimental data used in this thesis, and the applied software is listed. Chapter 4 presents and discusses the results of this work and is divided into three major parts. First, the PN of the xenophagic capturing of *Salmonella* is presented and analyzed. In this context, the current view of the xenophagic capturing of *Salmonella* is summarized and discussed. The second part is concerned with the stochastic model of a *Salmonella*-infected cell. The last part deals with the method development of this thesis. Here, the proposed method of *in silico* knockout, the concept of Manatee invariants, and a software for the automatized prediction of knockout behavior are presented. Chapter 5 concludes the thesis with a summary of the results and an outlook for future research.

Chapter 2

Theoretical Background

The aim of this chapter is to provide the methodical background of this thesis. First, we introduce the basic concepts and terms of *place/transition nets* (P/T nets) and discuss the interpretation of P/T nets in a biological context. We used the abbreviation PN as a synonym for a P/T net. The next part presents an extension of the classic PN formalism, the stochastic PN and its stochastic simulation by Gillespie's stochastic simulation algorithm. The following descriptions are based on the books by Koch *et al.* [43], Starke [125], Reisig [126], Wilkinson [127], and Ingalls [128].

2.1 Petri net formalism

PN were originally developed by Carl Adam Petri in the 1960s [129]. There are several reviews and books, which describe PN and their analysis [43, 44, 125, 126]. In the following, we focus on the basic concepts and terms that are relevant to this thesis. PN are directed, bipartite graphs and can be mathematically defined as the quintuple $PN = (P, T, F, W, M_0)$, where

P $= \{p_1, ..., p_m\}$ is a set of nodes,
T $= \{t_1, ..., t_n\}$ is a set of nodes, where P and T are disjunct sets,
F $\subseteq (P \times T) \cup (T \times P)$ is a set of arcs (p, t) or (t, p), where $p \in P$ and $t \in T$,
W : $F \to \mathbb{N}$ is a function that attaches a positive, non-zero integer number to each arc $f \in F$, its *arc weight*,

$M_0 : P \to \mathbb{N}_0$ is the *initial marking*, which matches each place p a number of marks called *tokens*, $M_0(p)$.

The elements of P and T are called *places* and *transitions*, respectively. An arc connects a place with a transition and *vice versa*, but no arc exists between two nodes of the same set. An arc pointing in both directions, from a transition to a place and from the place back to the transition is called *read arc*.

A *pre-transition* of a place p is a transition connected with place p by an arc, pointing from the transition to the place. Accordingly, a *post-transition* of a place p is a transition connected with place p through an arc in the opposite direction, starting at the place p and pointing towards the transition. The set of pre- and post-transitions of a place p are defined by

$$\bullet p = \{t \in T | (t,p) \in F\}, \text{and } p\bullet = \{t \in T | (p,t) \in F\},$$

respectively. Analogously to the definition of pre- and post-transitions, the set of *pre-places* and *post-places* of a transition t are indicated by

$$\bullet t = \{p \in P | (p,t) \in F\}, \text{and } t\bullet = \{p \in P | (t,p) \in F\},$$

respectively. A transition with only pre-places and no post-places is called *input transition*. In contrast, a transition with only post-places and no pre-places is termed *output transition*. Transitions that are neither input nor output transitions are named *inner* transitions.

Tokens represent discrete objects held by the places of the PN. The number of tokens on a place p defines the marking of the place p and is denoted by

$$M(p) : P \to \mathbb{N}_0.$$

The resulting distribution of tokens over all places is defined as the *marking* M of the PN. The marking defines a certain *state* i of the PN. The PN state with an initial marking M_0 is called *initial state*. In a *sequence of steps* the marking of the PN can change. A sequence of steps is defined by

$$M_0 \xrightarrow{s_1} M_1 \xrightarrow{s_2} M_2 \xrightarrow{s_3} ... \xrightarrow{s_n} M_n,$$

while $M_{i-1} \xrightarrow{s_i} M_i$, $i = 1, 2, ..., n$ is a step. A *step* or *simulation step* can be interpreted as the occurrence or the *firing* of a transition. A marking M is termed *reachable marking* if there is a sequence of steps to transform the initial marking M_0 to M. Another name for a sequence of steps is the *simulation* or *animation* of the PN. A transition t has the opportunity to fire in a given marking, i.e., is *enabled* or *activated* if the pre-places of t carry at least as many tokens as indicated by the weight of the connecting arcs, meaning $W(\bullet t, t) \leq M(\bullet t)$. It follows that a transition t is *disabled* or *inactivated* if $W(\bullet t, t) > M(\bullet t)$. For a given marking of a place at state i, $M_i(p)$, the firing of an enabled transition t results in the marking

$$M_{i+1}(p) = \begin{cases} M_i(p) - W(p,t) + W(p,t), & \text{if } p \in \bullet t \text{ and } p \in t\bullet, \\ M_i(p) - W(p,t), & \text{if } p \in \bullet t \text{ and } p \notin t\bullet, \\ M_i(p) + W(p,t), & \text{if } p \notin \bullet t \text{ and } p \in t\bullet, \\ M_i(p), & \text{otherwise.} \end{cases}$$

The firing of a transition results in the consumption of the tokens on its pre-places and the generation of tokens on its post-places, according to the weights of the respective arcs. This "token flow" of "token game" reflects the dynamic behavior of the system.

The graphical representation of a PN is depicted in Figure 2.1. The places are depicted as circles, the transitions as rectangles, and the tokens as dots or numbers on the places. The arcs of a PN are illustrated as arrows assigned by integer number corresponding to the arc weights. If no number is indicated, the arc weight is one.

The places *P1* and *P2* are the pre-places of transition *T1* and the places *P3* and *P4* are the pre-places of transition *T2*. In the initial marking, both transitions are enabled and can fire one time. In Figure 2.1, an exemplary sequence of steps is depicted. Upon the firing of transition *T1*, two tokens on place *P1* and one token on place *P2* are removed according to the arc weights. One token on place *P5* and two tokens on place *P6* are generated, resulting in the PN in the marking M_1, see Figure 2.1B. Transition *T1* is disabled and *T2* is still enabled. The firing of transition *T2* removes three

tokens on place *P3* and two tokens on place *P4* and produces one token on place *P6*, see the PN in the marking M_2 in Figure 2.1C. Now, the simulation ends after two simulation steps, because both transitions, *T1* and *T2*, are disabled. Another sequence of steps from $M_0 \rightarrow M_2$ would be first the firing of transition *T2* and then the firing of transition *T1*.

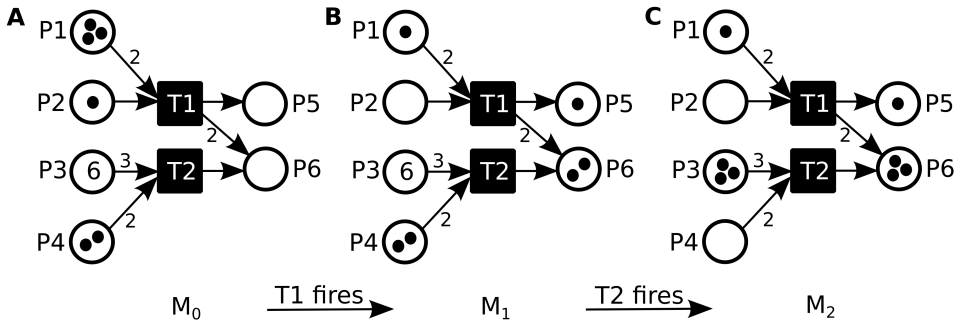

Figure 2.1 Graphical representation of a PN and its firing. The PN is defined by the set of places $P = \{P1, P2, P3, P4, P5\}$, the set of transitions $T = \{T1, T2\}$, the set of arcs $F = \{(P1, T1), (P2, T1), (P3, T2), (P4, T2), (T1, P5), (T1, P6), (T2, P6)\}$, and the multiset of weights $W = \{2, 1, 3, 2, 1, 2, 1\}$. (A) The PN in the initial marking $M_0 = \{3, 1, 6, 2, 0, 0\}$. Transition *T1* and *T2* are both enabled. (B) The transition T1 has fired, resulting in a new marking $M_1 = \{1, 0, 6, 2, 1, 2\}$. Transition *T1* is enabled and transition *T2* is disabled. (C) The transition T2 has fired, resulting in a new marking $M_2 = \{1, 0, 3, 0, 1, 3\}$. Transition *T1* and *T2* are both disabled.

2.2 Petri net analysis

There exist many methods to analyze PN, thanks to their well-defined mathematical representation [43, 44, 125, 126]. The topology of a PN with the transitions $t_1, ..., t_j, ..., t_n$ and the places $p_1, ..., p_i, ..., p_m$ can be expressed by a two-dimensional matrix C called the *incidence matrix*

$$C = \begin{array}{c} \\ p_1 \\ \vdots \\ p_i \\ \vdots \\ p_m \end{array} \begin{array}{c} \begin{array}{cccccc} t_1 & \dots & t_j & \dots & t_n \end{array} \\ \begin{pmatrix} z_{1,1} & \dots & z_{1,j} & \dots & z_{1,n} \\ \vdots & \vdots & \vdots & \vdots & \vdots \\ z_{i,1} & \dots & z_{i,j} & \dots & z_{i,n} \\ \vdots & \vdots & \vdots & \vdots & \vdots \\ z_{m,1} & \dots & z_{m,j} & \dots & z_{m,n} \end{pmatrix} \end{array},$$

with

$$z_{i,j} = \begin{cases} W(t_j, p_i), & \text{if } (t_j, p_i) \in F, \\ -W(p_i, t_j), & \text{if } (p_i, t_j) \in F, \\ W(t_j, p_i) - W(p_i, t_j), & \text{if } (t_j, p_i) \wedge (p_i, t_j) \in F, \\ 0, & \text{otherwise.} \end{cases}$$

The columns of the incidence matrix correspond to the places and the rows to the transitions of the PN. An entry $z_{i,j}$ of the incidence matrix denotes the change of tokens on the place p_i after the firing of transition t_j. A negative value indicates that tokens are removed on the respective place, and tokens are generated on the place by a positive entry.

The total change of token distribution on the places is given by

$$\Delta m = C \cdot x, \tag{2.1}$$

with a *Parikh* vector $x = (x_1, ..., x_j, ..., x_n)$ and Δm as a vector, which contains for each position i the change of tokens held by the place p_i. The entries of the Parikh vector x_j gives the number of times a transition $t_j \in T$ fires. The set of non-zero entries of x is called the *support* of the vector x and is defined by $supp(x) = \{i : x_i \neq 0\}$.

With the help of Equation 2.1, insights of the dynamic behavior of a PN can be obtained based on the topological structure and independent of the initial marking. These structural analyses evaluate the so-called *invariants* of the PN introduced by Lautenbach [130]. There are two types of invariants, T-invariants and place invariants (P-invariants).

2.2.1 Transition invariants

T-invariant provide information about the system's behavior [43,44,125,126]. A T-invariant represents a multiset of transitions with the property that the firing of the transitions does not change the marking of the PN ($\Delta M = 0$) and reproduces an arbitrary state of the system. The integer solutions of the equation system

$$C \cdot x = 0, \tag{2.2}$$

with the Parikh vector x and $x_j \geq 0$, $j = 1, ..., n$ are T-invariants of a PN with the transitions $t_1, ..., t_j, ..., t_n$ and the places $p_1, ..., p_i, ..., p_m$. The set of all T-invariants is

$$TI = \{x | x_j \geq 0 \wedge |supp(x)| > 0\},$$

with all vectors x as solution of Equation 2.2 and $|supp(x)|$ as the number of entries with $x_j \neq 0$. The solution space of Equation 2.2 is infinite, because each scalar multiplication of the vector x with an integer value is a solution. To restrict the set of T-invariants to a unique set of T-invariants, *minimal* T-invariants are defined. A T-invariant $x \in TI$ is *minimal* if $\nexists y \in TI$: $supp(y) \subseteq supp(x)$, i.e., its support does not contain the support of any other T-invariant, and the greatest common divisor of all entries in x is one. The set of minimal T-invariants is denoted by TI_{min}.

For simplification purposes, a minimal T-invariant $ti \in TI_{min}$ is often written as a multiset of transitions $ti = \{x_1 \cdot t_1, ..., x_j \cdot t_j, ..., x_n \cdot t_n\}$, where x is the Parikh vector. If each transition is part of at least one minimal T-invariant, the PN is *covered by T-invariants* (CTI). In this work, we indicate a T-invariant as a multiset of transitions, and we use the term T-invariant to refer to a minimal T-invariant.

The transitions participating in a T-invariant induce a subnet. This *T-invariant-induced subnet* contains the transitions of the T-invariant, the connected places to these transitions, and the arcs in between. For a $PN = (P, T, F, W, M_0)$ with the set of T-invariants TI, the T-invariant-induced subnet for $ti \in TI$ is given by

$$PN_{ti} = (P', T', F', W, M_0), \text{ where} \tag{2.3}$$

$P' = \{p \in P | (p, t) \vee (t, p) \in F, \text{ where } t \in T'\},$
$T' = \{t \in ti\},$
$F' = (P' \times T') \cup (T' \times P') \cap F.$

T-invariants can be categorized into different types, *trivial* T-invariants and *non-trivial* T-invariants. Trivial T-invariants contain two transitions and non-trivial T-invariants more than two transitions. T-invariants can

be further classified in *input-output* T-invariants, *input* T-invariants, *output* T-invariants, and *cyclic* T-invariants. Input-output T-invariants contain at least one input transition, at least one output transition, and inner transitions. Input T-invariants and output T-invariants are composed of inner transitions and at least one input transition or output transition, respectively. Cyclic T-invariants contain only inner transitions.

An algorithm to determine invariants has been described by Koch and Ackermann [131]. The computation of T-invariants, in the worst case, requires exponentially growing space [132, 133].

2.2.2 Place invariants

A P-invariant represents a set of places that do not change their weighted number of tokens during any sequence of steps [43,44,125,126]. P-invariants are the non-zero, integer solutions of the equation system

$$C^T \cdot x = 0, \tag{2.4}$$

with the Parikh vector x, $x_i \geq 0$, $i = 1, ..., m$, and C^T denotes the transposition of the incidence matrix C of a PN with the transitions $t_1, ..., t_j, ..., t_n$ and the places $p_1, ..., p_i, ..., p_m$. The weighted number of tokens is defined by

$$c = x_1 \cdot M(p_1) + ... + x_i \cdot M(p_i) + ... + x_m \cdot M(p_m),$$

with m as an arbitrary marking of PN, and x as a solution of Equation 2.4. For a given marking, the value of c is constant for any reachable marking. The set of all P-invariants is

$$PI = \{x | x_i \geq 0 \wedge |supp(x)| > 0\},$$

with all vectors x as solutions of Equation 2.4 and $|supp(x)|$ as the number of entries where $x_i \neq 0$. A P-invariant $x \in PI$ is *minimal* if $\nexists y \in PI$: $supp(y) \subseteq supp(x)$, i.e., its support does not contain the support of any other P-invariant, and the greatest common divisor of all entries in x is one. The set of minimal P-invariants is PI_{min}.

For simplification purposes, minimal P-invariants are often written as a multiset of places $PI_{min} = \{x_1 \cdot p_1, ..., x_i \cdot p_i, ..., x_m \cdot p_m\}$, where x is a minimal P-invariant. If each place p_i is part of at least one minimal P-invariant the PN is *covered by P-invariants* (CPI). Analogously to a T-invariant, we indicate a P-invariant as a multiset of places, and we use the term P-invariant to refer to a minimal P-invariant.

2.3 Petri nets in systems biology

In the 1990s, for the first time, a PN has been applied to biochemical reaction systems [47]. In the following, we briefly present the application of PN in computational systems biology. For a more comprehensive description, we refer to the book by Koch *et al.* [43] and the review of Chaouiya *et al.* [134].

The places of the PN are the passive part. The meaning of a place depends on the level of abstraction and the biological context. Places represent reservoirs and store units of *pathway components*, like proteins, protein complexes, enzymes, cofactors, bacteria, or cells. Besides, a place can capture the availability of a pathway component. In particular, in PN of signaling pathways, places are used to model the presence of a signal, meaning the presence of molecules required for the reaction. Furthermore, a place can represent a potentially reachable local state, e.g., a gene in its activated and deactivated state, or the state of the cell. In biological pathways, some components, like cofactors, appear in many reactions. To simplify the graphical layout of the PN, we applied so-called *logical places*, which are identical graphical copies of a pathway component and thus carry the same number of tokens on each copy.

The transitions of a PN are the active part and correspond to potential reactions or changes of the state, e.g., binding processes, dissociations, syntheses, degradations, post-translational modifications, activations, or deactivations. The firing of a transition can be interpreted as the occurrence of a reaction.

The arcs of a PN indicate the causal relations between the pathway components and the reactions. Arc weights correspond to the stoichiometric coefficients of the reactions.

Analogously to places, tokens can have different meanings. A token can represent a discrete unit of a pathway component, e.g., one mole, one molecule, one bacterium, or one cell. In PN of signaling pathways, a token describes a signal, meaning the presence of a pathway component is above a threshold that the reaction may occur. In this context, the token flow represents a *signal flow* or *information flow* [108]. In contrast, in metabolic systems there is a *mass flow* or *substance flow* [108]. A PN of a trivial biochemical reaction is illustrated in Figure 2.2, describing the binding of two proteins, A and B, to form a complex, AB.

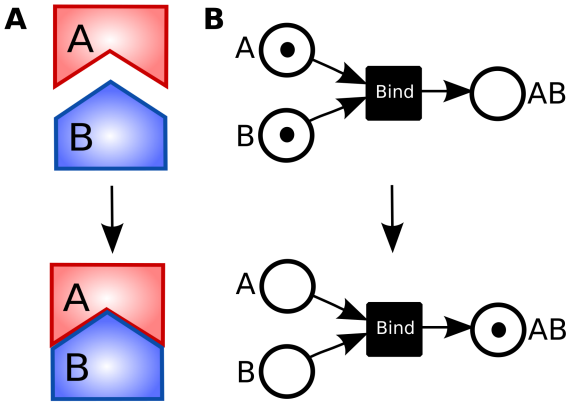

Figure 2.2 PN model of a binding reaction. (A) Schematic representation of a binding reaction. Protein A (red) and protein B (blue) form a complex, AB. (B) The PN with $P = \{A, B, AB\}$, $T = \{Bind\}$, $F = \{(A, Bind), (B, Bind), (Bind, AB)\}$, and $W = \{1, 1, 1\}$ models the binding reaction depicted in A. The three places, A, B, and AB, represent reservoirs of the protein A, protein B, and the protein complex AB, respectively. The transition *Bind* describes a potential binding process. The PN is in the initial marking $M_0 = \{1, 1, 0\}$ (upper part). After the firing of transition *Bind*, the resulting marking of the PN is $M_1 = \{0, 0, 1\}$ (lower part).

Normally, a PN represents only a part of the biological system, like a pathway, or a small process and not the whole cell as a system. There are two ways to model the interface to the environment. In the *open system*, input and output transitions are introduced, for sources and sinks, respectively. In the *closed system*, the PN has no input and output transitions and places forming the boundaries to the system's environment.

For the analysis and verification of biochemical PN models, the invariants are of particular importance. The incidence matrix is equivalent to the *stoichiometry matrix* in biochemistry.

2.3.1 Transition invariants

T-invariant-induced subnets describe functional modules, which can fire at steady state and thereby reflect the basic dynamics of the biological system. The concept of T-invariant is similar to that of EFM [45,86,87] and extreme pathways [88] in traditional biochemical modeling [52,89–91].

In biochemical PN models that are modeled as open systems, each T-invariant should represent a biologically meaningful module of the system. A trivial T-invariant that contains only inner transitions often represents a forward and backward reaction. A trivial T-invariant composed of an input and output transition commonly represents the synthesis and the degradation of a pathway component. Input-output T-invariants frequently describe the ways of signal flows through the biological pathway. Signal flows going from, e.g., a receptor initiation to a regulatory loop are represented by input T-invariants and signal flows starting from, e.g., a regulatory loop and going to the cell response are represented by output T-invariants. Cyclic T-invariants describe cyclic processes, like regulatory loops or amplifications. Biochemical PN models should fulfill the CTI property. Otherwise, transitions that are not part of any T-invariant do not participate in the system's behavior.

The application of T-invariant analysis to signaling pathways has been questioned because T-invariants describe functional modules at steady state and signaling pathways often do not behave like steady-state processes. In signaling pathways, the signal acts like a short and transient process. Nevertheless, invariants have been reported to be suitable for the analysis of signaling pathways [54–58]. Behre and Schuster assumed that after a transient signal, all components of the pathway have to be regenerated before the next signal occurs, and thus the steady state can be assumed averaged over a long time period [135].

Figure 2.3 shows an example of a biochemical PN and its corresponding T-invariants. The PN contains two T-invariants, the input-output T-invariant ti_1 and the trivial T-invariant ti_2. ti_1 represents the synthesis of substance A (transition *Syn*), the activation of substance A (transition *Act*), and the degradation of the activated substance (transition *Deg*). ti_2

describes the activation of substance A (transition *Act*) and its inhibition (transition *Inh*).

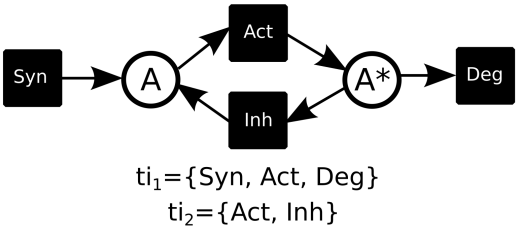

Figure 2.3 A PN of a biological process and its T-invariants. The PN represents the activation of substance A. The unactivated substance (place *A*) can be synthesized by transition *Syn*. Substance A can be activated by transition *Act* and inhibited by transition *Inh*. The activated substance (place *A**) can be degraded by transition *Deg*. The PN contains two T-invariant, ti_1 and ti_2.

2.3.2 Place invariants

A P-invariant expresses a substance balance at steady state and represents the conservation of a pathway component. Analogously to T-invariants, each P-invariant should have a biological interpretation. In case of a PN modeled as an open system, P-invariants are often sparse. A more strict verification criterium is to transform the PN in a closed system, e.g., by the deletion of all input and output transitions and checking the biological interpretation of the P-invariants of the transformed PN. PN that are modeled as a closed system have more P-invariants and ideally, should be CPI.

A small example of a P-invariant is indicated by the PN in Figure 2.4. This PN models an enzyme that is neither synthesized nor degraded. The enzyme contributes to the enzyme-catalyzed reaction of the Michaelis-Menten kinetics [136]. The PN contains one P-invariant, $pi_1 = \{E, ES\}$. The weighted sum of marking of the places E and ES, $c = M(E) + M(ES)$, is always constant in every reachable marking of the PN. The P-invariant pi_1 represents the conservation of the enzyme E. The amount of enzyme present in the system stays always the same, independent of the system's state, because the enzyme is neither produced nor consumed in the network. In contrast, the substrate S is synthesized and the product P is degradated, and therefore do not participate in a P-invariant.

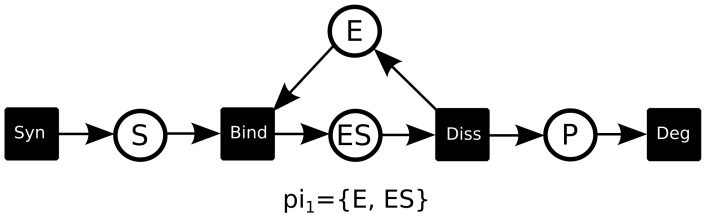

Figure 2.4 A PN of an enzyme-catalyzed reaction inspired by the Michaelis-Menten kinetics and its P-invariant The PN contains one P-invariant, pi_1, which includes the places E and ES. Meaning, the weighted sum of tokens on these places is not changed during the simulation.

2.4 Stochastic Petri net

We describe the dynamic behavior of PN in Section *Petri net formalism*. The simulation of a PN has been defined as a sequence of steps. In a standard PN model, a step need no time, as, e.g., a biochemical reaction would take. To model the progression of a system over time, the standard PN has to be extended. Here, a stochastic Petri net (SPN) provides a method to simulate a biochemical system in a stochastic manner over time [127]. In an SPN, each transition is associated with a stochastic rate constant, and including its pre- and post-places, describes a random process. A place in an SPN is equivalent to a random variable, and the tokens hold by a place correspond to the values a random variable can attain. The simulation of an SPN is usually performed by the application of Gillespie's exact stochastic simulation algorithm (SSA) [137, 138].

2.4.1 Gillespie's stochastic simulation algorithm

Gillespie's exact SSA is a numerical simulation algorithm of the chemical master equation [137, 138]. Each simulation run is an individual trajectory in the phase space described by the chemical master equation. The algorithm simulates each reaction or firing of a transition individually and moves forward in time from one firing of a transition to the next. In the following, we give a short introduction to the algorithm. For a more comprehensive explanation, we refer to Gillespie [137,138] and the books by Wilkinson [127] and Ingalls [128].

The input of the exact SSA is the initial marking M_0 and the stochastic

rate constants c_i, which are related to the deterministic rate constants k_i. The exact SSA consists of the following steps:

1. **Initialization step** The time t is initialized to zero.

2. **Determining reaction propensities** For a PN with $|T|$ transitions, each transition or reaction is associated to a reaction propensity a_i, $i = 1, 2, ..., |T|$. The reaction propensities are calculated from the marking and the stochastic rate constants, according to the order of the reaction. The propensity of a reaction is the probability of a reaction occurrence per time unit, e.g., second (sec), minute (min), or hour (h).

3. **Generating two random numbers** Two uniformly distributed random numbers r_1 and r_2 in the interval $[0, 1]$ are computed.

4. **Determining the next time point** The waiting time τ for the firing is computed from the exponential distribution function $p(0 \leq \tau \leq t) = a_0 e^{-a_0 \tau}$, where $a_0 = \sum_{i=1}^{r} a_i$ is the sum of the reaction propensities. The waiting time τ is determined by using the random number, r_1,

$$\tau = \frac{1}{a_0} ln(\frac{1}{r_1}).$$

5. **Determining the next transition** The probability that the transition T_i will occur is proportional to the reaction propensity, a_i, and is given by

$$P(T_i) = \frac{a_i}{a_0}.$$

   The next occurring transition is chosen using the second random number, r_2.

6. **Updating step** After a transition has fired the time is increased by τ and the reaction propensities are recalculated because the marking M has changed.

7. **Iteration** The process is repeated until the time reaches a predefined value, the *simulation time*.

Chapter 3

Material and Methods

This chapter is divided into three parts and summarizes the material and the methodical procedures used in this thesis. The first part describes general procedure of the development of a PN model. In the next part, the experimental data are depicted on which the mathematical models in this thesis are based. The software applied for this work is listed in the last part.

3.1 Development of Petri net models

The development of PN models to describe a biological system can be divided into the following steps, whereby it is often necessary to make iterations between the steps.

3.1.1 Data collection

Initially, molecular interactions and functional mechanisms known about the biological process have to be manually collected. The main source for these information is the existing literature. The number of relevant publications can get quite large, especially for well-known pathways. A lot of databases exist summarizing literature data. Important databases for signaling pathways are the Kyoto Encyclopedia of Genes and Genomes (KEGG) [139], BioModels [140], and the Reactome Knowledgebase [141]. An overview about protein-protein interaction and pathway databases can be found at `http://www.pathguide.org/`. However, recently discovered processes often

have not yet been integrated. Here, literature is the only source to model these poorly understood pathways. The selected information of the biological process of interest is often inconsistent and incomplete. One of the key challenges is to organize and evaluate the selected information and their integration into one consensus, mathematically consistent model. Particular attention should be given to the model organism used for the experiments. In different model organism or even cell types, the pathway may be quite different.

For the extension of the PN into a quantitative model, additional quantitative experimental data have to be gathered. Appropriate data are concentrations or numbers of pathway components at different time-points. Sources for quantitative experimental data are published data, own experiments, or databases that include kinetic information, such as BRaunschweig ENzyme DAtabase (BRENDA) [142].

3.1.2 Model construction

Usually, the construction of the model starts with a small PN based on a few references or a few reactions of the biological system. Afterwards the topology of the PN is analyzed to find structures that contradict the biological knowledge, see Subsection *Model analysis*. To resolve the identified inconsistencies, the selected data should be repeatedly studied and the wrongly extended structures of the PN should be modified. Providing that no inconsistencies were found, the PN can be, step by step, extended by further reactions that are essential for the biological process. After each model extension, the PN should be analyzed and verified.

For quantitative modeling, the kinetic parameters have to be integrated. Based on time-resolved data, the kinetic parameters of the model can be determined or estimated. The parameters of an SPN can be estimated by manual parameter fitting or by parameter estimation methods [143].

3.1.3 Model analysis

The PN formalism provides multiple techniques to check the PN model for consistency and correctness [43]. The verification of the PN includes

the T-invariant and P-invariant analysis. Another verification criterion is to simulate the PN and to check the biologically meaningful token flow. The methods presented in this work, the Manatee invariant analysis and the *in silico* knockout analysis, provide further verification techniques. The comparison of *in silico* knockouts with experimental knockout or knockdown studies allow to detect inconsistencies. A method to perform a *in silico* knockout analysis is introduced in this thesis. The biologically meaningful token flow can be checked by the simulation of the PN.

For the verification of an SPN, the simulation of the model should be able to reproduce the known, quantiative experimental data. To check this reproducibility, the model should be simulated and the token numbers, which represent concentrations or molecule numbers over time, have to be compared with the time-resolved quantitative data. If the model can not reproduce the experiments, the kinetic parameters have to be refined or the PN topology could be wrong.

Finally, when the mathematical model is capable to reproduce the experimental data, the model can be applied for the prediction of system‘s behavior. Now, the actual iterative model development starts [39] by the generation of predictions, which can be tested in future experiments called model validation. For example, the simulated effects of *in silico* knockouts provide valuable predictions for model validation.

3.2 Experimental data

For the two PN models presented in this thesis, multiple experimental data were collected. Depending on the level of abstraction of the model, the data range from functional information to quantitative, time-resolved data.

3.2.1 The Petri net of the xenophagic capturing of *Salmonella* in epithelial cells

The PN is based on molecular interactions and functional mechanisms compiled from the literature. A list of the references is given in Table A2 in the

appendix. All known processes of the xenophagic capturing of *Salmonella* that has been biochemically proven in epithelial cells (primarily strain HeLa) are included in the network. HeLa cells derived from a human cervical cancer are the commonly used epithelial cell line to study host-*Salmonella* interactions *in vitro*. In public databases, such as KEGG [139], BioModels [140], the Reactome Knowledgebase [141], and BRENDA [142] information of the xenophagic recognition of *Salmonella* is not available at present time.

3.2.2 The stochastic Petri net of a *Salmonella*-infected epithelial cell

The SPN was parameterized by literature data from different sources, see Table 4.5. The model is mainly based on semi-quantitative single-cell studies from Malik-Kale *et al.*, Knodler *et al.*, and Misselwitz *et al.* [16, 17, 77, 79]. In these studies, HeLa cells as a cell model for epithelial cells have been infected with *Salmonella* and analyzed by fluorescence microscopy or live cell imaging. For an overview of the techniques for monitoring the intracellular *Salmonella* population, we refer to the reviews of Knodler *et al.* and Castanheira *et al.* [144, 145].

3.3 Software

For the construction, simulation, and analysis of the PN, we used the open-source tool MonaLisa [84]. MonaLisa is a freely available software and provides a user-friendly graphical user interface (GUI) to easily build and appropriately visualize PN models. The tool supports qualitative and quantitative modeling. For the stochastic simulation of the SPN, we applied Gillespie's exact SSA [146]. The simulation results are further processed and visualized using R [147]. For the analysis of Manatee invariants and *in silico* knock-outs, we applied the software isiKnock developed in the scope of this work. isiKnock is available on sourceforge `https://sourceforge.net/projects/molbi-isiknock/`.

Chapter 4

Results and Discussion

This chapter is divided into three sections. The first two sections describe the two mathematical models of this work, the PN model of the xenophagic capturing of *Salmonella* Typhimurium, in the following referred to as *Salmonella*, in epithelial cells and the stochastic PN model of an infected epithelial cell with *Salmonella*. The last section deals with the method development of this thesis. Here, the novel method of *in silico* knockouts and the concept of Manatee invariants are presented. Furthermore, we introduce a tool named isiKnock, which allows the automatized prediction of *in silico* knockout behavior.

Partial results of this thesis have already been published and parts of the following descriptions are based on these publications. The PN of the xenophagic capturing of *Salmonella* and the concept of *in silico* knockouts have been published in PLoS Computational Biology [57]. The concept of Manatee invariants developed in cooperation with Leonie Amstein and Jörg Ackermann has been published in BMC Systems Biology [148].

4.1 The Petri net of the xenophagic capturing of *Salmonella* in epithelial cells

In this section, we present a mathematical model of the xenophagic capturing of *Salmonella* in epithelial cells described in the PN formalism. At first, the current view of the selective recognition of *Salmonella* to the xenophagy

pathway is reviewed and discussed, which serves as the basis for the development of the PN model. The various information of molecular interactions and functional mechanisms published in the last years are combined into one consensus model. This PN model is presented and analyzed in the next part, including the analysis of T-invariants, P-invariants, and the novel concept of Manatee invariants, which is described in Subsection *The concept of Manatee invariants*. Furthermore, we applied the proposed method of *in silico* knockouts (see Subsection *The concept of in silico knockouts*) to examine the knockout behavior of the xenophagic capturing of *Salmonella* and to compare the results with experimental perturbation data for model verification.

4.1.1 The xenophagic capturing of *Salmonella*

In the last years, various information of molecular interactions and functional mechanisms about the recognition and guidance of *Salmonella* to xenophagy has been elucidated and published in diverse publications. We combined the information of the state of the art in this research field into a schematic representation of the process, see Figure 4.1.

The following description of the pathway is based on the references used to build the PN of the xenophagic capturing of *Salmonella* in epithelial cells by Scheidel *et al.* [57]. It has to be noted that the research area of xenophagy is in focus of ongoing research. After our publication has been published in December 2016 [57], novel important findings have been elucidated. These aspects can be included to the PN in future work and are summarized in Subsection *Possible extensions of the Petri net model*.

Salmonella can infiltrate epithelial cells by a mechanism that is characterized by membrane ruffling [8], see Figure 4.1 upper part. The invaded bacterium is enclosed by the SCV [9]. Inside the cell, the bacteria stay in the SCV or can disrupt their vacuoles and get access to the cytosol [13, 34]. At first, the escaping bacterium is inside a damaged SCV, which is partially exposed to the cytosol. Later, the bacterium can lose the membrane remains of the SCV and is free within the cytosol. It is assumed that both *Salmonella* inside a damaged SCV and the cytosol are captured by the xenophagy path-

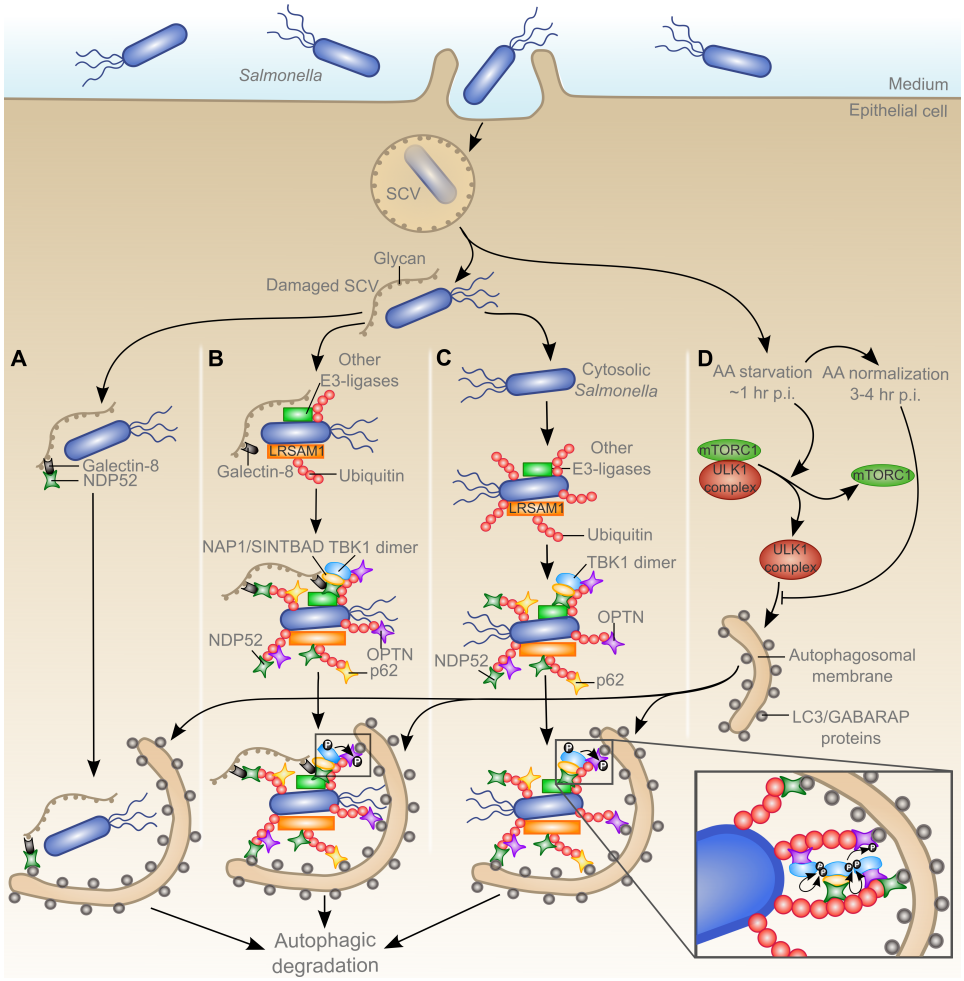

Figure 4.1 Schematic representation of the xenophagic capturing of *Salmonella* in epithelial cells. Inside epithelial cells, *Salmonella* are localized in the SCV. A small fraction of these bacteria disrupts the SCV. Bacteria with cytosolic access can be inside a damaged SCV or free in the cytosol. (A) Galectin-8-dependent xenophagic recognition. Galectin-8 binds to host glycan on the damaged SCV and recruits NDP52, which in turn binds LC3/GABARAP proteins on the autophagosomal membrane. (B) Galectin-8-dependent and ubiquitin-dependent xenophagic recognition. Besides galectin-8 recruitment, partially cytosolic bacteria get ubiquitinated by LRSAM1 and other E3 ubiquitin ligases. The autophagy receptors p62, NDP52, and OPTN bind to the ubiquitin chains and link the bacterium to LC3/GABARAP proteins on the autophagic membrane. OPTN phosphorylation by TBK1 enhances the binding affinity of OPTN with LC3 proteins. The hypothetical mechanism of TBK1 activation is depicted in the detailed view. (C) Ubiquitin-dependent xenophagic recognition of *Salmonella* inside the cytosol, i.e., without SCV membrane remains. (D) Nutrient-dependent regulation of xenophagy. Intracellular AA starvation is induced by SCV damage, resulting in the inactivation of mTORC1. Inactivated mTORC1 dissociates from the ULK1 complex, recovers the kinase activity of the ULK1 complex and is required for the autophagosomal membrane formation. The intracellular AA level normalizes, and mTORC1 localizes at the surface of the SCV and gets reactivated.

way for degradation [34].

Galectin-8-dependent xenophagic recognition

Due to the disruption of the vacuolar membrane, host glycans, which are localized to the luminal side of the vacuole, are exposed to the cytosol. The cytosolic lectin, galectin-8, can bind to these glycans and targets *Salmonella* inside the damaged SCV for xenophagy [36], see Figure 4.1A. After recruitment of galectin-8 to the damaged SCV, the autophagy receptor nuclear dot protein 52 (NDP52) binds to galectin-8 [36, 149]. Autophagy receptors are like adaptor proteins that link components recruited to the bacterial surface, like galectin-8 or ubiquitin, with the xenophagic pathway by the binding to proteins of the microtubule-associated protein 1 light chain 3 (LC3)/γ-aminobutyric acid receptor-associated protein (GABARAP) family [29–31, 36]. The LC3/GABARAP protein family consists of seven members, two splicing variants of LC3A, LC3B, LC3C, GABARAP, GABARAPL1, and GABARAPL2, which are human orthologs of the autophagy-related protein 8 (Atg8) in yeast. The interaction of NDP52 with both galectin-8 and LC3/GABARAP proteins on the autophagosomal membrane targets the bacterium to the autophagic machinery.

Ubiquitin-dependent xenophagic recognition

Salmonella with cytosolic access immediately recruit polyubiquitin chains, forming a dense coat around the bacteria [12]. Both *Salmonella* inside a damaged SCV and free cytosolic bacteria accumulate ubiquitin chains, see Figure 4.1B and 4.1C, respectively. It remains unknown, whether bacterial components or host proteins attached to the bacterial surface are ubiquitinated. Another explanation may be the autoubiquitination of E3 ubiquitin ligases. One E3 ubiquitin ligase, the leucine-rich repeat and sterile α motif-containing 1 (LRSAM1), has been reported to participate in the ubiquitination of *Salmonella* [150, 151]. The bacterium is decorated by a ubiquitin coat, containing multiple linkage types, at least K48-, K63-, and linear-conjugated ubiquitin chains [152, 153]. However, LRSAM1 has been shown to form predominantly other chain types, K6- and K27-conjugated

ubiquitin chains [150]. The presence of multiple linkage types suggests the participation of other unknown E3 ubiquitin ligases in the ubiquitination of *Salmonella*, in addition to LRSAM1.

Simultaneously, the autophagy receptors NDP52 [31], p62 [29], and optineurin (OPTN) [30] can bind to LC3/GABARAP proteins on the autophagosomal membrane and to ubiquitin chains on the bacterium. All three autophagy receptors are recruited to *Salmonella* and carry the ubiquitinated bacteria to the autophagic pathway. The missing of one of these three autophagy receptors results in an increased replication of *Salmonella* inside the cell [29–31, 154], and the missing of two of the three autophagy receptor does not additively enhance this effect [30, 154]. Therefore, all three autophagy receptors non-redundantly and independently of each other protect the cell from cytosolic *Salmonella*. This behavior indicates distinct functions of NDP52, p62, and OPTN in restricting *Salmonella* proliferation, besides their role as autophagy receptors.

For instance, the autophagy receptors differ in their preference to bind poly-ubiquitin chains of different linkage types. p62 preferentially binds K63-linked poly-ubiquitin chains, but it can also bind K48-linked poly-ubiquitin chains and mono-ubiquitin [23]. OPTN binds to linear ubiquitin chains and K63-linked poly-ubiquitin chains [30, 155] and in its phosphorylated state to nearly all linkage types [156]. NDP52 binds to mono-ubiquitin, other binding affinities need to be studied in further experiments [154]. Another point of difference is that only NDP52 can interact with galectin-8 [36] and selectively binds to LC3C [157]. In contrast, p62 interacts with all proteins of the LC3/GABARAP protein family to the same extent [157]. Moreover, NDP52 binds the serine/threonine-protein kinase TANK-binding kinase 1 (TBK1) and recruits TBK1 in a complex with adaptor proteins, NAK-associated protein 1 (NAP1) or similar to NAP1 TBK1 adaptor (SINTBAD), to ubiquitinated *Salmonella* [31]. The unique feature of OPTN is the increased binding affinity to LC3 proteins and ubiquitin as a result of its phosphorylation by TBK1 [30, 156, 158, 159].

TBK1-dependent enhancement of xenophagic capturing

Activated TBK1 leads to the polyphosphorylation of OPTN at serine-177. Serine-177 is adjacent to the N-terminal LC3-interacting region (LIR) motif of OPTN, which facilitates the binding with LC3 proteins. The phosphorylation of OPTN at serine-177 enhances the binding affinity to LC3B by changing the hydrogen bond formation. This enhanced binding affinity has been shown to restrict the replication of *Salmonella* [30]. TBK1 can be activated by the pattern recognition receptor Toll-like receptor 4 (TLR4). The TLR4 signaling can be triggered in response to lipopolysaccharides (LPS), which are components of the cell wall of Gram-negative bacteria, such as *Salmonella*. The knockdown of TBK1 in the HeLa cell line results in an enhanced *Salmonella* proliferation [30, 31, 160], although TLR4 is not functional in HeLa cells due to the missing of the accessory protein, MD2. This suggests that there are unknown mechanisms, resulting in the activation of TBK1.

To explain TBK1 activation upon *Salmonella* infection in HeLa cells, we assumed a mechanism of TBK1 activation by autophosphorylation, see detailed view in Figure 4.1. The inactive form of TBK1 is a dimer, which can form higher order oligomer structures [161–164]. In the inactive state, without oligomerization, autophosphorylation is prevented, because the two kinase domains are located on the opposite sides of the dimer [163]. In consequence of the oligomerization, TBK1 is activated by autophosphorylation. The NAP1/SINTBAD-NDP52 complex and OPTN recruit TBK1 to ubiquitinated *Salmonella* [30, 31]. We hypothesized that the recruitment of TBK1 by NDP52 and OPTN results in a local enrichment of TBK1 dimers. This high local concentration of TBK1 dimers may allow for oligomerization, which in turn results in the autophosphorylation of TBK1. The controlled activation of TBK1 by localization has previously been suggested in a review by Helgason *et al.* [165]. Actually, NDP52 and OPTN are located in the same local domain around *Salmonella*, separately from p62 [30, 154]. An interesting point for future research is to test whether TBK1 is localized in the same domain as NDP52 and OPTN. Additionally, NAP1 has been demonstrated to promote the oligomerization of TBK1 in human embryonic

kidney 293T cells [166].

A recent study by Richter *et al.* describes a similar mechanism of TBK1 activation and its role in the selective autophagy of damaged mitochondria [156]. They reported that phosphorylation of the ubiquitin binding in ABIN and NEMO (UBAN) domain of OPTN by TBK1 promotes the binding of OPTN to ubiquitin. In turn, the optimal activation of TBK1 requires the interaction of OPTN with K63-linked polyubiquitin or linear-polyubiquitin [155]. Moreover, K63-linked ubiquitination of TBK1 itself has been shown to be essential for its kinase activity [161]. The higher binding affinity of OPTN to ubiquitin chains in a complex with TBK1 may amplify the high local concentration and autoactivation of TBK1. Further studies have to clarify whether TBK1 activation by autophosphorylation is orchestrated by a high concentration of TBK1 in local domains around the bacterium to facilitate xenophagy of *Salmonella*. Besides OPTN, TBK1 also phosphorylates the other autophagy receptors, p62 and NDP52 [156, 167, 168], which may promote *Salmonella* xenophagy.

The activation of TBK1 to facilitate xenophagy can be of pharmaceutical interest. Intestinal epithelial cells (IEC), which are *in vivo* invaded by *Salmonella*, do only sparsely express TLR4 [169] and are LPS-hyporesponsive, due to the high concentration of LPS in the gut lumen [170]. Here, the autoactivation of TBK1 by high local concentration may be a mechanism to promote *Salmonella* xenophagy and to protect the host cell from cytosolic bacteria.

Nutrient-dependent regulation of xenophagy The xenophagy of *Salmonella* is assumed to be regulated by the intracellular nutrient level. Amino acid (AA) starvation is caused by escaping bacteria from the SCV and thus, results in an induction of xenophagy [171, 172], see Figure 4.1D. The AA starvation at approximately ∼1 h post infection (p.i.) is a host-driven process, which is provoked by the disruption of the vacuolar membrane of the SCV and not by metabolizing bacteria inside the cytosol. Thereupon, the protein kinase mammalian target of rapamycin (mTOR) is inhibited. mTOR is together with the regulatory-associated protein of mTOR (Raptor) and mammalian lethal with SEC13 protein 8 (mLST8) a subunit of

the mTOR complex 1 (mTORC1). Inactivated mTORC1 dissociates from the uncoordinated 51-like kinase 1 (ULK1) complex, which is formed by ULK1, focal adhesion kinase family interacting protein of 200 kD (FIP200), autophagy-related protein 13 (ATG13), and autophagy-related protein 101 (ATG101) [173]. Afterwards, the ULK1 complex recovers its kinase activity, which is suggested to be required for the formation of the autophagosomal membrane. At 3-4 h p.i., the intracellular AA level normalizes, and mTORC1 accumulates around the SCV and gets reactivated.

Probably, the reactivation of mTORC1 may be the reason for the escape of *Salmonella* from xenophagy in later time points of the infection and for the inefficiency of *Salmonella* xenophagy [11,14–17]. To elucidate the mechanisms, leading to AA starvation and particularly how bacteria trigger AA normalization are important topics for therapeutic research.

4.1.2 Petri net annotation and topology

We constructed a PN model to mathematically describe the processes of the xenophagic capturing of *Salmonella* in epithelial cells, graphically summarized in Figure 4.1. For each pathway component a place and for each reaction a transition was assigned. A complete list of the literature references is given by Table A2 in the appendix. To provide a PN without P-invariants for the knockout analysis, the PN presented in this work slightly differs from the PN model published by Scheidel *et al.* [57], see Subsection *In silico knockout of Petri net models with P-invariants* for more information about the effects of P-invariant on the *in silico* knockouts.

The PN consists of 63 places and 75 transitions connected by 195 arcs. A graphical representation of the PN is depicted in Figure 4.2. The places and transitions of the PN and their biological interpretation are listed in Table A1 and Table A2 in the appendix, respectively.

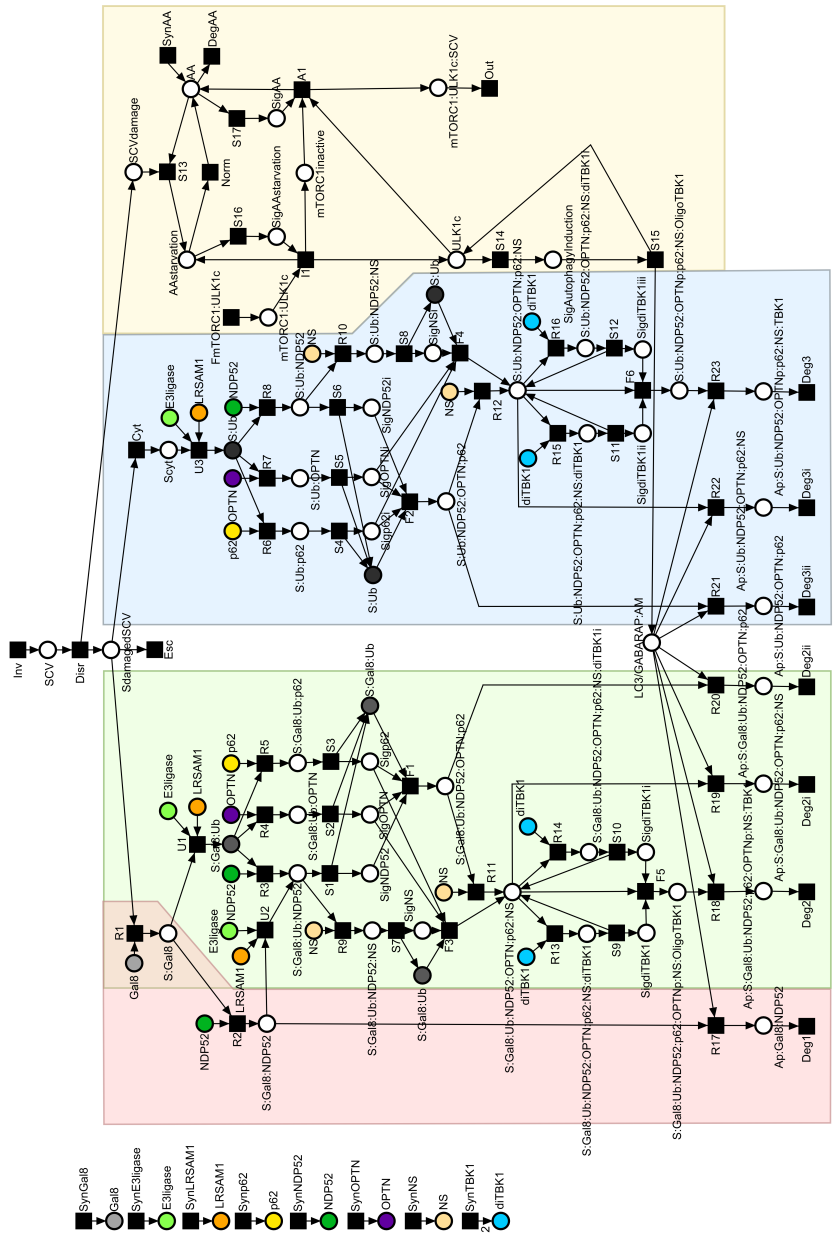

Figure 4.2 The PN of the xenophagic capturing of *Salmonella* in epithelial cells. The model represents the galectin-8-dependent xenophagic recognition (red part, see Figure 4.1A), the ubiquitin- and galectin-8-dependent xenophagic recognition (green part, see Figure 4.1B), the ubiquitin-dependent xenophagic recognition (blue part, see Figure 4.1C), and the nutrient-dependent regulation (yellow part, see Figure 4.1D). All places and transitions are listed in Table A1 and Table A2 in the appendix. Logical places are represented by different colors.

The PN is modeled as an open system and comprises ten input and seven output transitions. An input transition that is named "*SynX*" represents the synthesis of a pathway component X. The input transition *FmTORC1:ULK1c* describes the syntheses of the compounds of the mTORC1 and the ULK1 complex and their formation to a complex, the mTORC1-ULK1 complex. The input transition *Inv* depicts the invasion of *Salmonella* into the epithelial cell. Output transitions that are marked by the letters "*Deg*" refer to degradations of captured *Salmonella* inside the autophagosome, and the output transition *Out* represents the removal of the complex between mTORC1 and the ULK1 complex from the SCV. Modifier components, such as ubiquitin and phosphate, are not explicitly modeled as a place in the PN. Ubiquitination is indirectly modeled by transitions starting with the initial letter "*U*", and phosphorylation is performed by the transitions *F5* and *F6*. Recruitments of pathway components are modeled by transitions labeled with the initial letter "*R*" and complex formations by the initial letter "*F*"'. Transitions that are marked by the letter "*S*" represent the forwarding of a signal. Transitions with the initial letter "*I*" and "*A*" refer to inactivation and activation processes, respectively.

Places that are named, e.g., "*Y:X*" describe complexes of the pathway components Y and X. Places whose names start with "*Sig*" are introduced for technical reasons and represent signals, indicating that a certain pathway component has bound to the complex. Each of the seven places starting with the letters "*Ap*" represents the bacterium, which is trapped by the LC3/GABARAP-positive autophagosomal membrane.

The places of the PN and the tokens carried by these places have different interpretations, see Table 4.1. Places, like *Scyt* or *S:Gal8*, are similar to reservoirs that store units of pathway components, e.g., *Salmonella* inside the cytosol or galectin-8-positive *Salmonella*, respectively. A token held by these places represents one bacterium at different locations in the cell or one bacterium labeled by various proteins. Places, such as *Gal8*, *NDP52*, or *p62*, model the presence of a signal, meaning that the threshold level of molecules required for the reaction is reached. A token on these places represents the availability of sufficient molecules for the occurrence of the reaction. Places, such as *SCVdamage* or *AA* describe states, e.g., the signal

that the SCV is damaged or the signal representing a normal AA level in the cell, respectively.

Table 4.1 Places of the PN of the xenophagic capturing of *Salmonella* in epithelial cells and their interpretation.

Interpretation	Places
Store units of pathway components	SCV, SdamagedSCV, S:Gal8:NDP52, Scyt, S:Gal8, S:Gal8:Ub, S:Gal8:Ub:p62, S:Gal8:Ub:OPTN, S:Gal8:Ub:NDP52, S:Gal8:Ub:NDP52:NS, S:Gal8:Ub:NDP52:OPTN:p62, S:Gal8:Ub:NDP52:OPTN:p62:NS, S:Gal8:Ub:NDP52:OPTN:p62:NS:diTBK1, S:Gal8:Ub:NDP52:OPTN:p62:NS:diTBK1i, S:Gal8:Ub:NDP52:OPTNp:p62:NS:OligoTBK1, S:Ub, S:Ub:p62, S:Ub:OPTN, S:Ub:NDP52, S:Ub:NDP52:NS, S:Ub:NDP52:OPTN:p62, S:Ub:NDP52:OPTN:p62:NS, S:Ub:NDP52:OPTN:p62:NS:diTBK1, S:Ub:NDP52:OPTN:p62:NS:diTBK1i, S:Ub:NDP52:OPTNp:p62:NS:OligoTBK1, Ap:S:Gal8:NDP52, Ap:S:Gal8:Ub:NDP52:OPTN:p62, Ap:S:Gal8:Ub:NDP52:OPTN:p62:NS, Ap:S:Gal8:Ub:NDP52:OPTNp:p62:NS:TBK1, Ap:S:Ub:NDP52:OPTN:p62, Ap:S:Ub:NDP52:OPTN:p62:NS, Ap:S:Ub:NDP52:OPTNp:p62:NS:TBK1
Capture the visibility of a component	Gal8, NDP52, OPTN, p62, LRSAM1, E3ligase, diTBK1, NS, LC3/GABARAP:AM, mTORC1:ULK1c, mTORC1:ULK1c:SCV, mTORC1inactive, ULK1c
Represent a state	SCVdamage, SigAA, AA, AAstarvation, SigAutophagyInduction, SigAAstarvation, SigNDP52, SigNDP52i, SigOPTN, SigOPTNi, Sigp62, Sigp62i, SigNS, SigNSi, SigdiTBK1, SigdiTBK1i, SigdiTBK1ii, SigdiTBK1iii

In the following, we describe some sub-structures of the PN model in a more detailed way that differ from ordinary biochemical reactions, such as binding processes, dissociations, or phosphorylations.

ULK1 complex-dependent induction of autophagy

It is suggested that the kinase activity of the ULK1 complex is required for the formation of the autophagosomal membrane. The formation of the autophagosomal membrane is a complex process, consisting of multiple proteins and complexes and was out of scope to be modeled of this work. To still model the ULK1 complex-dependent induction of autophagy, the process can be described in a more abstract manner, see Figure 4.3.

Here, read arcs offer the opportunity to model the activation of a process by the availability of a component. Figure 4.3A shows the induction of LC3/GABARAP-positive autophagosomal membrane modeled by a read arc. The LC3/GABARAP-positive autophagosomal membrane (place *LC3/GABARAP:AM*) can only be formed if the ULK1 complex (place

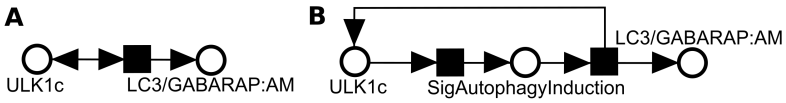

Figure 4.3 PN topology of the ULK1 complex-dependent induction of autophagy (A) The PN structure abstracts the induction of autophagy by ULK1 in form of a read arc. (B) The read arc was dissolved by an additional place, *SigAutophagyInduction*.

ULK1c) is present. However, the use of read arcs hampers the analysis of invariants, as they are not reflected by the incidence matrix. We modeled the ULK1-dependent induction of autophagy by the PN structure depicted in Figure 4.3B. Here, the read arc was dissolved by an additional, technical place, *SigAutophagyInduction*, representing a signal of autophagy induction and a transition, which reproduces the ULK1 complex and forms the LC3/GABARAP-positive autophagosomal membrane. Similar structures are used at various points of the PN model.

Formation of multicomponent complexes

The formation of complexes that consist of multiple components can occur in various ways. The complex of ubiquitinated *Salmonella* with the three autophagy receptors is one example of a small multicomponent complex. All three autophagy receptors, p62, NDP52, and OPTN, can bind almost simultaneously and independently of each other to the ubiquitinated coat of the bacterium [29–31, 154]. Figure 4.4A illustrates a PN model, which models the binding of all possible orders of binding events of the autophagy receptors to the ubiquitin chains around *Salmonella*. For only three proteins, their are six possible binding orders, but by adding further proteins the problem raises with $n!$, where n is the number of proteins. The modeling of all possible orders of binding events leads to huge and interconnected network structures due to the combinatorial complexity. The problem of combinatorial complexity of protein complexes in pathways is well-known, reviewed by Hlavacek *et al.* [174].

To reduce the complexity of the network structure, we modeled the autophagy receptor binding by the PN depicted in Figure 4.4B. The PN models the binding of the three autophagy receptors to ubiquitinated *Salmonella*,

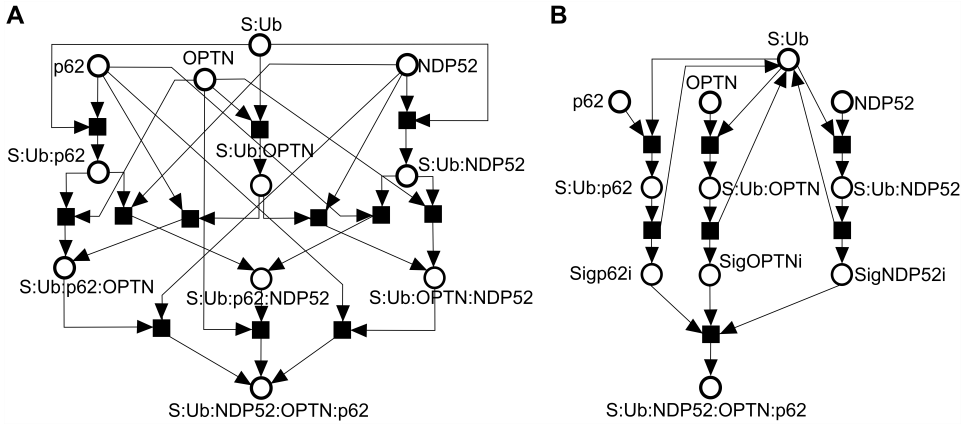

Figure 4.4 PN topology of the autophagy receptor binding to ubiquitinated *Salmonella*. (A) Complex and highly interconnected structure of the PN of the autophagy receptor binding. The PN models all possible orders of binding events of the three autophagy receptors, p62, OPTN, and NDP52. (B) Simplified PN of the autophagy receptor binding.

by three separate transitions, resulting in the formation of the complexes, ubiquitinated *Salmonella* with p62 (place *S:Ub:p62*), with NDP52 (place *S:Ub:NDP52*), and with OPTN (place *S:Ub:OPTN*). When the complexes have formed, a signal can be generated on the places *Sigp62i*, *SigNDP52i*, and *SigOPTNi*, respectively. A token on these places represents the presence of a required amount of the certain autophagy receptor associated with ubiquitinated *Salmonella*. If all places, *Sigp62i*, *SigNDP52i*, and *SigOPTNi*, hold at least one token, all three autophagy receptors have been recruited in a sufficient amount to *Salmonella* and the complex of the three autophagy receptors and ubiquitinated *Salmonella* can form. In comparison to the PN depicted in Figure 4.4A, which models the binding of all possible orders of binding events, the simplified PN in Figure 4.4B does not model a complex that is composed of only two of the three autophagy receptors. However, due to the fact that all three autophagy receptors are required and two autophagy receptors are not sufficient to lead *Salmonella* to xenophagy, it is not necessary to model all intermediate complexes. This PN topology was also applied to model the autophagy receptor binding to galectin-8-positive and ubiquitin-positive *Salmonella*. We used similar structures to model the binding of NAP1/SINTBAD to NDP52.

Autoactivation of TBK1

The mechanism of TBK1 activation is modeled by the PN topology depicted in Figure 4.5. The PN models the binding of TBK1 dimers by two separate transitions, whose firing results in the formation of TBK1-positive *Salmonella*. Then, a signal is generated on the places *SigdiTBK1ii* and *SigdiTBK1iii*. A token on these places represents the presence of a required amount of TBK1 dimers recruited to ubiquitinated *Salmonella*. If the places *SigdiTBK1ii* and *SigdiTBK1iii* hold at least one token, the TBK1 dimers are present in a sufficient amount to form oligomers for their autoactivation in microdomains around ubiquitinated *Salmonella*, and in turn OPTN is phosphorylated. This structure was also applied to model TBK1 activation at the surface of galectin-8-positive and ubiquitin-positive *Salmonella*.

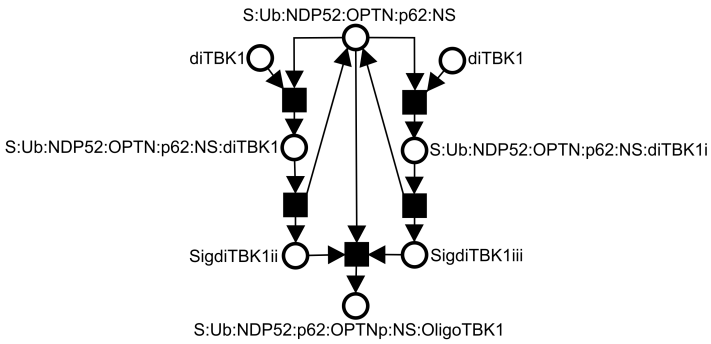

Figure 4.5 PN topology of the TBK1 activation. The PN topology abstracts the oligomerization of TBK1 and phosphorylation of OPTN.

Obviously, it is an oversimplification to model the complex mechanisms, leading to the activation of TBK1, by such a simple network structure depicted in Figure 4.5A. The PN does not include any spatial components, which are essential for the controlled autoactivation of TBK1 by high local concentrations. Nevertheless, the level of detail is sufficient to generate predictions of the dependencies between the components of the pathway.

Possible extensions of the Petri net model

To reduce the complexity of the PN, we had to make some abstractions. We neglected that the bacterium can escape from its damaged vacuole at

later time points of infection. If the bacterium is once in the ubiquitin- and galectin-8-dependent xenophagic recognition pathway, it can not loose its galectin-8-positive vacuole and enters the ubiquitin-dependent xenophagic recognition pathway.

Besides galectin-8 and ubiquitin, the second messenger diacylglycerol (DAG) is recruited to the SCV in an early phase after infection and restricts *Salmonella* replication [175]. It has not yet been finally clarified whether DAG-positive *Salmonella* is linked to the xenophagy pathway or a process called LC3-associated phagocytosis (LAP) [176, 177]. The depletion of the DAG-dependent pathway and the ubiquitin-dependent xenophagic recognition has been demonstrated to result in an additive effect of LC3-recruitment to *Salmonella* [175], indicating independent pathways. Electron microscopic studies would be required to clearly distinguish between LAP and xenophagy.

In addition to the three autophagy receptors, p62, NPD52, and OPTN, a fourth receptor, Tax1-binding protein 1 (TAX1BP1), seems to play an important role in the xenophagic capturing of *Salmonella* [178]. The inhibition of TAX1BP1 together with NDP52 results in an additive effect on the restriction of *Salmonella* proliferation, and TAX1BP1 may even partially compensate the knockdown of NDP52. TAX1BP1 is not included in the PN, since it is unclear whether TAX1BP1 alone is sufficient for autophagic degradation of *Salmonella* or the combination with the other autophagy receptors, OPTN and p62, is required to link the bacterium to the autophagy pathway.

After the publication of the PN model of the xenophagic capturing of *Salmonella* by Scheidel *et al.* in December 2016 [57], novel important aspects have been published. In our model, we assumed that, in addition to LRSAM1, further E3 ubiquitin ligases participate in the ubiquitination of *Salmonella*. In two recent studies, two of these E3 ubiquitin ligases have now been detected, ariadne RBR E3 ubiquitin protein ligase 1 (ARIH1) [179] and HOIL-1-interacting protein (HOIP) [180]. In addition, OTU deubiquitinase with linear linkage specificity (OTULIN) has been identified as a DUB for M1-linked ubiquitin chains around *Salmonella*. The depletion of OTULIN results in an enhanced linear ubiquitination of the bacterium and restricts

bacterial proliferation [181]. In a recent study, a mechanism for the reactivation of mTORC1 has been demonstrated in macrophages [182]. The kinase AMPK, a negative regulator of mTOR, is targeted for lysosomal degradation by *Salmonella*, which in turn decreases autophagy. These new insights about the pathway can be extended in future work.

4.1.3 Invariant analysis

Place invariants of the Petri net

The PN model contains no P-invariants. The missing of P-invariants is usual for PN modeled as an open system. Each pathway component in the PN can be produced and degraded, i.e., the sum of tokens on the places stays not always constant.

For a more strict verification criterium, we deleted all input and output transitions to transform the PN from an open system into a closed system. The PN modeled as a closed system contains twelve P-invariants. The P-invariants and their biological interpretation are listed in Table A3 in the appendix. 61 of the 63 places are part of P-invariants. The remaining two places are *SCVdamage* and *LC3/GABARAP:AM*. The place *SCVdamage*, which represents the signal of the disruption of the SCV, is not part of any P-invariant, because the number of tokens on this place is not constant. The signal can be generated and is lost after the induction of AA starvation in the cytosol. The place *LC3/GABARAP:AM*, which describes the LC3/GABARAP-positive autophagosomal membrane, is not part of any P-invariant, because the autophagic membrane is formed and degraded, thus the number of tokens on this place is not constant.

Figure 4.6 shows the PN without input and output transitions. The places of an exemplary P-invariant, pi_4, are highlighted in red. pi_4 represents the conservation of NDP52, indicating that NDP52 is neither produced nor consumed in the PN. All 27 places, composing pi_4, describe NDP52 itself or complexes that contain NDP52 as a component.

Errors in the PN topology can be revealed by the analysis of P-invariants. For example, a mistake in the PN model would be identified, if a place that is part of pi_4 represent a complex that does not include NDP52 or a

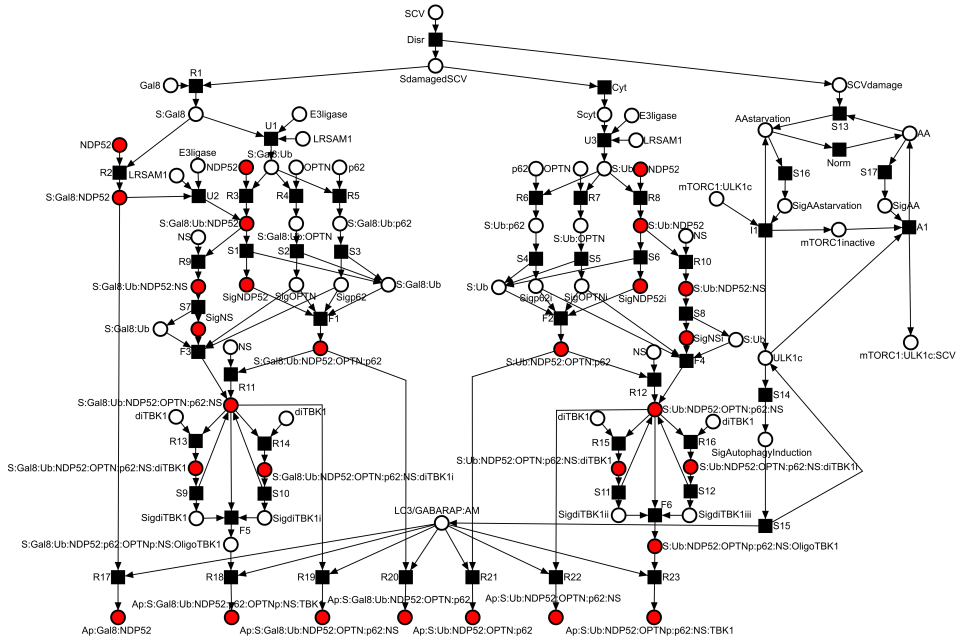

Figure 4.6 Exemplary P-invariant of the PN. The P-invariant (pi_4, red-highlighted) contains 27 places and represents the conservation of NDP52 in the system. NDP52 is a component of 43% of the places, demonstrating its key role in xenophagic capturing of *Salmonella* in epithelial cells.

place, representing a complex that includes NDP52, is not part of the P-invariant. In the final PN model depicted in Figure 4.6 no such mistakes in the PN topology could be detected, all twelve P-invariants have a meaningful biological interpretation, see Table A3 in the appendix.

For the basic pathway components, the number of complexes that contain the corresponding component, in other words, the number of places of each P-invariant is listed in Figure 4.7.

Not surprisingly, the P-invariant that comprises the most places represents *Salmonella* (pi_7). 32 of the 63 places belong to this P-invariant. The second biggest P-invariants represent NDP52 (pi_4), LRSAM1 (pi_5), and the unknown E3 ligase (pi_9), each formed by 27 of the 63 places, underlining the key role of NDP52 and ubiquitination in xenophagy. The smallest P-invariant describes the complex mTORC1 (pi_8) formed by only three of the 63 places.

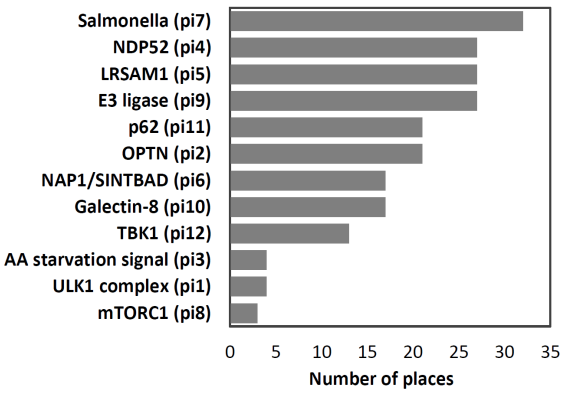

Figure 4.7 Bar chart of the P-invariants. The bar chart depicts all P-invariants of the PN in Figure 4.6 and their biological interpretation ordered according to their size.

Transition invariants of the Petri net

The PN fulfills the CTI property and consists of 19 T-invariants, which all have a meaningful, biological interpretation, see Table A4 in the appendix. One T-invariant, ti_{19}, is a trivial T-invariant, containing two transitions, *SynAA* and *DegAA*. The remaining 18 T-invariants are input-output T-invariants, of which 16 T-invariants, ti_1-ti_{16}, represent alternative ways of signal flow of the xenophagic recognition of *Salmonella*. T-invariant ti_{17} describes the escape of the bacterium from its vacuole, without a capturing to the autophagy pathway. T-invariant ti_{18} describes the functional module of mTORC1 regulation by the AA level in the cytosol.

The induced subnet of the exemplary T-invariant ti_9, PN_{ti_9}, is highlighted in Figure 4.8 (red part) and represents the ubiquitin-dependent capturing of free cytosolic *Salmonella* to the xenophagic pathway, without NAP1/SINTBAD binding and OPTN phosphorylation. The xenophagy pathway is dependent on the AA level-dependent regulation of mTORC1. The regulation of mTORC1 by the cytosolic AA level is not part of PN_{ti_9}. The mTORC1 regulation by the cytosolic AA level is reflected by the induced subnet of T-invariant ti_{18}, $PN_{ti_{18}}$, see Figure 4.8 blue part.

These two T-invariants, ti_9 and ti_{18}, in an exemplary way demonstrate that T-invariants describe functional modules, which do not reflect all biological dependencies. The regulation of mTORC1 is influenced by the disruption of the SCV, and the generation of the autophagosomal membrane is

dependent on the regulation of mTORC1 and the cytosolic AA level. These functional dependencies are not indicated by the T-invariants.

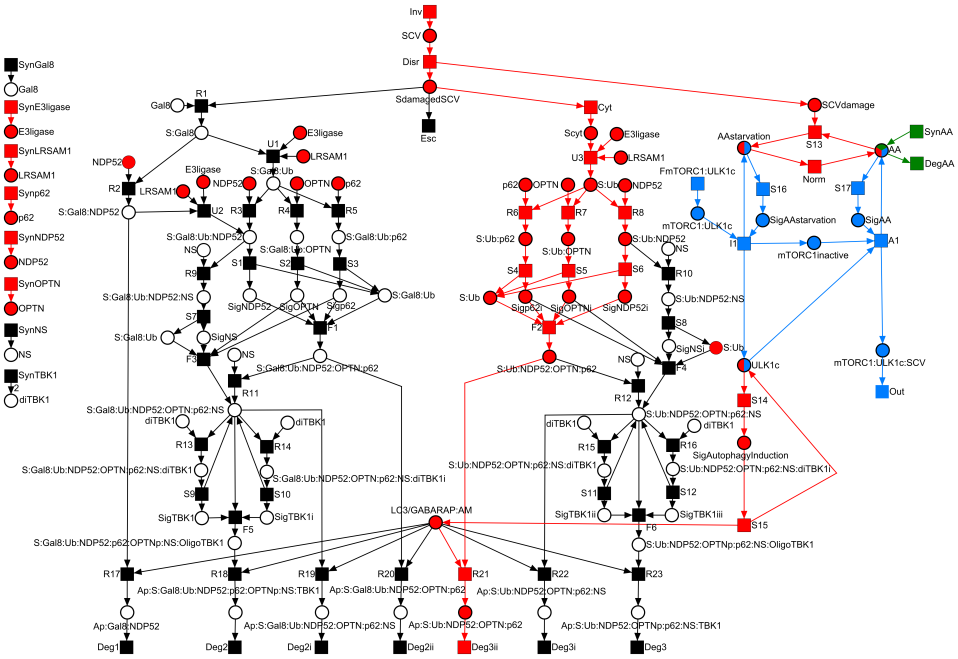

Figure 4.8 Exemplary T-invariants of the PN. T-invariant ti_9 represents the ubiquitin-dependent xenophagic recognition of free cytosol *Salmonella* (PN_{ti_9}, red-colored). T-invariant ti_{18} represents the regulation of mTORC1 by the cytosolic AA level ($PN_{ti_{18}}$, blue-colored). T-invariant ti_{19} is a trivial T-invariant, containing the two transitions *SynAA* and *DegAA* ($PN_{ti_{19}}$, green-colored).

Manatee invariants of the Petri net

The novel concept of Manatee invariants, which are linear combinations of T-invariants, was developed in this work, see Subsection *The concept of Manatee invariants* for a description of the method. Here, we applied the Manatee invariant analysis to the PN of the xenophagic capturing of *Salmonella* in epithelial cells.

The 19 T-invariants of the PN compose 19 Manatee invariants listed in Table A5 in the appendix. The subnet induced by ti_{19}, $PN_{ti_{19}}$, contains no P-invariants. Therefore, ti_{19} is also a Manatee invariant, $mi_{19} = ti_{19}$.

The subnet induced by ti_{18}, $PN_{ti_{18}}$, comprises two P-invariants. The first P-invariant is formed by the places *AAstarvation* and *SigAAstarvation* and the second P-invariant by the places *AA* and *SigAA*. The linear combination

of ti_{18} with ti_{19} resolves the second P-invariant, but the induced subnet of these two T-invariants, $PN_{ti_{18}+ti_{19}}$, still includes the P-invariant formed by the places *AAstarvation* and *SigAAstarvation*. The linear combination with any of the T-invariants ti_1-ti_{17} removes this P-invariant of $PN_{ti_{18}+ti_{19}}$ and results in 17 Manatee invariants,

$$mi_1 = ti_1 + ti_{18} + ti_{19},$$

$$mi_2 = ti_2 + ti_{18} + ti_{19},$$

$$..., \text{ and}$$

$$mi_{17} = ti_{17} + ti_{18} + ti_{19}.$$

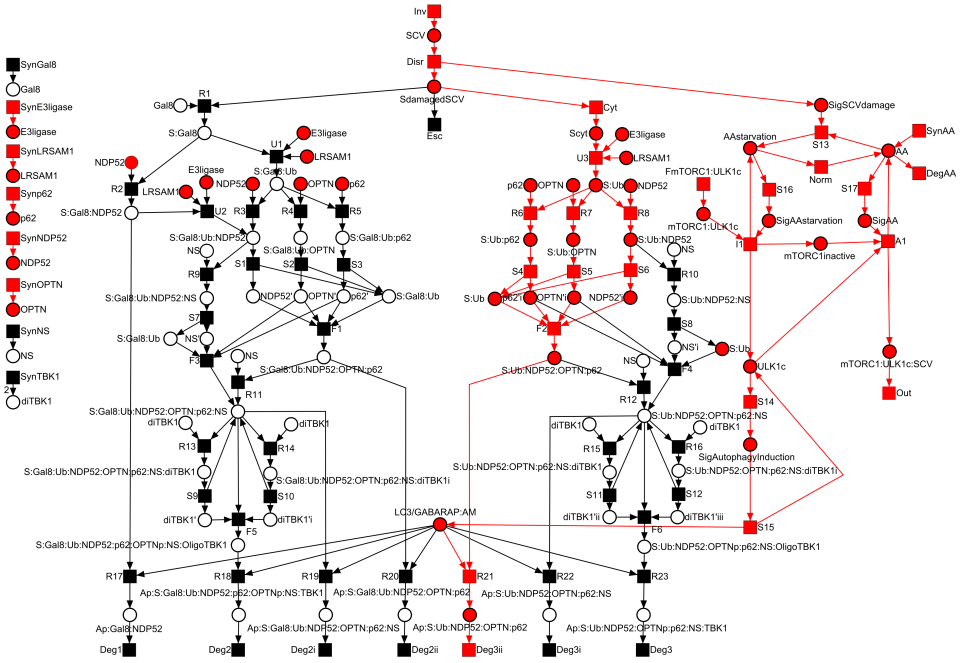

Figure 4.9 Exemplary Manatee invariant of the PN. The subnet induced by Manatee invariant $mi_9 = ti_9 + ti_{18} + ti_{19}$, PN_{mi_9}, is highlighted in red and represents the ubiquitin-dependent xenophagic recognition, which is dependent on the regulation of mTORC1 by the cytosolic AA level.

Each subnet induced by ti_1-ti_{16} has two P-invariants. The first P-invariant is formed by the places *ULK1c* and *SigAutophagyInduction* and the second P-invariant by the places *AA* and *AAstarvation*. The linear com-

bination with ti_{18} and ti_{19} resolves both P-invariants. The subnet induced by ti_{17}, $PN_{ti_{17}}$, has one P-invariant, containing the places AA and AAs-*tarvation*. The linear combination with ti_{19} removes this P-invariant and results in the Manatee invariant $mi_{18} = ti_{17} + ti_{19}$.

Figure 4.9 illustrates the induced subnet of the exemplary Manatee invariant mi_9, PN_{mi_9}. Manatee invariant mi_9 is a linear combination of the T-invariants ti_9, ti_{18}, and ti_{19}, see Figure 4.8. In contrast to the T-invariants, Manatee invariant mi_9 is able to capture the biological dependencies of the pathway. The ability of Manatee invariants to reveal the biological dependencies is of particular relevance for the computation of *in silico* knockouts.

4.1.4 *In silico* knockout analysis

To examine the model behavior in case of perturbations, we performed an *in silico* knockout analysis. At first, we analyzed the impact of transitions on the PN model as a whole. Then, we investigated the pairwise dependencies of the transitions on the places of the PN.

Impact of transitions on the Petri net

The impact of each input transition on the PN is illustrated in Table 4.2 in descending order. Transition *SynAA* has the highest impact on the PN, 100% of the Manatee invariants are affected. Transition *SynAA* represents the generation of the AA level in the cytosol. The regulation of the AA level is important for the induction of autophagy. The second highest impact on the PN model has transition *Inv* by affecting 95% of the Manatee invariants. The knockout of transition *Inv* indicates that the bacterium can not invade into the cell. One Manatee invariant, mi_{19}, remains unaffected from these knockouts, representing the generation of the cytosolic AA. The generation of AA is a general process that is independent of the bacterium invasion. The third greatest impact has transition *FmTORC1:ULK1c* by affecting 89% of the Manatee invariants. The knockout of transition *FmTORC1:ULK1c* disables the syntheses of the components of the mTORC1 and ULK1 complex and their complex formation, which are essential for the induction of autophagy.

Table 4.2 *In silico* knockouts and their impact on the PN of the xenophagic capturing of *Salmonella* in epithelial cells. The impact of each input transition, i.e., the number and percentage of affected Manatee invariants, in descending order.

Knocked out transitions	Number of affected Manatee invariants	Percentage of affected Manatee invariants
SynAA	19	100%
Inv	18	95%
FmTORC1:ULK1c	17	89%
SynNDP52	16	84%
Synp62	15	79%
SynOPTN	15	79%
SynLRSAM1	15	79%
SynE3ligase	15	79%
SynNS	12	63%
SynGal8	11	58%
SynTBK1	10	53%

The knockout of transition *SynNDP52* affects 84% of the Manatee invariants. All 16 Manatee invariants mi_1-mi_{16}, representing alternative ways of signal flow of carrying *Salmonella* to the xenophagic degradation, are affected by this knockout. This high impact demonstrates the central role of NDP52 in participating in all ways of signal flow that lead to the xenophagic recognition of *Salmonella*. The knockout of the other autophagy receptors p62 and OPTN (transitions *Synp62* and *SynOPTN*, respectively) also have a high impact on the pathway. 15 ways of signal flow of recognizing *Salmonella* for xenophagy are affected by each of these knockouts, but one way of signal flow stays always unaffected, representing the galectin-8-dependent xenophagic recognition. An equal effect can be observed by the knockout of transitions *SynLRSAM1* and *SynE3ligase*, which represent the E3-ligases that are responsible for the ubiquitination of cytosolic *Salmonella*. The input transition with the lowest impact is *SynTBK1*, 53% of the Manatee invariants are affected. Transition *SynTBK1* represents the synthesis and dimerization of TBK1. TBK1 enhances the autophagic degradation of *Salmonella*, but seems not to be an essential factor.

Pairwise dependencies of the Petri net

To investigate the influence of perturbations, like impaired protein syntheses, on the components of the xenophagic capturing of *Salmonella* pathway, we applied the *in silico* knockout analysis established in this thesis, see Sub-

section *The concept of in silico knockouts*. The application of the knockout analysis to the PN of the xenophagic capturing of *Salmonella* in epithelial cells provides a proof of principle for the novel method. The computation of the *in silico* knockouts was performed by using the software isiKnock with the settings, *Manatee invariants* and *Integrate output reaction*, see Subsection *The software isiKnock*.

The pairwise dependencies between transitions and places are compactly represented in the *in silico* knockout matrix, see Figure 4.10. Ten input transitions are assigned to the rows of the matrix and 45 places to the columns, composing a matrix of 450 entries. The knockout of the ten transitions describes the impaired invasion of *Salmonella* (transition *Inv*) and the impaired expression of proteins or complexes (transition *SynE3ligase*, *SynLRSAM1*, *SynGal8*, *Synp62*, *SynNDP52*, *SynOPTN*, *SynNS*, *SynTBK1*, *FmTORC1:ULK1c*).

The 45 columns represent all pathway components that are involved in the xenophagic capturing of *Salmonella*. The remaining 18 places of the PN, which are not depicted in the matrix are places that describe signals. Each of the 450 matrix entries shows the predicted effect of one *in silico* knockout to a certain component of the xenophagy pathway. 262 entries were predicted to be unaffected places (green) and 188 entries to be affected places (red).

For affected places, the amount of the corresponding pathway components in the experiment should be reduced in comparison to the normal, non-perturbed condition. In general, a similar amount of the pathway components should be observed for unaffected places. Due to quantitative effects of dividing bacteria, an experimental perturbation of a protein that impairs the xenophagic degradation of *Salmonella* can lead to a higher amount of bacteria inside the cell. In this case, an increased amount of pathway component can be observed for an unaffected place that represents the bacterium and is not in contradiction to the prediction.

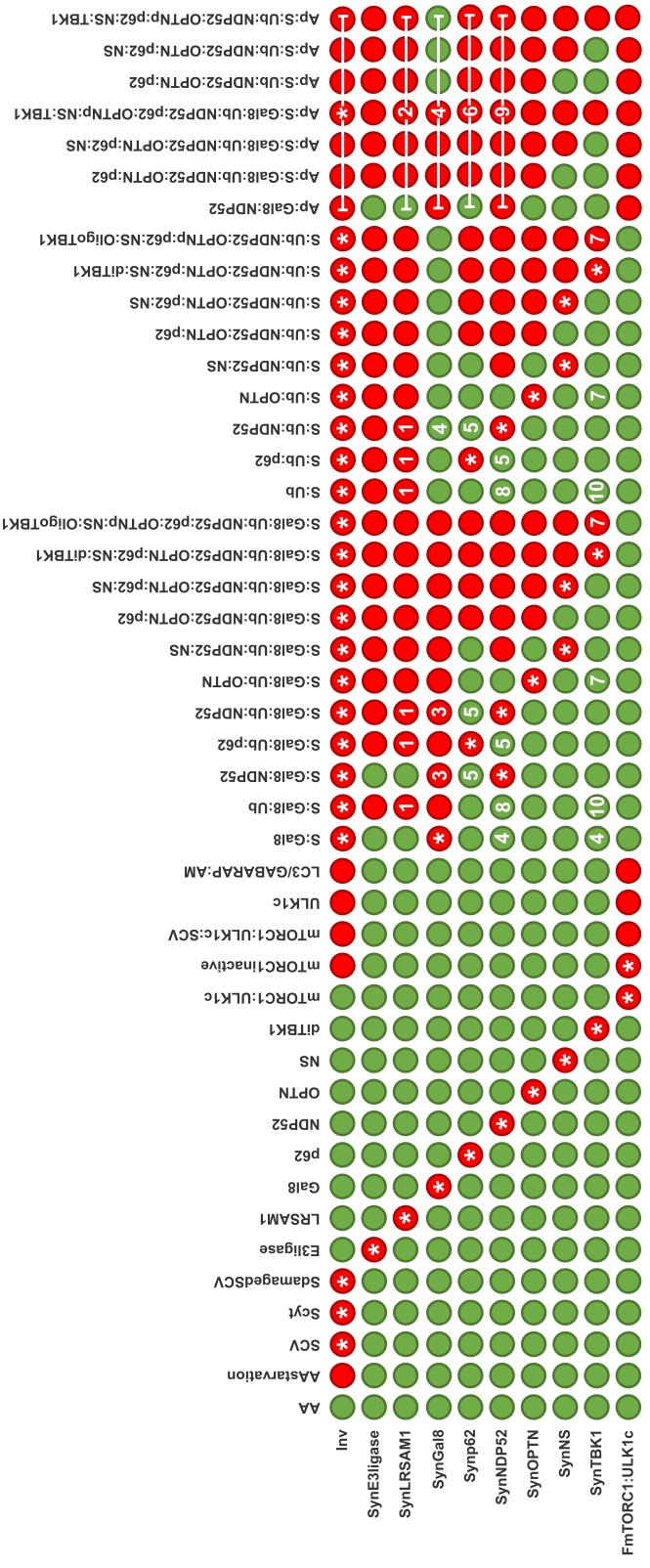

Figure 4.10 *In silico* knockouts of the xenophagic capturing of *Salmonella* in epithelial cells. The rows of the *in silico* knockout matrix show the knocked out reactions and the columns the pathway components of the xenophagic capturing of *Salmonella*. A red entry indicates an effect of the knockout and a green entry no effect. The numbers in some entries represent the reference of experimentally investigated effects: [1] Huett *et al.* [150]; [2] Huett *et al.* [150], Ng *et al.* [151]; [3] Thurston *et al.* [36], Li *et al.* [149]; [4] Thurston *et al.* [36]; [5] Cemma *et al.* [154]; [6] Zheng *et al.* [29], Cemma *et al.* [154]; [7] Wild *et al.* [30]; [8] Thurston *et al.* [31]; [9] Cemma *et al.* [154], von Muhlinen *et al.* [157], Thurston *et al.* [31]; [10] Wild *et al.* [30], Radtke *et al.* [160]. Biologically obvious results are marked by an asterisk. We summarized all seven places representing *Salmonella* trapped by the LC3/GABARAP-positive autophagosomal membrane. The knockout of these places is experimentally investigated, if the fraction of LC3/GABARAP-positive *Salmonella* has been observed in the experiments.

In general, *in silico* knockout predictions could not match with experimental perturbation data because of

- a wrong topological structure of the PN, which does not describe the correct biological dependencies,
- the experimental perturbation effects are contradictory, i.e., the same perturbation experiment results in different outcomes,
- the incorporation of literature knowledge for different cell lines can lead to inconsistent results, and
- the experimental knockout behavior is influenced by alternative pathways that are not part of the PN.

We found experimental perturbation data for 52 of the 450 matrix entries in ten studies [29–31, 36, 149–151, 154, 157, 160]. In these experiments, gene knockouts or knockdowns have been performed, and knockout effects on certain pathway components have been observed. 19 of the 52 experimentally investigated entries are unaffected places and 33 are affected places. For all the seven places, representing bacteria trapped by the LC3/GABARAP-positive autophagosomal membrane, *Ap:S:Gal8:Ub:NDP52:OPTN:p62*, *Ap:S:Gal8:NDP52*, *Ap:S:Ub:NDP52:OPTN:p62*, *Ap:S:Ub:NDP52:OPTNp:p62:NS:TBK1*, *Ap:S:Gal8:Ub:NDP52:OPTN:p62:NS*, *Ap:S:Ub:NDP52:OPTN:p62:NS*, and *Ap:S:Gal8:Ub:NDP52:OPTNp:p62:NS:TBK1*, the knockout effects are considered as experimentally investigated, if the fraction of LC3/-GABARAP-positive *Salmonella* has been observed in the experiments.

Further 54 of the 450 matrix entries are obvious from the biological perception, e.g., the impaired invasion of *Salmonella* consequently affects the presence of bacteria in the SCV. No experimental data are currently available for the remaining 344 entries, which represent hypotheses of knockout behavior that can be tested by future experimental investigations.

In the following, the effects of each *in silico* knockout will be considered, experimentally investigated effects are outlined, and some interesting knockout behavior for future experimental studies will be highlighted.

In silico* knockout of the invasion of *Salmonella The knockout of transition *Inv* generated 35 unaffected and 10 affected places and represents an impairment of the invasion process of *Salmonella* into the cells, see Figure 4.10. As a matter of course, all pathway components that include the bacterium are affected by this knockout. The AA starvation, which is provoked by the SCV disruption [171, 172], is affected by the impaired invasion and all processes triggered by AA starvation, which are the inactivation of mTORC1, activation of the ULK1 complex, mTORC1 accumulation and reactivation around the SCV, and the formation of the autophagosomal membrane. The proteins that are involved in the xenophagic capturing of *Salmonella* (places *E3ligase*, *LRSAM1*, *Gal8*, *p62*, *NDP52*, *OPTN*, *NS*, *diTBK1*, and *mTORC1:ULK1c*) are unaffected by this knockout and can still be produced in cells.

***In silico* knockout of LRSAM1 and the unknown E3 ligase** The knockouts of the transitions *SynLRSAM1* and *SynE3ligase* led to the same effects, 25 affected and 20 unaffected places and represent an impaired expression of LRSAM1 and the other unknown E3 ubiquitin ligase, respectively. In consequence, all pathway components that include the ubiquitinated bacterium are affected by these knockouts and the E3 ubiquitin ligase itself.

The treatment of HeLa cells with siRNA against LRSAM1 (siLRSAM1) has been shown to reduce the association of *Salmonella* with ubiquitin, p62, NDP52, LC3 proteins, and the fraction of *Salmonella* within autophagosomes [150, 151]. In accordance with these results, the *in silico* knockout of LRSAM1 affects ubiquitinated *Salmonella* (places *S:Ub* and *S:Gal8:Ub*), the recruitment of p62 (places *S:Ub:p62* and *S:Gal8:Ub:p62*), NDP52 (places *S:Ub:NDP52* and *S:Gal8:Ub:NDP52*), and the LC3/GABARAP-positive autophagosomal membrane (the seven places representing bacteria trapped by the LC3/GABARAP-positive autophagosomal membrane) to *Salmonella*, see Figure 4.10. Furthermore, the recruitment of the autophagy receptor OPTN to the bacterium is affected by the *in silico* knockout of LRSAM1 (places *S:Ub:OPTN* and *S:Gal8:Ub:OPTN*). The reduced localization of OPTN to *Salmonella* upon the knockout or knockdown of LRSAM1 remains

to be examined in future studies.

The perturbation of other E3 ubiquitin ligases involved in the ubiquitination of *Salmonella* have to be performed to evaluate their effect on the complexes involved in the xenophagic capturing of *Salmonella*. In two recent studies, two of these E3 ubiquitin ligases have already been identified, ARIH1 [179] and HOIP [180].

***In silico* knockout of galectin-8** The knockout of transition *SynGal8* resulted in 16 affected and 29 unaffected places and describes an impairment of the synthesis of galectin-8. This knockout affects all pathway components that include galectin-8 and galectin-8 itself.

A reduced fraction of NDP52-positive *Salmonella* at 1 h p.i. has been observed in HeLa cells depleted of galectin-8 [36,149]. The *in silico* knockout of galectin-8 affected the binding of NDP52 to galectin-8-positive *Salmonella* (places *S:Gal8:NDP52* and *S:Gal8:Ub:NDP52*), but the binding of NDP52 to ubiquitinated *Salmonella* (place *S:Ub:NDP52*) was unaffected by this knockout, see Figure 4.10. In siRNA against galectin-8 (siGal8)-treated cells, only a small amount of about 1-2% of *Salmonella* stayed NDP52-colocalized at 1 h p.i. [36, 149]. The recruitment of NDP52 to *Salmonella* at 4 h p.i. seems not to be inhibited [36], which may be explained by the recruitment of NDP52 by ubiquitin and independent of galectin-8 at later time points of the infection.

The treatment of HeLa cells with siGal8 has been shown to reduce the fraction of LC3-positive *Salmonella* [36]. In accordance with this observation, the *in silico* knockout of galectin-8 affected four of the seven places representing bacteria trapped by the LC3/GABARAP-positive autophagosomal membrane, see Figure 4.10.

***In silico* knockout of p62** 17 affected and 28 unaffected places resulted from the knockout of transition *Synp62*, which represents an impaired expression of p62. As a matter of course, all pathway components that include p62 are affected by this knockout and p62 itself.

In p62-depleted HeLa cells, a reduced percentage of LC3-positive *Salmonella* has been observed [29, 154]. In accordance, the *in silico* knockout

of p62 affected six of the seven places representing bacteria trapped by the LC3/GABARAP-positive autophagosomal membrane, see Figure 4.10. The percentage of NDP52-positive *Salmonella* is the same in p62-depleted HeLa cells, indicating an independent recruitment of p62 and NDP52 to *Salmonella* [154]. The *in silico* knockout of p62 revealed also no effect on the recruitment of NDP52 to *Salmonella* (places *S:Gal:NDP52*, *S:Ub:NDP52*, and *S:Gal:Ub:NDP52*). Furthermore, the localization of OPTN to *Salmonella* is not affected by the *in silico* knockout of p62 (places *S:Ub:OPTN* and *S:Gal:Ub:OPTN*). There are no studies available examining whether OPTN localization to *Salmonella* is independent of p62.

***In silico* knockout of NDP52** The knockout of transition *SynNPD52* describes an impaired expression of the protein NDP52 and predicted 21 affected and 24 unaffected places. In consequence, this knockout affects all pathway components that include NDP52 and NDP52 itself.

An increased fraction of ubiquitinated *Salmonella* has been observed in HeLa cells depleted of NDP52 [31]. In comparison, the *in silico* knockout of NDP52 did not affect the ubiquitination of *Salmonella* (places *S:Ub* and *S:Gal8:Ub*), see Figure 4.10. The experimentally observed increase of ubiquitinated *Salmonella* may be caused by a higher fraction of cytosolic bacteria due to an inoperable xenophagic degradation and not by a direct effect of NDP52 on the process of ubiquitination.

The treatment of HeLa cells with siRNA against NDP52 (siNDP52) has no influence on the binding of p62 to *Salmonella* [154]. Likewise, the *in silico* knockout of NDP52 revealed no effect on the recruitment of p62 to *Salmonella* (places *S:Ub:p62* and *S:Gal8:Ub:p62*) and did not affect the recruitment of OPTN to *Salmonella* (places *S:Ub:OPTN* and *S:Gal8:Ub:OPTN*), see Figure 4.10. There are no studies available examining whether OPTN localization to *Salmonella* is independent of NDP52.

No effect on galectin-8-positive *Salmonella* has been observed for HeLa cells depleted of NDP52 [36]. In accordance, the *in silico* knockout of NDP52 did not affect the localization of galectin-8 to the bacterium (place *S:Gal8*), see Figure 4.10.

Moreover, the transfection of HeLa cells with siNDP52 has been demon-

strated to reduce the fraction of LC3/GABARAP-positive *Salmonella* [31, 154, 157]. The *in silico* knockout of NDP52 also showed a negative effect on the binding of the LC3/GABARAP-positive autophagosomal membrane by affecting all seven places representing bacteria trapped by the LC3/GABARAP-positive autophagosomal membrane, see Figure 4.10.

***In silico* knockout of OPTN** The knockout of transition *SynOPTN* resulted in 17 affected and 28 unaffected places and describes an impairment of the expression of the protein OPTN. All pathway components that include OPTN are affected by this knockout and OPTN itself.

Experimental perturbation studies of OPTN that observe the influence of OPTN on the pathway components included in the PN are not available in the literature so far. The *in silico* knockout of OPTN predicted, for instance, no influence on the recruitment of NDP52, p62, and NAP1/SINTBAD to *Salmonella* (places *S:Ub:NDP52*, *S:Gal8:Ub:NDP52*, *S:Ub:p62*, *S:Gal8:Ub:-p62*, *S:Ub:NDP52:OPTN:p62:NS*, and *S:Gal8:Ub:NDP52:OPTN:p62:NS*), see Figure 4.10. Theses hypotheses can be experimentally validated in further studies.

***In silico* knockout of NAP1/SINTBAD** The PN predicted 13 affected and 32 unaffected places by the knockout of transition *SynNS*, which represents an impaired synthesis of NAP1/SINTBAD. All pathway components that include NAP1/SINTBAD are affected by this knockout and NAP1/SINTBAD itself. In the literature, experimental perturbation studies of NAP1/SINTBAD that observe the effect of NAP1/SINTBAD on any pathway components included in the PN are not available so far.

***In silico* knockout of TBK1** The knockout of transition *SynTBK1* results in 7 affected and 38 unaffected places and describes an impaired expression of the kinase TBK1. As a matter of course, this knockout affects all pathway components that include TBK1 and the TBK1 itself.

In TBK1-depleted HeLa cells, no effect on galectin-8-positive *Salmonella* has been observed [36]. In agreement with this observation, the *in silico* knockout of TBK1 did not affect the galectin-8 binding to *Salmonella* (place

S:Gal8), see Figure 4.10.

A similar fraction of *Salmonella* mutant *sifA*$^-$ that is positive for OPTN has been observed for HeLa cells depleted of TBK1 [30]. In comparison, the *in silico* knockout of TBK1 likewise did not affect the recruitment of OPTN to *Salmonella* (places *S:Ub:OPTN* and *S:Gal8:Ub:OPTN*), see Figure 4.10. The treatment of HeLa cells with siRNA against TBK1 (siTBK1) has been demonstrated to reduce the fraction of *Salmonella* mutant *sifA*$^-$ that is positive for phosphorylated OPTN (pS177) [30]. In accordance with the experimental perturbation behavior, the *in silico* knockout of TBK1 affected the phosphorylation of OPTN (places *S:Ub:NDP52:OPTNp:p62:NS:OligoTBK1* and *S:Gal8:Ub:NDP52:OPTNp:p62:NS:OligoTBK1*).

In *Tbk1*$^{-/-}$ mouse embryonic fibroblasts (MEF), an increased association of ubiquitin with *Salmonella* has been observed [160]. The fraction of ubiquitinated *Salmonella* enhances from 2 to 4 h p.i. The increased association of ubiquitin with *Salmonella* has also been demonstrated in HeLa cells at 4 h p.i. [160]. In comparison, the *in silico* knockout of TBK1 showed no effect on the ubiquitination of *Salmonella* (places *S:Ub* and *S:Gal8:Ub*). A higher fraction of ubiquitinated *Salmonella* in siTBK1-treated cells can be explained by an enhanced number of bacteria inside the cytosol caused by the impaired xenophagic degradation of *Salmonella* due to the TBK1-depletion and not by a direct effect of TBK1 on the process of ubiquitination. Another explanation may be that another function of TBK1, besides OPTN phosphorylation, may lead to a higher amount of ubiquitinated *Salmonella*. TBK1 has been reported to maintain the integrity of the SCV [160]. In contrast to the increased fraction of ubiquitinated *Salmonella* in *Tbk1*$^{-/-}$ MEF and siTBK1-treated HeLa cells, a reduced fraction of ubiquitinated *Salmonella sifA*$^-$ in HeLa cells transfected with siTBK1 has been reported 4 h p.i. [30]. The *Salmonella sifA*$^-$ is a mutant of *Salmonella* that remains predominantly in the cytosol.

***In silico* knockout of the mTORC1-ULK1 complex** The knockout of transition *FmTORC1:ULK1c* predicted 12 affected and 33 unaffected places and describes an impairment of the synthesis and formation of the protein complex mTORC1-ULK1. All pathway components that include

the mTORC1 or the ULK1 complex are affected by this knockout and the mTORC1-ULK1 complex itself.

In summary, for each of the ten *in silico* knockouts, the observed knockout behavior was in accordance with the expected. Experimental perturbation data were found for 52 of 450 predictions and matched in all of the cases. This underlines the correctness and consistency of the PN model of the xenophagic capturing of *Salmonella* and provides a proof of principle of the proposed concept of *in silico* knockouts, see Subsection *The concept of in silico knockouts*.

4.2 The stochastic Petri net of a *Salmonella*-infected epithelial cell

To investigate the dynamics of a *Salmonella*-infected cell, we developed an SPN that models a HeLa cell infected with *Salmonella* Typhimurium under experimental conditions. One simulation trajectory or simulation run of the SPN represents the infection of one individual cell. In the following, we first give an overview of the general biological processes that are included in the model and present the global architecture of the SPN.

4.2.1 The infection of epithelial cells with *Salmonella*

In experimental research, the epithelial cells are incubated within an infection medium that contains the bacteria. The infection medium or culture medium varies in its average number of *Salmonella* that are added per cell named the *multiplicity of infection* (MOI). The epithelial cells are incubated with the infection medium for a specific period of time called the *incubation time* or *infection time*. After the infection time, the cells are washed to remove non-invaded bacteria. During the infection time, the bacterium can land on the surface of the cell, see Figure 4.11. *Salmonella* have been observed to swim in close proximity to the cell surface, a process that has been termed *near surface swimming* [77]. After some time of near surface swimming, the bacterium can take off from the cell surface.

Alternatively, *Salmonella* can dock to the cell surface via the needle-like structure of the T3SS encoded by SPI-1 [10–12,34]. Effector proteins are injected by SPI-1-encoded T3SS and trigger a rearrangement of the cytoskeleton, resulting in a ruffling of the cell membrane around the bacterium [8]. A region of ruffled membrane on the cell surface is termed *ruffle* or *membrane ruffle*. Such a ruffle on the cell surface forms an obstacle, where further bacteria encounter during near surface swimming. In a cooperative manner, *Salmonella* are assumed to use preexisting ruffles to invade the epithelial cell [77, 183]. We called the process of cooperative invasion by preexisting ruffles *ruffle joining*.

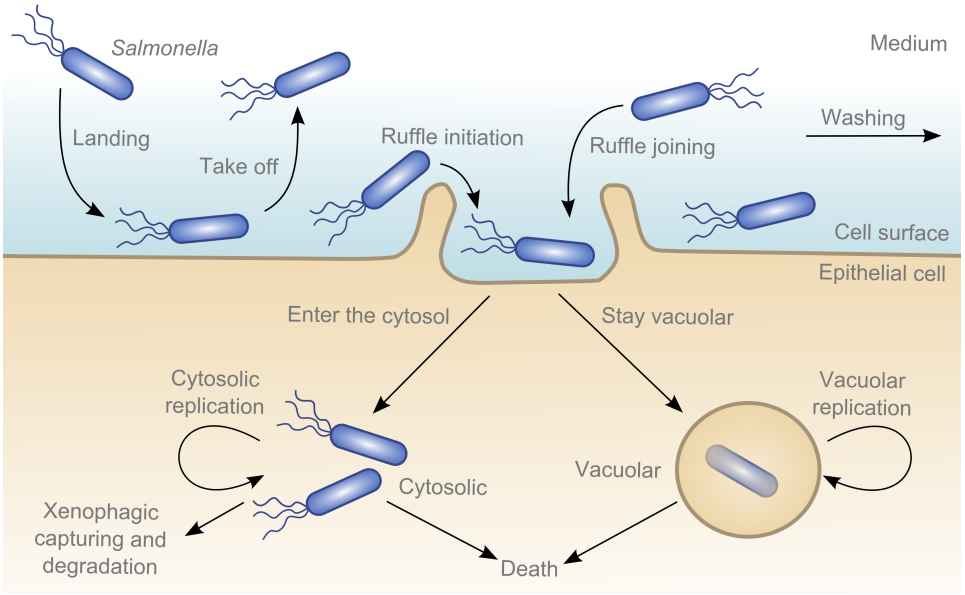

Figure 4.11 Schematic representation of the infection of a epithelial cell with *Salmonella*. Upon the bacteria are added to epithelial cells, they first land on the cell surface and perform a near surface swimming. Some bacteria take off again and swim back to the medium. Other bacteria invade the cells in a cooperative manner by the initiation of a ruffle, which is joined by further bacteria. Invasive *Salmonella* are enclosed within the SCV and start to replicate. Some bacteria enter to the cytosol, where they can be captured and degradated by xenophagy. Later in the infection, the cells populated by *Salmonella* die.

Once inside the epithelial cell, the bacterium is surrounded by the SCV. The majority of bacteria stays inside the SCV and start to replicate. A fraction of *Salmonella* disrupts the membrane of the SCV and enters the cytosol [10–12,34]. The cytosolic bacteria can be recognized and degradated

by xenophagy [29–31, 34–36]. At late time points of the infection, i.e., when the number of bacteria inside the cell is high, the epithelial cell seems to die [16].

4.2.2 Topology of the stochastic Petri net

We constructed an SPN that contains the processes of a *Salmonella*-infected epithelial cell that are illustrated in Figure 4.11. Table A6 in the appendix lists all places, their biological meaning, and their initial marking. The transitions and their stochastic rate constants are described in Table A7 in the appendix.

The graphical representation of the SPN model is illustrated in Figure 4.12. We graphically grouped the SPN into seven functional parts:

- generation of the infection medium (Figure 4.12, yellow part)
- washing of the epithelial cell (Figure 4.12, green part)
- *Salmonella* at different states of the infection (Figure 4.12, black part)
  - landing and take off
  - ruffle initiation and joining
  - entering the SCV and the cytosol
  - bacterial proliferation
- fate of the epithelial cell (Figure 4.12, purple part)
- xenophagic capturing of cytosolic *Salmonella* (Figure 4.12, turquoise part)
- divisibility of *Salmonella* (Figure 4.12, red part)
- cell death (Figure 4.12, blue part)

In the following, each part of the SPN is described. The arcs of the reaction equations are named after the transitions. Each transition is associated to a stochastic rate constant termed $c_{transition\ name}$.

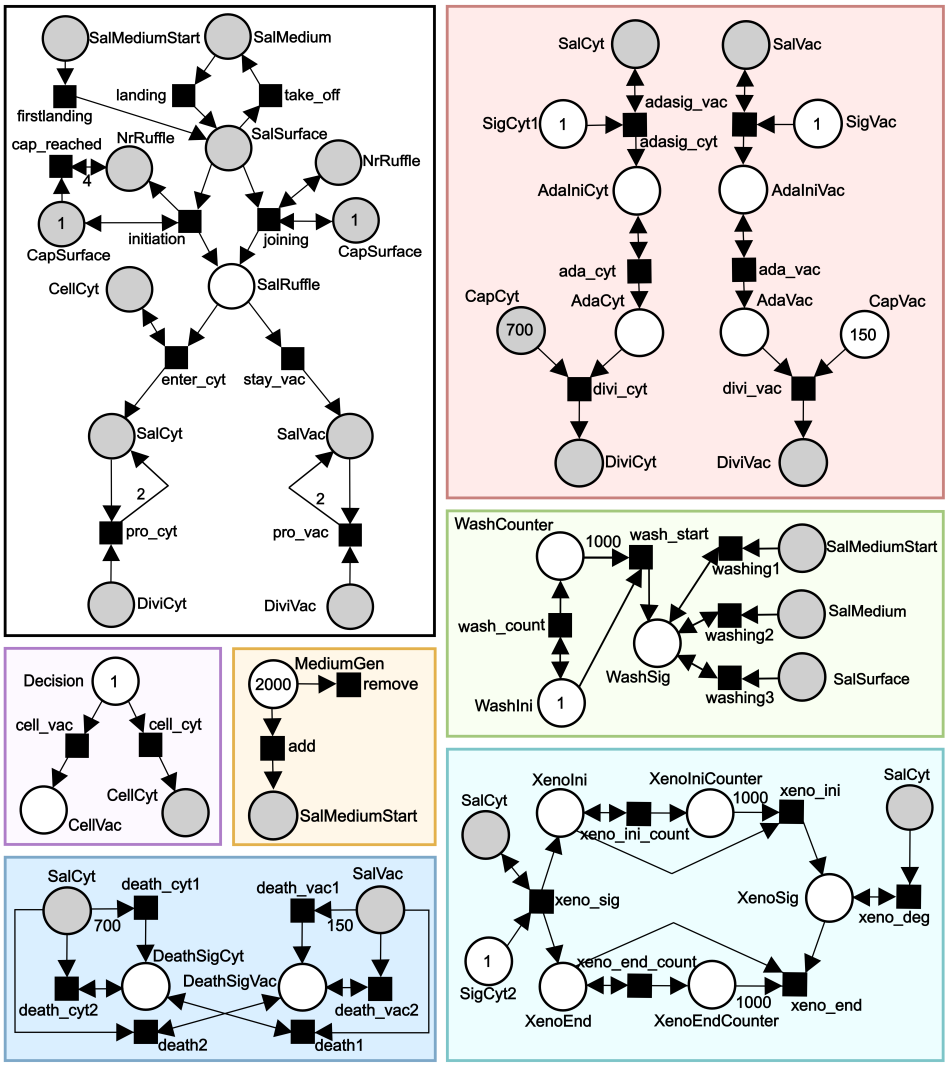

Figure 4.12 The SPN of a *Salmonella*-infected epithelial cell. The SPN is graphically grouped into seven functional parts: generation of the infection medium (yellow part), washing process (green part), *Salmonella* at different states of the infection (black part), fate of the cell (purple part), xenophagic capturing of cytosolic *Salmonella* (turquoise part), divisibility of the bacteria in the cytosol and vacuole (red part), and the cell death (blue part). All gray places are logical places. The depicted tokens represent the initial marking. For a description of the places and transition, see Table A6 and Table A7 in the appendix.

Generation of the infection medium

The MOI is the ratio of bacteria in the infection medium to cells. For the infection of cells with bacteria, often a particular MOI is indicated in the experiment. However, the actual MOI may differ due to uncertainty in the experimental measurements by the generation of the infection medium. Also, the number of bacteria to infect an individual cell may vary from the indicated MOI due to an irregular distribution of the infection medium. For example, an indicated MOI of 100 in an experiment can be generated by 1000 bacteria in the infection medium to infect 10 cells. In average, 100 bacteria can potentially infect an individual cell. The number of bacteria to infect an individual cell can deviate from the MOI of 100.

To simulate the stochastic fluctuations of the number of bacteria to infect an individual cell, the generation of the infection medium is modeled by the processes

$$\begin{aligned} \mathit{MediumGen} &\xrightarrow{\mathit{remove}} \varnothing, \\ \mathit{MediumGen} &\xrightarrow{\mathit{add}} \mathit{SalMediumStart}, \end{aligned}$$

where the initial marking of the place *MediumGen* restricts the maximum number of bacteria to infect an individual cell. The marking of *SalMediumStart* represents the actual number of *Salmonella* in the medium to infect an individual cell.

For $M_0(\mathit{MediumGen}) = 2000$, the simulations are limited to the maximum MOI of 2000. Each token on *MediumGen* represents a bacterium that can either choose to be added to the infection medium by transition *add* or to be removed by transition *remove*. The transitions *remove* and *add* are associated with the stochastic rate constants c_{remove} and c_{add}, respectively.

The probability distribution of the MOI of one simulation, i.e., the number of bacteria to infect an individual cell is given by the binomial distribution

$$B(\mathrm{m}|p,n) = \binom{n}{\mathrm{m}} p^{\mathrm{m}}(1-p)^{n-\mathrm{m}},$$

where m = number of bacteria per individual cell, $n = M_0(\mathit{MediumGen})$,

and $p = \frac{c_{add}}{c_{remove}+c_{add}}$.

The MOI, i.e., the averaged number of bacteria per cell, is given by

$$\mathrm{MOI} = M_0(MediumGen) \times \frac{c_{add}}{c_{remove} + c_{add}}.$$

Washing of the epithelial cell

The infection time ends with the washing of the cells to remove non-invaded *Salmonella*. The initiation of the washing process is modeled by the processes

$$WashIni \xrightarrow{wash\_count} WashCounter + WashIni,$$
$$1000\ WashCounter + WashIni \xrightarrow{wash\_start} WashSig,$$

with $M_0(WashIni) = 1$, $M_0(WashCounter) = 0$, and $M_0(WashSig) = 0$. The place *WashIni* represents a signal for the one-time initiation of the washing process. The place *WashCounter* describes a time counter, and *WashSig* represents the signal for the onset of the washing process.

For $M_0(WashIni) = 1$, tokens are accumulated on place *WashCounter* by the occurrence of transition *wash_count*. After the place *WashCounter* reaches 1000 tokens, the transition *wash_start* generates one token on place *WashSig*. The token on *WashIni* is removed, i.e., $M(WashIni) = 0$ to prevent the initiation of further washing processes. For $M_0(WashSig) = 1$, the washing process starts, and non-invaded bacteria in the infection medium or on the cell surface are removed by the three processes:

$$SalMediumStart + WashSig \xrightarrow{washing1} WashSig,$$
$$SalMedium + WashSig \xrightarrow{washing2} WashSig,$$
$$SalSurface + WashSig \xrightarrow{washing3} WashSig,$$

where *SalMediumStart*, *SalMedium*, and *SalSurface* are all places that represent *Salmonella* outside the cell.

Landing and take off

We assumed that *Salmonella* need some time to adjust to the medium at the beginning of the infection time. To model this adjustment, the number of *Salmonella* in the medium is represented by two places, *SalMediumStart* and *SalMedium*. *SalMediumStart* represents the bacteria in the medium at the beginning of the infection time and *SalMedium* represents the adapted bacteria in the medium. We assumed that after a first landing on the cell surface the bacterium has been adapted to the infection medium.

The first landing is modeled by the process

$$SalMediumStart \overset{firstlanding}{\longrightarrow} SalSurface,$$

where the place *SalSurface* denotes the number of bacteria on the cell surface, with $M_0(SalSurface) = 0$. After some time of near surface swimming, the bacterium can take off from the cell surface:

$$SalSurface \overset{take\_off}{\longrightarrow} SalMedium,$$

with $M_0(SalMedium) = 0$. The occurrence of the process *take_off* leads to the take off of one bacterium from the cell surface back to the medium. Afterwards, the bacterium is adapted to the medium. The landing of adapted *Salmonella* on the cell surface is modeled by the process

$$SalMedium \overset{landing}{\longrightarrow} SalSurface.$$

Ruffle initiation and joining

It has been observed that *Salmonella* form ruffles on the cell surface [8]. The formation of a new ruffle is modeled by the process

$$SalSurface + CapSurface \overset{initiation}{\longrightarrow} SalRuffle + NrRuffle + CapSurface,$$

with $M_0(CapSurface) = 1$, $M_0(SalRuffle) = 0$, and $M_0(NrRuffle) = 0$. The place *SalRuffle* denotes the total number of bacteria located in ruffles. The place *CapSurface* describes a signal for the capability of the cell surface to

accept additional bacteria, and *NrRuffle* counts the number of ruffles on the cell surface.

For $M_0(CapSurface) = 1$, sufficient space on the cell surface is left to form a new ruffle by transition *initiation*. The counter *NrRuffle* increases each time a new ruffle is initiated. Note that the attachment of *Salmonella* to the cell via the SPI-1-encoded T3SS has been shown to be irreversible [184]. In the SPN, a bacteria located in a ruffle will never leave the ruffle again.

It is assumed that the cooperative invasion is caused by bacteria joining preexisting ruffles [77, 183]. We modeled the ruffle joining of *Salmonella* by the process

$$SalSurface + NrRuffle + CapSurface \xrightarrow{joining} SalRuffle + NrRuffle + CapSurface.$$

If at least one ruffle has formed on the cell surface, i.e., $M(NrRuffle) \geq 1$, a bacterium can join a ruffle by transition *joining*. For $M(CapSurface) = 1$, the cell surface has sufficient space that bacteria can join ruffles.

The entry of *Salmonella* into epithelial cells has been observed to occur at a limited number of possible entry points [8, 77, 185, 186]. Typically, one to three ruffles are formed on the cell surface. Multiple bacteria has been viewed in the localization of one ruffle [16, 187]. For high MOI, physical limitations of bacterial invasion in HeLa cells infected with *Salmonella* Typhi has been shown [185].

We modeled the physical limitations by a maximum number of ruffles on the cell surface, i.e., by the limiting process

$$4\,NrRuffle + CapSurface \xrightarrow{cap\_reached} 4\,NrRuffle.$$

If the number of ruffles on the cell surface reaches four, i.e., $M(NrRuffle) = 4$, transition *cap_reached* takes place and the marking of *CapSurface* drops to zero. For $M(CapSurface) = 0$, additional bacteria on the cell surface can not be accepted. Further physical limitations may concern the number of bacteria on the surface or the number of internalized bacteria.

Entering the SCV and the cytosol

Inside the cell, the decision of a bacterium to get cytosolic or stay in the vacuole seems not to be an independent choice, but appears to be more a cell-dependent process [78]. We assumed that there are cells with the capability to host cytosolic *Salmonella*, i.e., *cytosolic-capable* cells and there are also *cytosolic-incapable* cells, see Subsection *Fate of the epithelial cell* for a detailed description. However, it has been observed that cells containing cytosolic *Salmonella* can additionally contain vacuolar bacteria [17]. We assumed that in cells with the ability to harbor cytosolic *Salmonella*, the individual bacterium can still decide whether to go into the cytosol or to stay in the vacuole.

The process of *Salmonella* staying in the SCV is modeled by

$$SalRuffle \xrightarrow{stay\_vac} SalVac,$$

with $M_0(SalVac) = 0$. The place *SalVac* denotes the total number of bacteria in the SCV. The process of *Salmonella* entering the cytosol is modeled by

$$SalRuffle + CellCyt \xrightarrow{enter\_cyt} SalCyt + CellCyt,$$

with $M_0(CellCyt) = 0$ and $M_0(SalCyt) = 0$. The place *CellCyt* describes a signal for the capability of the cell to host cytosolic bacteria, for more information see Subsection *Fate of the epithelial cell*. The place *SalCyt* represents the total number of *Salmonella* with cytosolic access. Only if $M(CellCyt) = 1$, transition *get_cyt* can produce tokens on *SalCyt*. In other words, only if the cell is cytosolic-capable, a bacterium can reach the cytosol by the occurrence of transition *get_cyt*.

In the SPN model, *Salmonella* are directly removed from the ruffle to the cytosol. For reasons of simplification, we did not included an intermediated step, where the bacterium is first located in a damaged SCV and then becomes cytosolic. It has been shown that the vacuolar escape seems to be an early event, which happens soon after the internalization [17], and the damaged SCV is a transient state between the intact SCV and bacteria free

in the cytosol [145].

In summary, cytosolic-capable cells, i.e., $M(CellCyt) = 1$, can result in cells with exclusively *Salmonella* in the cytosol, cells with exclusively *Salmonella* in the SCV, cells with cytosolic and vacuolar *Salmonella*, or uninfected cells without invaded bacteria. Cells with exclusively *Salmonella* in SCV or uninfected cells can origin from cytosolic-incapable cells, i.e., $M(CellCyt) = 0$.

Bacterial proliferation

The proliferation of *Salmonella* in the cytosol and the SCV is modeled by the second order autocatalytic reactions

$$SalCyt + DiviCyt \overset{pro\_cyt}{\longrightarrow} 2\,SalCyt,$$
$$SalVac + DiviVac \overset{pro\_vac}{\longrightarrow} 2\,SalVac,$$

where *DiviCyt* and *DiviVac* were introduced to model the lag phase and the stationary phase of cytosolic and vacuolar proliferation, respectively, see Subsection *Divisibility of Salmonella*. Each time transition *pro_cyt* takes place, a token is removed from places *SalCyt* and *DiviCyt*, and two tokens are produced on *SalCyt*, i.e., one bacterium in the cytosol multiplies to two bacteria. In the same way, transition *pro_vac* represents the proliferation of vacuolar *Salmonella*.

Fate of the epithelial cell

It has been suggested that the opportunity of *Salmonella* to get access to the cytosol may not only be the decision of the individual bacterium but is rather a cell-dependent process [78]. In case of an independent escape strategy, the chance of a cell to host cytosolic *Salmonella* would raise with the number of invaded bacteria or increasing MOI. On the contrary, it has been reported that the fraction of cytosolic *Salmonella* is independent from the MOI [78]. We assumed that only in a subpopulation of cells, the bacterium can escape from the SCV and enters the cytosol.

The decision whether a cell is able to host cytosolic *Salmonella* is mod-

eled by the processes

$$Decision \xrightarrow{cell\_cyt} CellCyt,$$
$$Decision \xrightarrow{cell\_vac} CellVac.$$

The place *Decision* with the initial marking $M_0(Decision) = 1$ represents the cell before the decision to become a cytosolic-capable or cytosolic-incapable cell. By the firing of transition *cell_cyt* or *cell_vac*, a token can either be produced on place *CellCyt* or on place *CellVac*. $M(CellCyt) = 1$ represents a cytosolic-capable cell, whereas $M(CellVac) = 1$ represents a cytosolic-incapable cell.

Xenophagic capturing of cytosolic *Salmonella*

Salmonella inside the cytosol recognized by xenophagic pathway [29–31, 34–36]. The process of xenophagic degradation is depicted in the turquoise part of the SPN in Figure 4.12. The degradation of *Salmonella* by xenophagy is modeled by the process

$$SalCyt + XenoSig \xrightarrow{xeno\_deg} XenoSig,$$

with $M_0(XenoSig) = 0$. The place *XenoSig* represents the signal for xenophagic degradation. The xenophagic degradation is active if $M(XenoSig) = 1$, otherwise xenophagy is inactive. For $M(XenoSig) = 1$, tokens are consumed on place *SalCyt* by the firing of transition *xeno_deg*. In other words, bacteria are removed from the cytosol via xenophagic degradation.

Xenophagy has been shown to restrict the growth of *Salmonella* [30, 31, 34–36]. On the other hand, in some cases, cytosolic *Salmonella* seem to evade xenophagic recognition and replicate with high rates inside the cytosol [14, 16, 17]. Xenophagy has been suggested to capture cytosolic *Salmonella* only in the early phase of infection [34, 171, 172]. Around 3-4 h p.i. the autophagic targeting may be prevented by the reactivation of mTOR [171, 172]. There are also assumptions that *Salmonella* can benefit from the autophagy pathway [188]. Summarized, the xenophagic recognition of cytosolic *Salmonella* is temporally restricted to the early phase of

the infection and xenophagy is not in all cells able to completely suppress the bacterial growth in the cytosol.

The initiation and termination of xenophagy is induced by the process

$$SigCyt2 + SalCyt \xrightarrow{xeno\_sig} XenoIni + XenoEnd + SalCyt,$$

with $M_0(SigCyt2) = 1$, $M_0(XenoIni) = 0$, and $M_0(XenoEnd) = 0$. The place *SigCyt2* represents a signal for the presence of *Salmonella* in the cytosol. The place *XenoIni* denotes a signal for the initiation and *XenoEnd* a signal for the termination of xenophagy. If one bacterium reaches the cytosol, i.e., $M(SalCyt) \geq 1$, by the firing of transition *xeno_sig*, the token is consumed from *SigCyt2* and produced on *XenoIni* and *XenoEnd*, i.e., $M(XenoIni) = M(XenoEnd) = 1$. In other words, the signals for the initiation and termination of xenophagy are induced.

Xenophagy is initiated by the processes

$$XenoIni \xrightarrow{xeno\_ini\_count} XenoIni + XenoIniCounter,$$
$$1000\, XenoIniCounter + XenoIni \xrightarrow{xeno\_ini} XenoSig,$$

with $M_0(XenoIniCounter) = 0$. The place *XenoIniCounter* describes a time counter. For $M(XenoIni) = 1$, tokens are accumulated on place *XenoIniCounter* by transition *xeno_ini_count*. If the time counter, place *XenoIniCounter*, reaches 1000 tokens, transition *xeno_ini* generates one token on place *XenoSig* to activate xenophagic degradation. By the firing of this transition, the token on *XenoIni* is removed, i.e., $M(XenoIni) = 0$, to stop the time counter and prevent further xenophagy initiations. Equivalent to the initiation of xenophagy, the termination of xenophagy is modeled by the processes

$$XenoEnd \xrightarrow{xeno\_end\_count} XenoEnd + XenoEndCounter,$$
$$1000 XenoEndCounter + XenoEnd + XenoSig \xrightarrow{xeno\_end} \varnothing,$$

with $M_0(XenoEndCounter) = 0$.

Divisibility of *Salmonella*

The doubling time of bacteria is dependent on their environmental conditions, such as space, nutrients, pH, and temperature [189,190]. A change in the environmental conditions leads to a *lag phase*, a time period the bacteria need to adjust to the new environment. During this time, the bacterial proliferation is impaired. Also later in the infection, the proliferation decreases due to limited space and nutrients. This phase of bacterial growth is called *stationary phase*.

We combined the effects of the lag phase and stationary phase on the bacterial growth into a feature that we call *divisibility*. The divisibility is dependent on the *adaptability* and the *capacity*. Under adaptability, we understand the effects of the lag phase on the bacterial proliferation. The capacity represents the effects of the stationary phase. The divisibility of cytosolic and vacuolar *Salmonella* is represented by the places *DiviCyt* and *DiviVac*, respectively. In the following, we focus on the explanation of the processes that affect the divisibility of cytosolic *Salmonella*. The divisibility of the vacuolar *Salmonella* is modeled in the same way.

The adaptability to the cytosol modeled by the place *AdaCyt* can be increased by the processes

$$SigCyt1 + SalCyt \xrightarrow{adasig\_cyt} AdaIniCyt + SalCyt,$$
$$AdaIniCyt \xrightarrow{ada\_cyt} AdaCyt + AdaIniCyt,$$

with $M_0(SigCyt1) = 1$, $M_0(AdaIniCyt) = 0$, and $M_0(AdaCyt) = 0$. The place *SigCyt1* describes a signal for the presence of *Salmonella* in the cytosol, the place *AdaIniCyt* represents a signal for the initiation of the adaptability process of *Salmonella* in the cytosol, and the place *AdaCyt* represents the adaptability to the cytosol.

If a bacterium reaches the cytosol, i.e., $M(SalCyt) \geq 1$, the token on *SigCyt1* is consumed and produced on place *AdaIniCyt* by transition *adasig_cyt*. For $M(AdaIniCyt) = 1$, the adaptability, i.e., place *AdaCyt*, increases by the firing of transition *ada_cyt*.

Each time a token is produced on place *AdaCyt*, it is consumed and

produced on place *DiviCyt* by the process

$$AdaCyt + CapCyt \xrightarrow{divi\_cyt} DiviCyt,$$

where the place *CapCyt* represents the capacity of the cytosol.

To compute the cytosolic capacity of HeLa cells, we assumed a volume of 2600 μm^3 [191]. *Salmonella* have been reported to be 2-5 μm in length with a diameter in the range of 0.7-1.5 μm [192]. This results in an average bacteria volume of $\pi r^2\ h = 3.14\ \mu m^3$, with $r = 0.55\ \mu m$ and $h = 3.5\ \mu m$. As theoretical upper limit, 828 bacteria fit into one HeLa cell. Due to cellular structures and geometrical reasons, this theoretical upper limit is overestimated. We suggested up to 700 bacteria per HeLa cell, i.e., $M_0(CapCyt) = 700$. The capacity can also be interpreted as a measure for the restricting environmental conditions, like nutrient availability or space.

The maximum divisibility of cytosolic *Salmonella* is dependent on the initial marking of *CapCyt* and thus $max\ M(DiviCyt) = 700$. For $M(DiviCyt) = 700$, *Salmonella* proliferate with the highest achievable doubling time, see Subsection *Bacterial proliferation*. Each time a bacterium multiplies, a token on *DiviCyt* is consumed. This reduces the doubling time by reason of a lack of space or nutrients and resembles the stationary phase, when the number of cytosolic bacteria converges towards 700.

Equivalent to the divisibility of cytosolic *Salmonella*, the divisibility of *Salmonella* in the SCV is modeled by the processes

$$SigVac + SalVac \xrightarrow{adasig\_vac} AdaIniVac + SalVac,$$
$$AdaIniVac \xrightarrow{ada\_vac} AdaVac + AdaIniVac,$$
$$AdaVac + CapVac \xrightarrow{divi\_vac} DiviVac.$$

with $M_0(CapVac) = 150$, i.e., suggesting a maximum space for in total up to 150 bacteria enclosed in the SCV.

Cell death

To model the death of infected cells with cytosolic *Salmonella*, we included the processes

$$700\, SalCyt \xrightarrow{death\_cyt1} DeathSigCyt,$$
$$SalCyt + DeathSigCyt \xrightarrow{death\_cyt2} DeathSigCyt,$$

with $M_0(DeathSigCyt) = 0$. The place *DeathSigCyt* represents a signal that the cell undergoes cell death due to a high number of cytosolic *Salmonella*. If the number of *Salmonella* in the cytosol reaches 700, i.e., $M(SalCyt) \geq 700$, the 700 tokens on place *SalCyt* are consumed by transition *death_cyt1*. We defined 700 as the upper limit of bacteria in the cytosol in HeLa cells, see Subsection *Divisibility of Salmonella*. Remaining tokens on place *SalCyt* are removed by transition *death_cyt2*. Equivalent to the death of cells with cytosolic *Salmonella*, the death of cells with vacuolar *Salmonella* is modeled by the processes

$$150\, SalVac \xrightarrow{death\_vac1} DeathSigVac,$$
$$SalVac + DeathSigVac \xrightarrow{death\_vac2} DeathSigVac,$$

where the place *DeathSigVac* represents a signal that the cell undergoes cell death due to a high number of vacuolar *Salmonella*.

For cells containing cytosolic and vacuolar *Salmonella*, we included the processes

$$SalVac + DeathSigCyt \xrightarrow{death1} DeathSigCyt,$$
$$SalCyt + DeathSigVac \xrightarrow{death2} DeathSigVac,$$

to remove vacuolar bacteria in cells that die as a result of a high number of cytosolic bacteria and to degrade cytosolic bacteria in cells that die as a result of a high number of vacuolar bacteria, respectively.

The SPN models cell death like a process that happens in late time points of the infection, when the number of intracellular bacteria is high as it has been observed by Malik-Kale *et al.* [16]. In polarized, human IEC, Knodler *et*

al. supposed that cell death represents a strategy of bacterial dissemination into neighboring cells [14]. They assumed that colonic epithelial cells are occupied by a huge amount of cytosolic *Salmonella* and are extruded from the epithelium monolayer into the intestinal lumen and undergo caspase-1-dependent cell death.

4.2.3 Parametrization and verification of the stochastic Petri net

The kinetic parameters of the SPN model can be divided into three sets. The first set is formed by processes that take place immediately after the process has the possibility to occur, i.e., when the transition gets enabled. These processes are all characterized by a stochastic rate constant with a high value of $1000\,1/sec$. The following 18 parameters belong to this first group: c_{wash_start}, $c_{washing1}$, $c_{washing2}$, $c_{washing3}$, c_{divi_cyt}, c_{divi_vac}, c_{adasig_cyt}, c_{adasig_vac}, c_{xeno_sig}, $c_{cap\_reached}$, $c_{xeno\_ini\_count}$, $c_{xeno\_end\_count}$, c_{death1}, c_{death2}, c_{death_cyt1}, c_{death_cyt2}, c_{death_vac1}, and c_{death_vac2}.

The second set are parameters that model the desired experimental conditions, like the MOI (c_{remove} and c_{add}) and the infection time (c_{wash_count}). Table 4.3 summarizes values of the stochastic rate constants c_{remove} and c_{add} for MOI in the range of 4 to 500. Depending on the required MOI for the simulation, the stochastic rate constants c_{remove} and c_{add} were chosen. The generation of the infection medium occurs on a short timescale of 10^{-3} sec.

Table 4.3 Parameters for the MOI. Values of the stochastic rate constants c_{remove} and c_{add} are listed for various MOI, given $M_0(MediumGen) = 2000$.

MOI	c_{remove} **[1/sec]**	c_{add} **[1/sec]**
500	750	250
250	875	125
125	937.5	62.5
75	962.5	37.5
63	968.5	31.5
50	975	25
31	984.5	15.5
16	992	8
8	996	4
4	998	2

Depending on the desired infection time for the simulation, the stochastic rate constant c_{wash_count} was selected. Table 4.4 summarizes values of

c_{wash_count} for infection times in the range of 5 to 30 min.

Table 4.4 Parameters for the infection time. Values of the stochastic rate constant c_{wash_count} for various infection times are listed.

Infection time [min]	c_{wash_count} **[1/sec]**
5	3.33
9	1.85
10	1.67
15	1.11
20	0.83
25	0.66
30	0.56

A common indication of experimental measurements is the time period p.i., which represents the time interval between the washing and the measurement. For the SPN, the time period p.i. is given by the simulation time minus the infection time.

For example, an experimental measurement of infected cells at 20 min p.i. with 10 min infection time and MOI of 50 can be simulated by the SPN model with a simulation time of 30 min and the stochastic rate constants $c_{remove} = 975\,1/sec$, $c_{add} = 25\,1/sec$ (see Table 4.3), and $c_{wash\_count} = 1.67\,1/sec$ (see Table 4.4). Note that the infection time and the MOI of one individual simulation can differ in stochastic variation from the average infection time and the MOI listed in Table 4.4 and Table 4.3, respectively.

The third set of parameters determines the dynamics of the stages of a *Salmonella* infection, see Table 4.5. The 16 entries in Table 4.5 give first kinetic parameters describing the *Salmonella* infection in epithelial cells. For each parameter, the source of the experimental data is listed. Only for the adjustment of the time period of the lag phases, c_{ada_cyt} and c_{ada_vac}, no experimental data were available.

Parametrization of transitions *firstlanding*, *landing*, and *take_off*

The median time period of near surface swimming has been observed to be 1.5 sec [77]. We assumed an exponential distributed time period of near surface swimming. This determined the stochastic rate constant c_{take_off} for transition *take_off*, which is given by

$$c_{take\_off} = 1/1.5\ sec = 0.67\,1/sec.$$

Table 4.5 Kinetic parameters of a *Salmonella*-infected epithelial cell.

Parameter	Value [1/sec]	Source
$c_{firstlanding}$	0.0019	Misselwitz *et al.* [77, 79]
$c_{landing}$	0.0384	Misselwitz *et al.* [77]
c_{take_off}	0.67	Misselwitz *et al.* [77]
$c_{initiation}$	0.0005	Misselwitz *et al.* [77, 79]
$c_{joining}$	0.005	Misselwitz *et al.* [77]
c_{get_cyt}	0.004	Knodler *et al.* [17]
c_{stay_vac}	0.006	Knodler *et al.* [17]
c_{pro_cyt}	0.000000595	Malik-Kale *et al.* [16]
c_{pro_vac}	0.000000411	Malik-Kale *et al.* [16]
c_{cell_cyt}	350	Thurston *et al.* [31]
c_{cell_vac}	650	Thurston *et al.* [31]
c_{xeno_ini}	0.56	Tattoli *et al.* [171, 172], Birmingham *et al.* [34]
c_{xeno_end}	0.069	Tattoli *et al.* [171, 172]
c_{xeno_deg}	0.00037	Knodler *et al.* [17], Malik-Kale *et al.* [16]
c_{ada_cyt}	0.167	NA
c_{ada_vac}	0.036	NA

The concentration of *Salmonella* in proximity to the cell surface has been measured by fluorescence microscopy [77]. 2.75×10^{-4} *Salmonella* per μm^2 have been reported for a MOI of 1.5. Assuming an adherent HeLa cell with a diameter of 20 μm and an area of 314 μm^2, in average 0.0864 *Salmonella* are in proximity to the cell surface of one cell. Under steady-state conditions of landing and take off, the mean number of *Salmonella* near the cell surface of one individual cell is given by

$$\langle M(SalSurface) \rangle = \frac{c_{landing}}{c_{take\_off}} \times \langle M(SalMedium) \rangle,$$

which determines the stochastic rate constant $c_{landing} = 0.0384\,1/sec$ for $\langle M(SalSurface) \rangle = 0.0864$, $c_{take\_off} = 0.67\,1/sec$, and $\langle M(SalMedium) \rangle = \text{MOI} = 1.5$.

For the stochastic rate constant $c_{firstlanding}$, we chose a 20 times lower value than for the stochastic rate constant $c_{landing}$, i.e.,

$$c_{firstlanding} = \frac{c_{landing}}{20} = 0.0019\,1/sec$$

to reproduce the experimental data by Misselwitz *et al.* [77, 79], see Figure 4.13A and Figure 4.13B.

Parametrization of transitions *initiation* and *joining*

The stochastic rate constants $c_{initiation}$ and $c_{joining}$ were adapted to reproduce the experimental data shown by Misselwitz *et al.* [77, 79]. In their experiment, 150 HeLa cells have been incubated with *Salmonella* for 9 min at MOI in the range of 4-500. The percentage of cells possessing at least one ruffle has been quantified. We simulated the SPN 2000 times for the same conditions as in the experiment, i.e., 9 min infection time and corresponding MOI. Figure 4.13A depicts the mean fraction of cells possessing ruffles. For our choice of the stochastic rate constant $c_{initiation} = 0.0005\,1/sec$, the simulation reproduces the experimental data of Misselwitz *et al.* [77], see Figure 4.13A.

Since the formation of ruffles requires the irreversible binding of at least one bacterium [184], the percentage of cells possessing ruffles can also be considered as the proportion of infected cells. The fraction of infected cells is called the *infection efficiency*. Figure 4.13B shows the infection efficiency of *Salmonella* for a infection time of 20 min and a MOI ranging from 1 to 1024. The predicted infection efficiency is in accordance with the measured infection efficiency by Misselwitz *et al.* [79], see Figure 4.13B.

To model a significant cooperative effect of bacterial invasion [77, 183], the probability of bacteria joining preexisting ruffles has to be chosen higher than the probability of the formation of a new ruffle, i.e., $c_{joining} > c_{initiation}$. The stochastic rate constant $c_{joining}$ is adapted to reproduce the experimental data of Misselwitz *et al.*, Figure 10B middle [77]. In their experiment, the number of *Salmonella* per ruffle, above and under the cell surface, has been quantified four times in 25 HeLa cells. In the SPN, we do not distinguish between bacteria above and under the cell surface of a ruffle. To compare the simulations with the experimental data, we summed up the number of bacteria above and under the cell surface presented by Misselwitz *et al.*, Figure 10B middle [77] to the total number of *Salmonella* per membrane ruffle, see gray line in Figure 4.13C. In accordance with the experimental conditions, we simulated the SPN with an infection time of 9 min at various MOI in the range of 4 to 500. For each MOI, the number of bacteria per membrane ruffle was quantified in the simulations with at least one ruffle,

i.e., M($NrRuffle$) ≥ 1. The stochastic rate constant $c_{joining} = 0.005\,1/sec$ of joining ruffles, which is 10 times higher than the stochastic rate constant $c_{initiation} = 0.0005\,1/sec$ of ruffle initiation, reproduces the experimental data of Misselwitz *et al.*, see Figure 4.13C. The number of *Salmonella* per ruffle increases with enhancing MOI. At a common MOI in the range of 63 to 125, there are three to five bacteria located in one ruffle. For high MOI, e.g., 500, the number of bacteria clustering on a ruffle reaches 13 bacteria.

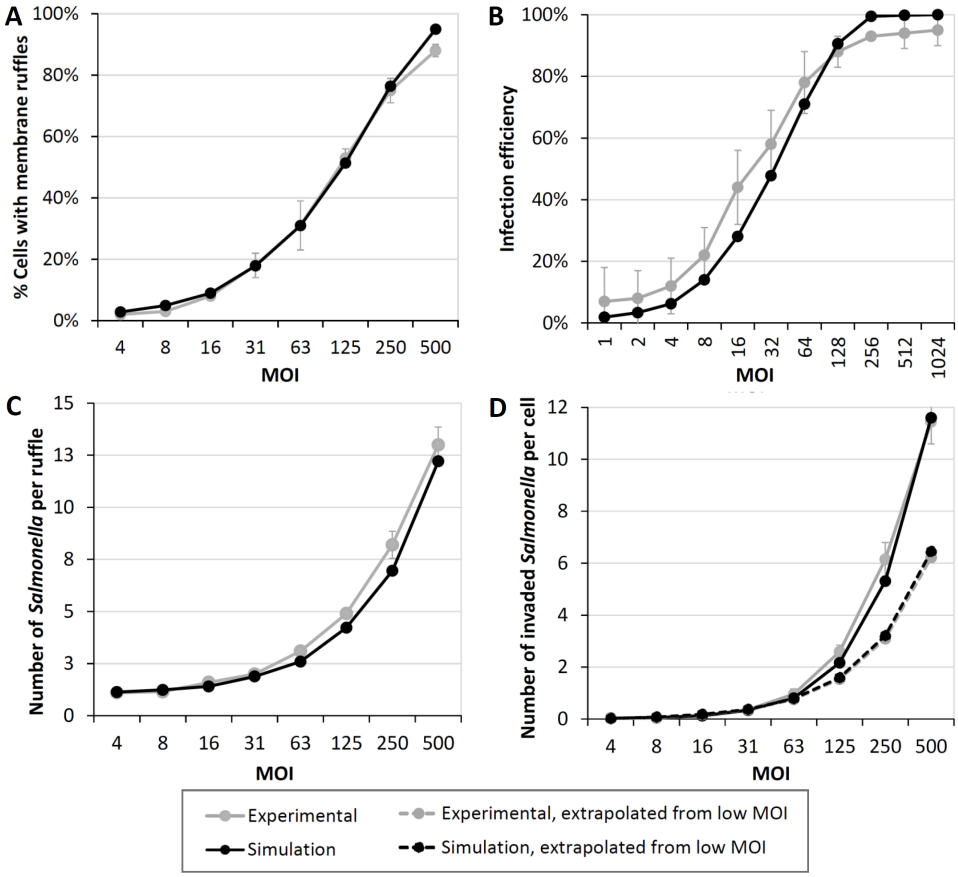

Figure 4.13 Invasion of *Salmonella* in epithelial cells. The black lines indicate the simulated data and the gray lines the experimental data presented by Misselwitz *et al.* [77, 79]. (A) Percentage of cells possessing ruffles (9 min infection time). (B) Infection efficiency, i.e., proportion of infected cells (20 min infection time). (C) Number of *Salmonella* per ruffle (9 min infection time). (D) Number of invaded *Salmonella* per cell. For each MOI, the number of invaded *Salmonella* per cell were computed by multiplying the number of *Salmonella* per membrane ruffle in B with the fraction of cells possessing ruffles in A. The dashed lines are extrapolated from low MOI, assuming a linear increase of invasion.

In accordance to Misselwitz *et al.*, Figure 10B right [77], we multiplied

the fraction of cells possessing ruffles (see Figure 4.13A) with the number of *Salmonella* per ruffle (see Figure 4.13C). Misselwitz *et al.* named the product as "invaded *Salmonella* per cell". Figure 4.13D shows the number of invaded *Salmonella* per cell for increasing MOI in the range of 4 to 500. By the assumption of no cooperative behavior of the bacterial invasion, a linear increase would be expected. We extrapolated from low MOI to high MOI, see Figure 4.13D dashed lines. The extrapolated line is much lower than the simulated data, displaying the cooperative invasion of *Salmonella*. The cooperative effect of bacterial invasion by clustering on ruffles has been experimentally demonstrated by Misselwitz *et al.* [77], see gray lines in Figure 4.13C. The predicted invaded *Salmonella* per cell are in agreement with the experimental data. The simulation of the SPN model demonstrates that the cooperative effect of *Salmonella* shown in the experiments [77, 183] can be reproduced by a 10 times higher probability of ruffle joining than ruffle initiation, this corresponds to $c_{joining} = 10 \times c_{initiation}$, see Table 4.5.

It can be assumed that the area of ruffled membrane, containing multiple bacteria is considerably larger than the size of ruffles with one or only a few bacteria. An increase in the ruffle size, i.e., an expansion of the size of the obstacles on the cell surface, may enhance the cooperative effect of ruffle joining by further bacteria. Since the simulation of the SPN are in quantitative accordance with the experimental measurements [77, 79], see Figure 4.13B, we did not include a dependency between the geometric size of a ruffle and the ruffle joining into the SPN.

Parametrization of transitions *get_cyt* and *stay_vac*

The proportion of cytosolic or vacuolar *Salmonella* in cytosolic-capable cells is determined by the stochastic rate constants c_{get_cyt} and c_{stay_vac} of the transitions *get_cyt* and *stay_vac*, respectively. The stochastic rate constants c_{get_cyt} and c_{stay_vac} were chosen to reproduce the experimental data shown by Knodler *et al.* in Figure 2 [17]. Knodler *et al.* infected HeLa cells with *Salmonella* and enumerated the bacterial load and the fraction of cytosolic *Salmonella* in cells that contain at least one cytosolic bacterium. The bacterial load is the number of total bacteria, i.e., vacuolar and cytosolic, per cell.

HeLa cells have been infected with *Salmonella* at MOI in the range of 50-100 and have been quantified at 1 h p.i. Unfortunately, there are no experimental data available immediately after the infection. At 1 h p.i., there can be effects of xenophagy and proliferation, see Subsection *Xenophagic capturing of cytosolic Salmonella* and Subsection *Bacterial proliferation*, respectively. According to the experimental conditions, the SPN was simulated at an average MOI of 75 for 1 h and 10 min (incl. 10 min infection time). A high number of 3000 simulation runs was performed, which results in 240 cells with cytosolic *Salmonella*, i.e., $M(SalCyt) \geq 1$. For these simulations, the total number of bacteria (vacuolar and cytosolic) and the fraction of cytosolic *Salmonella* from the total bacterial load were quantified, see Figure 4.14. Except for stochastic variations, the simulation results are in quantitative accordance with the experimental data for $c_{get\_cyt} = 0.004\,1/sec$ and $c_{stay\_vac} = 0.006\,1/sec$, compare with Knodler *et al.*, Figure 2 [17].

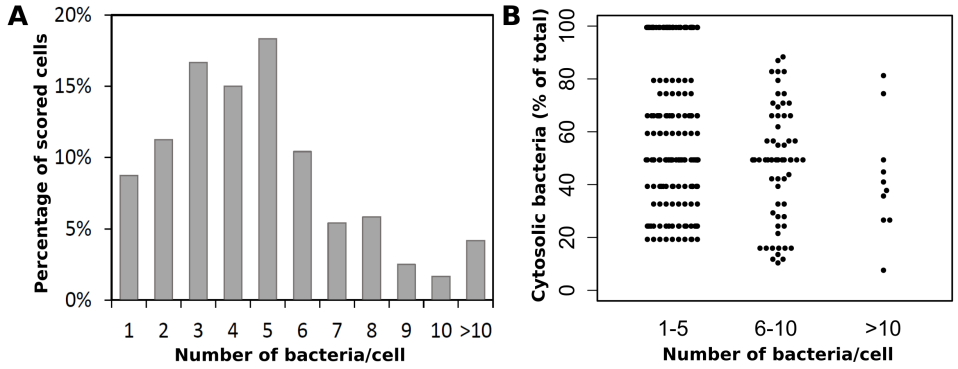

Figure 4.14 Predicted bacterial load of cells with cytosolic *Salmonella*. In 240 simulated cells that are predicted to include at least one cytosolic bacteria, i.e., $M(SalCyt) \geq 1$, the number and the composition of the bacterial load were quantified at 1 h p.i. (10 min infection time, MOI of 75). (A) The percentage of cells are scored for each the bacterial load (number of total bacteria, i.e., vacuolar and cytosolic, per cell). (B) The fraction of cytosolic *Salmonella* from the total bacterial load for cells containing 1-5 bacteria, 6-10 bacteria, and >10 bacteria. Each dot depicts one simulation, i.e., one cell. The simulated data fit the experimental data presented by Knodler *et al.* in Figure 2 [17].

Similar to the distributions measured experimentally [17], the predicted bacterial load in cells with cytosolic *Salmonella* is broadly distributed, ranging from 1 to more than 10 bacteria per cell, see Figure 4.14A. The fraction of cytosolic *Salmonella* in cells with a high bacterial load (6-10 bacteria,

and >10 bacteria per cell) is in most of the cases lower than the fraction of vacuolar *Salmonella*, see Figure 4.14B. If a correlation between the SCV damage and the bacterial load exists, we would expect a higher number of cytosolic bacteria in cells with a high bacterial load. The simulation data agree with the hypothesis about no correlation between the SCV damage and the bacterial load of the cells [17].

Parametrization of transitions *pro_cyt* and *pro_vac*

For the adjustment of the proliferation rate of cytosolic and vacuolar *Salmonella*, the stochastic rate constants c_{pro_cyt} and c_{pro_vac} of transitions *pro_cyt* and *pro_vac* have to be determined. The proliferation inside the cytosol has been demonstrated to be much faster than inside the SCV, due to ideal life conditions, such as a nutrient-rich environment, sufficient space, and neutral pH [11, 14, 15, 17, 144, 193]. The term *hyper-replication* has been introduced to describe this phenotype of fast-replicating *Salmonella* inside the cytosol, which results in more than 50-100 bacteria per cell [14, 17]. In colonic epithelial cells, a doubling time of ∼20 min for cytosolic *Salmonella* has been observed [14]. In HeLa cells, Malik-Kale *et al.* observed the growth of cytosolic *Salmonella* [16]. To distinguish between cytosolic and vacuolar bacteria, they used fluorescent dextran, a marker of the endocytic pathway that accumulates within the SCV [193]. To reproduce the experimental data of Malik-Kale *et al.*, Figure 4A [16], we chose a slightly slower doubling time of 40 min for cytosolic *Salmonella* in HeLa cells. This corresponds to a proliferation rate of $0.000417\,Salmonella/sec$ and determines the stochastic rate constant c_{pro_cyt}, which is given by

$$c_{pro\_cyt} = \frac{0.000417}{max\, M(DiviCyt)}\, 1/sec = 0.000000595\, 1/sec,$$

where $max\, M(DiviCyt) = 700$.

The simulated growth of *Salmonella* in the cytosol is depicted in Figure 4.15A. For ten simulation runs, where $M(SalCyt) \geq 1$, we plotted the fold change vs. 2.5 h p.i. of cytosolic *Salmonella*. The predicted cytosolic growth by the SPN model is similar to the experimental growth of dextran-negative (cytosolic) *Salmonella*, compare with Malik-Kale *et al.*,

Figure 4A [16]. Similar to the cytosolic growth observed experimentally, a late onset of proliferation between 4 and 5 h p.i. was predicted by the SPN. In the simulations, the late onset is caused by the xenophagic degradation of cytolic *Salmonella* in the first hours of the infection and not by a long lag phase of cytosolic bacteria, see Subsection *Xenophagic capturing of cytosolic Salmonella*. We assumed that in the early hours of the infection the xenophagic recognition and degradation restricts the bacterial growth in the cytosol and causes the late onset of proliferation between 4 and 5 h p.i. This suggestion is encouraged, by the detection of bacterial growth of cytosolic bacteria as early as 4 h p.i. in NDP52-depleted cells [31].

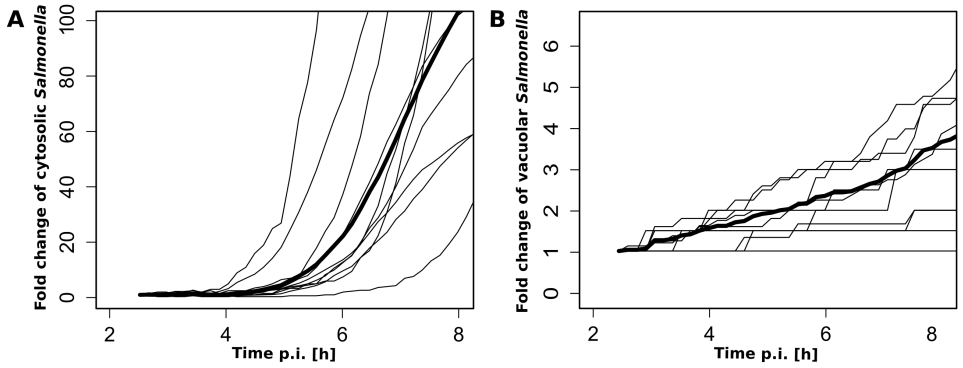

Figure 4.15 Simulated growth of cytosolic and vacuolar *Salmonella*. The fold change vs. 2.5 h p.i. of (A) cytosolic *Salmonella* and (B) vacuolar *Salmonella* was quantified in 10 min intervals for the indicated time points (10 min infection time, MOI of 50). The mean fold change is depicted by the thick line. The predicted growth of *Salmonella* is similar to the experimental growth shown by Malik-Kale *et al.* in Figure 4 [16].

In colonic epithelial cells, the average doubling time for *Salmonella* inside the SCV and the cytosol has been measured to be $\geq$95 min [14]. Consequently, the proliferation inside the SCV has to be much slower than inside the cytosol. Malik-Kale *et al.* measured a 3 fold increase from 2.5 to 9 h p.i. for vacuolar *Salmonella* [16]. This corresponds to a doubling time of approximately $\sim$4 h 30 min for vacuolar bacteria and results in a proliferation rate of 0.0000617 $Salmonella/sec$. To achieve a maximum doubling time of 4 h 30 min for a bacterium, the stochastic rate constant was set to

$$c_{pro\_vac} = \frac{0.0000617}{max\, M(DiviVac)}\, 1/sec = 0.000000411\, 1/sec,$$

where $max\, M(DiviVac) = 150$.

The predicted growth of vacuolar *Salmonella* is shown in Figure 4.15B. For ten simulation runs, where $M(SalVac) \geq 1$, the fold change of vacuolar *Salmonella* was quantified. The predicted growth of vacuolar *Salmonella* is similar to the experimental growth of dextran-positive (vacuolar) *Salmonella* depicted by Malik-Kale *et al.* in Figure 4B [16].

Parametrization of transitions *cell_cyt* and *cell_vac*

The chance of a cell to become cytosolic-capable or cytosolic-incapable is determined by the ratio of the stochastic rate constants c_{cell_cyt} and c_{cell_vac} of the transitions *cell_cyt* and *cell_vac*, respectively. The fraction of cells with hyper-replicating *Salmonella*, i.e., cells suggested to contain cytosolic *Salmonella*, has been determined to be around 8% for all measured MOI in the range of 25 to 800 [78]. In another study, ∼10% of cells has been detected to contain ubiquitinated bacteria at 2 and 4 h p.i. [31]. Ubiquitin has been demonstrated to serve as a marker for *Salmonella* present in the cytosol [12]. Knodler *et al.* reported that approximately 9% of the cells harbors hyper-replicating *Salmonella* at 8 h p.i. [17]. In a study of Malik-Kale *et al.*, at 6 h p.i. ∼15% of the infected cells contained cytosolic *Salmonella*, which were stained with anti-LPS antibody [16]. They also reported that at 8 h p.i. approximately 10% of the cells contained hyper-replicating *Salmonella*.

Xenophagy has been shown to restrict the proliferation of *Salmonella* in the cytosol [30, 31, 34–36]. For this reason, the 8% to 15% of cells, containing cytosolic bacteria [12, 16, 17, 31, 78] is not necessarily the fraction of the cytosolic-capable cells. In a study of Thurston *et al.*, the autophagy receptor NDP52 has been depleted and the fraction of HeLa cells containing ubiquitinated *Salmonella* has been determined for 2 and 4 h p.i. [31]. At 2 h p.i., ∼23% of the cells contains cytosolic *Salmonella* and ∼45% at 4 h p.i.

Based on these experimental findings, we assumed a model, where around 35% of the cells are cytosolic-capable. To generate 35% of cytosolic-capable and 65% cytosolic-incapable cells, the stochastic rate constant was set to $c_{cell\_cyt} = 350\, 1/sec$ and $c_{cell\_vac} = 650\, 1/sec$.

Parametrization of transitions *xeno_ini*, *xeno_end*, and *xeno_deg*

To specify in which period of time xenophagy is active, i.e., $M(XenoSig) = 1$, the stochastic rate constants c_{xeno_ini} and c_{xeno_end} of the transitions *xeno_ini* and *xeno_end* have to be adjusted. It has been suggested that xenophagy is induced by AA starvation, which in turn is triggered by membrane damage and is only active in the early time of the infection [171, 172]. Furthermore, at 1 h p.i., 20% of total bacteria are already associated with LC3 proteins [34]. We chose $c_{xeno\_ini} = 0.56\,1/sec$ to activate xenophagy, i.e., $M(XenoSig) = 1$, after ∼30 min the first bacterium reaches the cytosol. At 3-4 h p.i., xenophagy has been reported to be prevented by intracellular AA level normalization and reactivation of mTOR [171, 172]. The stochastic rate constant $c_{xeno\_end} = 0.069\,1/sec$ leads to the deactivation of xenophagy, i.e., $M(XenoSig) = 0$, after ∼4 h the first bacterium reaches the cytosol.

The efficiency of xenophagic degradation can be configured by the stochastic rate constant c_{xeno_deg} of transition *xeno_deg*. We determined the stochastic rate constant c_{xeno_deg} by reproducing the experimental data of Malik-Kale *et al.* [16] and Knodler *et al.* [17]. From their infected cells, $9.2 \pm 3.2\%$ or $10 \pm 4\%$ contained hyper-replicating *Salmonella* at 8 h p.i. [16, 17]. We predicted a fraction of 8.2% cells with cytosolic, hyper-replicating *Salmonella* at 8 h p.i. for $c_{xeno\_deg} = 0.00037\,1/sec$, see Figure 4.17.

In a simplified way, the SPN models xenophagy as a signal that is either present or absent. If xenophagy is active, i.e., $M(XenoSig) = 1$, the probability of an individual bacterium to be degradated by transition *xeno_deg* is always constant. Maybe, the initiation and termination of xenophagy is more a continuous process in which the efficiency of xenophagy varies, depending from time point of the infection.

Parametrization of transitions *ada_cyt* and *ada_vac*

By the adjustment of the stochastic rate constants c_{ada_cyt} and c_{ada_vac} of transitions *ada_cyt* and *ada_vac*, respectively, the time period of the lag phase of cytosolic and vacuolar *Salmonella* can be changed. Unfortunately, there are no experimental data available about the lag phase of *Salmonella* inside a HeLa cell. It has been observed that bacterial growth in the cytosol

is initiated around 4 h p.i. [16]. However, we assumed that this is caused by xenophagic degradation in the first hours of the infection and not by a long lag phase, see Subsection *Parametrization of transitions pro_cyt and pro_vac*. We determined the stochastic rate constant $c_{ada\_cyt} = 0.167\,1/sec$ to produce the highest achievable doubling time, i.e., $M(DiviCyt) = 700$, after ∼1 h the first bacterium reaches the cytosol. To achieve a maximum doubling time after ∼1 h the first bacterium reaches the SCV, we chose the stochastic rate constant $c_{ada\_vac} = 0.036\,1/sec$.

In summary, the proposed 16 parameters listed Table 4.5 give the first estimations of the kinetic rates of a *Salmonella*-infected cell. For this set of parameters, the SPN reproduces the experimental data from the publications we used to parameterize the SPN. In future work, the parameters of the SPN have to be validated in an iterative way [39], by quantitative predictions that can be tested in future experiments. Especially, to elucidate the role of xenophagy in the late onset of bacterial proliferation inside the cytosol, further experiments would be instructive.

4.2.4 Predictions of the stochastic Petri net

In the following, we applied the SPN model as a tool to predict the effects of the infection time and the MOI on the infection efficiency and to simulate the composition and distribution of the bacterial load.

Infection efficiency

The SPN predicted the infection efficiency of *Salmonella* in HeLa cells for MOI in the range of 4 to 500 and infection times in the range of 5 to 30 min, see Figure 4.16. As expected, the predicted infection efficiency enhances with increasing MOI and infection time. For example, for a high MOI of 500, nearly 100% of the cells are predicted to be infected with *Salmonella* from an infection time of 15 min. For a low MOI, e.g., MOI of 4, even for a high infection time of 30 min, only around 12% of the cells are infected. Depending on the biological questions, the MOI and the infection time have to be selected for the experiments. A low MOI can

be experimentally motivated by the avoidance of multiple infection events of an individual cell. The predictions of the SPN model provide valuable information for future experiments to study *Salmonella* infections.

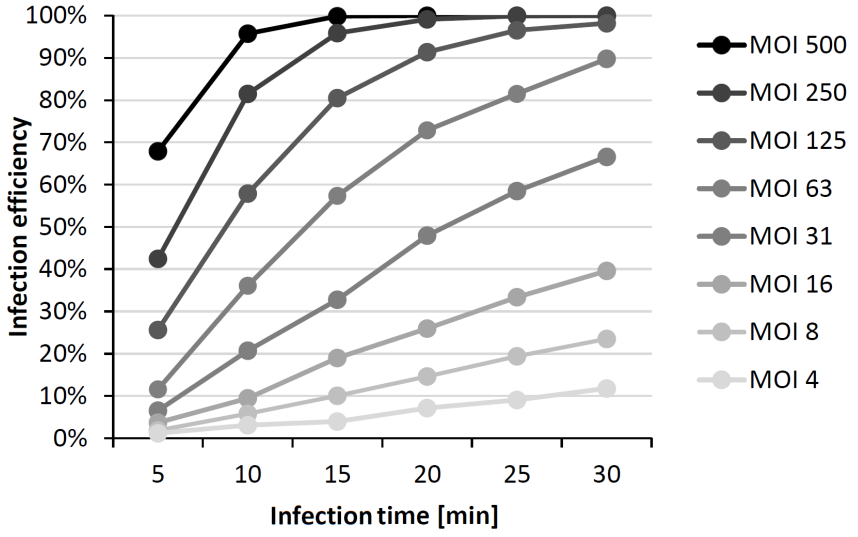

Figure 4.16 Predicted infection efficiency of epithelial cells with *Salmonella*. The infection efficiency, i.e., percentage of infected cells, was predicted for MOI ranging from 4 to 500 and infection times ranging from 5 to 30 min.

Composition of the bacterial load

To investigate the composition and distribution of the bacterial load per cell over time, we predicted the number of bacteria for ∼150 infected cells ($M(SalCyt) \geq 1$ or $M(SalCyt) \geq 1$), see Figure 4.17. Each dot represents the total number of *Salmonella* in one cell. The simulation results are in quantitative accordance with the experimental data shown in Malik-Kale *et al.*, Figure 1B [16] and Knodler *et al.*, Figure 1 [17]. In their experiments, intracellular *Salmonella* has been enumerated by fluorescence microscopy and no distinction has been made between cytosol or vacuolar *Salmonella*. In the simulation, we can differentiate between cytosol or vacuolar bacteria. A gray dot in Figure 4.17 depicts the predicted bacterial number of one individual cell with exclusively *Salmonella* in SCV. A black dot represents the total number of bacteria per cell, including cytosolic *Salmonella*.

At 2 h p.i., all of the cells contain less than 20 bacteria, independent of

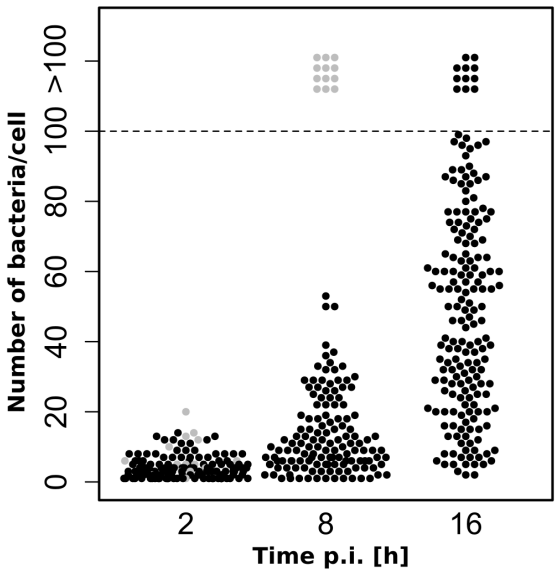

Figure 4.17 Predicted composition and distribution of the bacterial load. The bacterial load was counted per infected cell, i.e., $M(SalCyt) \geq 1$ or $M(SalCyt) \geq 1$ ($n = \sim$150 cells, 10 min infection time, MOI of 50). Each dot represents the total bacterial load of one cell, i.e., number of cytosolic and vacuolar *Salmonella*. Cells depicted by gray dots contain cytosolic bacteria and by black dots host exclusively bacteria inside the SCV.

their location in the cytosol or the SCV. At 8 h p.i., the cells have separated into two groups. The first group represents cells hosting exclusively vacuolar bacteria. These cells show bacterial growth at this time point of the infection, but most of the cells still contain less than 20 bacteria. The maximum is 53 vacuolar bacteria in one cell at 8 h p.i. By contrast, in the second group, all of the cells contain more than 100 bacteria. In the experiments of Malik-Kale *et al.* [16] and Knodler *et al.* [17], it was assumed that this group represents the hyper-replicating cytosolic *Salmonella*. The simulation of the SPN supports this hypothesis. All cells that contain more than 100 bacteria at 8 h p.i. are predicted to harbor cytosolic *Salmonella*. Note that these cells can also include vacuolar *Salmonella*. A proportion of 8.2% of the cells belongs to this second group of cytosolic *Salmonella*, which is in agreement with the fraction of hyper-replicating bacteria measured in the experiments, $9.2 \pm 3.2\%$ in Knodler *et al.* [17] and $10 \pm 4\%$ in Malik-Kale *et al.* [16]. At 16 h p.i., the number of bacteria per cell is broadly distributed, ranging from two to more than 100 *Salmonella* per cell. All cells are predicted to host

exclusively vacuolar *Salmonella*. All cells that contain cytosolic *Salmonella* have died at this late phase of infection, see Subsection *Cell death*. The cells with more than 100 *Salmonella* per cell are predicted to be cells with bacteria enclosed in SCV.

The term *hyper-replication* for cells with more than 50-100 bacteria per cell has been proposed to describe cells with fast-replicating *Salmonella* inside the cytosol [14, 17]. The simulation of the SPN demonstrates that slow-growing vacuolar bacteria can also reach more than 50-100 bacteria at late time points of the infection. According to the definition of *hyper-replication* [14, 17], these cells would be classified as hyper-replicative and thereby misidentified as cell with cytosol bacteria. The term *hyper-replication* to describe cytosolic *Salmonella* based on the bacterial number is valid at 8 h p.i., but not at 2 h p.i. and 16 h p.i., see Figure 4.17.

4.3 Method development in computational systems biology

In this section, the developed methods of this work are described. We introduced a novel concept of *in silico* knockouts, which considers the effects of knockouts on the steady-state behavior of the model and the functional dependencies of a pathway. In this context, we established the concept of Manatee invariants, which are linear combinations of T-invariants, and their suitability for *in silico* knockouts by reflecting the biological dependencies from the signal initiation to the cell response. Furthermore, we developed a tool named isiKnock to facilitate the automatized prediction of *in silico* knockout behavior.

4.3.1 The concept of *in silico* knockouts

The concept of *in silico* knockouts developed in this thesis rests on the method described by Grunwald *et al.* [59], which is based on T-invariants. Transitions of a PN can be *knocked out*, i.e., are not functional or impaired. A T-invariant, $ti \in TI$, is called *affected* by the knockout, if the knocked out transition t is part of the T-invariant, i.e., $t \in ti$, and *unaffected*, otherwise.

The *impact* of a transition on the network can be measured by the number or percentage of affected T-invariants.

For a knocked out transition t, the set of affected T-invariants TI_{affected} is given by

$$TI_{\text{affected}}(t) = \{ti \in TI | t \in ti\},$$

with ti is a T-invariant and TI is the set of all T-invariants of the PN. Accordingly, the set of unaffected T-invariants $TI_{\text{unaffected}}$ is defined by

$$TI_{\text{unaffected}}(t) = \{ti \in TI | t \notin ti\}.$$

For the knockout of several transitions $t_j, ..., t_k$, the sets of affected and unaffected T-invariants are given by

$$TI_{\text{affected}}(t_j, ..., t_k) = TI_{\text{affected}}(t_j) \cup ... \cup TI_{\text{affected}}(t_k) \text{ and}$$

$$TI_{\text{unaffected}}(t_j, ..., t_k) = TI_{\text{unaffected}}(t_j) \cap ... \cap TI_{\text{unaffected}}(t_k),$$

respectively.

In experimental perturbation studies, commonly the synthesis of a protein is impaired to investigate which pathway components are affected. Accordingly, guided from the biological question, it is important to know the influence of a knocked out transition, e.g., a protein synthesis reaction, on the places of the PN.

We define a place p as *unaffected* by the knockout of a transition t if

$$\exists t' \in \bullet p | \exists ti \in TI_{\text{unaffected}}(t) \wedge t' \in ti,$$

where $\bullet p$ is the set a pre-transitions of the place p. In contrast, a place p is *affected* by the knockout of a transition t if

$$\nexists t' \in \bullet p | \exists ti \in TI_{\text{unaffected}}(t) \wedge t' \in ti.$$

In other words, if there exists a pre-transition of a place that is part of an unaffected T-invariant, the place is called unaffected and otherwise a place is called affected.

From the biological perspective, a pathway component represented by a place in the PN is affected by the knockout if their is no way to produce the component under steady-state conditions. Otherwise, if there is still at least one way to produce the pathway component at steady state, the component is unaffected by the knockout.

We visualize the pairwise influences of each knocked out transition to each place by a matrix representation named *in silico knockout matrix*. The entries of the *in silico* knockout matrix for a PN with the transitions $t_1, ..., t_j, ..., t_n$ and the places $p_1, ..., p_i, ..., p_m$ is given by

$$z_{i,j} = \begin{cases} 0, & \text{if } \exists t \in {}^\bullet p | \exists ti \in TI_{\text{unaffected}}(t_j) \wedge t \in ti \\ 1, & \text{if } \nexists t \in {}^\bullet p | \exists ti \in TI_{\text{unaffected}}(t_j) \wedge t \in ti. \end{cases} \tag{4.1}$$

The value 0 of the entry $z_{i,j}$ indicates that place p_i is unaffected by the knockout of transition t_j, and 1 stands for an affected place. Each of the n matrix rows stands for a knocked out transition, whereas each of the m matrix columns represents a place. The binary values of the matrix entries are visualized by either a red or a green circle. The value 0 is color-coded by a green circle, representing an unaffected place, and the value 1 by a red circle, representing an affected place. In other words, a green entry indicates that the turnover of the pathway component j is functional under steady-state conditions if reaction i is knocked out. For a red entry, the turnover of the pathway component j is not functional at steady state. Under the term *turnover* we understand the balance between the synthesis or production and degradation of a pathway component [194].

In the following, we want to consider the concept of *in silico* knockout on a small PN example, see Figure 4.18A. The example PN models the synthesis of two proteins, A and B, the binding of these proteins to form a complex, AB, and the outflow of the complex to the environment. The PN is composed of one T-invariant, $ti_1 = \{SynA, SynB, Bin, Out\}$, which contains all the transitions of the PN, i.e., the PN fulfills the CTI property. The knockout of any transition affects the T-invariant ti_1. Thus, the impact of each transition on the network is 100%.

The *in silico* knockout matrix of the PN in Figure 4.18A is depicted

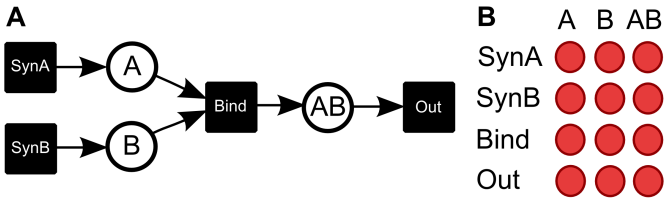

Figure 4.18 A small PN example and its *in silico* knockout matrix. (A) The PN consists of three places, protein A, protein B, and protein complex AB, and four transitions, *SynA*, *SynB*, *Bin*, and *Out*. The PN fulfills the CTI property and consists of one T-invariant, $ti_1 = \{SynA, SynB, Bin, Out\}$. (B) The *in silico* knockout matrix of the PN shown in part A. All matrix entries are visualized by red circles, representing affected places.

in Figure 4.18B. The four rows of the matrix represent the knocked out transitions of the PN, *SynA*, *SynB*, *Bin*, and *Out*. The three columns stand for the places of the PN, A, B, and AB. From the biological perspective, each column of the matrix represents a pathway component. Each row represents an impairment of a reaction, depending on the biological interpretation of the transition that is knocked out.

Input transitions produce tokens, and therefore they often represent the synthesis or the production of pathway components. The knockout of an input transition is related to an experimental gene knockout or knockdown. In the example PN, the knockout of the input transition *SynA* or *SynB* blocks the synthesis of protein A or protein B, respectively. Inner transitions often represent specific biochemical reactions, such us binding processes or phosphorylations. The knockout of an inner transition can symbolize the disruption of an individual protein interaction domain or phosphorylation site without disrupting the entire protein. In the example PN, the knockout of the inner transition *Bind* could stand for a deletion of the interaction domain, which enables the binding of protein A to protein B. The knockout of output transitions, which consume pathway components, can experimentally represent the blockage of underlying pathways. For example, if the response of a signaling pathway is modeled by an output transition, representing, e.g., cell death or autophagy, the knockout of this transition represents the deletion of proteins that are essential for these underlying pathways. In the example PN, the knockout of the output transition *Out* hampers the outflow of the complex to the environment and can stand for perturbing an

underlying pathway that is dependent on the protein complex AB.

For the example PN in Figure 4.18A, all entries of the *in silico* knockout matrix are red (see Figure 4.18B), i.e., all pathway components are affected by each knockout, and their turnover is not functional. For example, the knockout of transition *SynA*, indicating that the synthesis of protein A is impaired, has an effect on protein B. If protein A is knocked out, protein A can not bind to protein B, which leads to an accumulation of protein B, and the turnover of protein B becomes not functional. However, an experimental knockout or knockdown of protein A would have no effect on protein B. If the synthesis of protein A is not functional, protein B would be unaffected, and the turnover takes place. The accumulation of protein B would enhance its consumption, what in the long run recovers the turnover of protein B.

In general, PN models of signaling pathways do not include for each pathway component a degradation reaction, i.e., for each place an output transition. The degradation reactions can be ignored under basic conditions, because we are interested in the signal flows that lead to the respective cell response. Under knockout conditions, these degradation reactions become more important. To achieve comparable results with experimental knockout or knockdown experiments, we extended the concept of *in silico* knockouts by considering these degradation reactions to ensure the turnover of pathway components under knockout conditions. For each place that is listed in the knockout matrix, we add an additional output transition. Figure 4.19A shows the modified PN. Three output transitions for the places A, B, and AB are appended. These output transitions, *DegA*, *DegB*, and *DegAB*, can be interpreted as degradation processes of protein A, protein B, and protein complex AB, respectively. The modified PN has four T-invariants

$ti_1 = \{SynA,\ SynB,\ Bin,\ Out\}$,
$ti_2 = \{SynA,\ DegA\}$,
$ti_3 = \{SynB,\ DegB\}$, and
$ti_4 = \{SynA,\ SynB,\ Bin,\ DegAB\}$.

One of the T-invariants, ti_1, is also a T-invariant of the original PN in Figure 4.18A and three new T-invariants, ti_2-ti_4, exist. ti_2 and ti_3 represents the turnover of the proteins A and B, respectively. ti_4 describes the

turnover of the protein complex AB, including the synthesis of the complex compounds, proteins A and B, the complex formation, and its degradation.

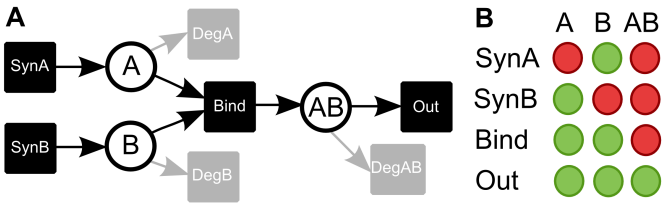

Figure 4.19 The small PN example with additional output transitions and its *in silico* knockout matrix. (A) The PN depicted in Figure 4.18A with additional output transitions, *DegA*, *DegB*, and *DegAB*. (B) The *in silico* knockout matrix of the PN shown in part A.

The *in silico* knockout matrix for the PN with additional output transitions in Figure 4.19A is shown in Figure 4.19B. Now, seven entries of the knockout matrix switch from red to green. For example, the knockout of transition *SynA* has no influence on protein B, which is in accordance with an experimental knockout or knockdown of protein A. If the synthesis of protein A is knocked out, the turnover of protein B can still be functional at steady state. The additional output transition ensures the turnover at steady state, only if the place is unaffected by the knockout and reveals *in silico* knockouts that are comparable with experimental gene knockouts or knockdowns.

For the *in silico* knockout analysis, the PN should fulfill the CTI property, but formally the presented method can also be applied to PN that are not CTI. Parts of the PN that are not part of any T-invariant-induced subnet will always be interpreted as affected by the knockout.

A PN of a biological pathway is in general not a directed chain of reactions that transmit the signal from the initiation to the response. Many regulatory mechanisms, such as feedback loops, exist that influence upstream signaling processes and make signaling pathways highly interconnected [41, 195]. These regulatory mechanisms cause cycles in the network structure. This results in the decomposition of the pathways into functional modules at steady state expressed by T-invariants. Cycles in the PN topology are often expressed by P-invariants of the subnets induced by T-invariants. Consequently, the T-invariant analysis can not necessarily

reveal entire signal flows in signaling pathways and therefore T-invariants not always reflect the biological dependencies. For an example, see the T-invariants of the PN of the xenophagic capturing of *Salmonella* illustrated in Figure 4.8 in Subsection *Transition invariants of the Petri net*. The similar concept of EFM has been previously described as inapt to reflect causal dependencies of pathways [108].

For this reason, the *in silico* knockout analysis based on T-invariants can lead to results that are in contradiction to the expected knockout behavior from experimental perturbation studies. To get biologically comparable results for networks with cyclic structures, a linear combination of T-invariants, the *Manatee invariants*, can be applied for the computation of *in silico* knockouts.

4.3.2 The concept of Manatee invariants

We developed the concept of Manatee invariants to uncover entire signal flows in pathways from the signal initiation to the cell response [148]. The method is based on the concept of feasible T-invariants presented by Sackmann *et al.* [54]. In the following, we give a short explanation of Manatee invariants and discuss the benefit to perform *in silico* knockouts based on Manatee invariants. For a more detailed and formal definition, we refer to Amstein *et al.* [148].

Equivalent to the Definition 2.3 of a subnet induced by a T-invariant in Chapter *Theoretical Background*, the subnet induced by a Manatee invariant, mi, is PN_{mi}. A linear combination of T-invariants is called a Manatee invariant, mi, if its induced subnet PN_{mi} contains no P-invariants, except those are P-invariants of the whole PN.

A small example of a Manatee invariant is given by the PN depicted in Figure 4.20. The PN models an enzyme-catalyzed reaction, inspired by the Michaelis-Menten reaction kinetics [136]. The PN has four places and six transitions. The places S, E, ES, and P represent a substrate S, an enzyme E, the complex ES of the enzyme and the substrate, and a product P, respectively. The PN fulfills the CTI-property and consists of two T-invariants, $ti_1 = \{SynS, Bind, Diss, DegP\}$ and $ti_2 = \{SynE, DegE\}$. ti_1 represents

the generation of substrate S, its binding to enzyme E, its catalyzation by E into product P, and the degradation of P. ti_2 describes the turnover of enzyme E.

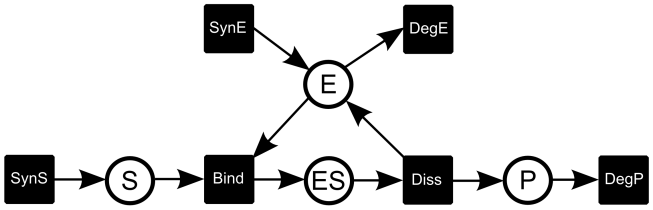

Figure 4.20 A PN of an enzyme-catalyzed reaction. The PN consists of two T-invariants, $ti_1 = \{SynS, Bind, Diss, DegP\}$ and $ti_2 = \{SynE, DegE\}$, and two Manatees invariants, $mi_1 = ti_1 + ti_2 = \{SynS, Bind, Diss, DegP, SynE, DegE\}$ and $mi_2 = ti_2 = \{SynE, DegE\}$.

The PN in Figure 4.20 has no P-invariants. The ti_1-induced subnet, PN_{ti_1}, contains one P-invariant, $pi_1 = \{E, ES\}$. pi_1 covers the cyclic structure of the PN and represents the conservation of enzyme E. This cyclic structure causes the decomposition of the PN into the two T-invariants, ti_1 and ti_2. The two T-invariants uncouple the process of the enzyme-catalyzed reaction into two functional modules that can operate at steady state. From the biological perspective, the catalyzation of the substrate S is functionally dependent on the synthesis of the enzyme E. Therefore, the functionality of ti_1 is dependent on transition $SynE$, which is part of ti_2.

This small PN example points out the property of T-invariants to describe functional modules at steady state and their deficiency to reflect the biological dependencies. The concept of Manatee invariants combines T-invariants to recover the functional dependencies at steady state.

T-invariant ti_1 does not fulfill the property of a Manatee invariant because of P-invariant pi_1 of PN_{ti_1}. The linear combination of ti_1 and ti_2 induces a PN, $PN_{ti_1+ti_2}$, that fulfills the property of a Manatee invariant by the lack of P-invariants and forms the Manatee invariant

$$mi_1 = ti_1 + ti_2 = \{SynS, Bind, Diss, DegP, SynE, DegE\}.$$

The subnet induced by ti_2, PN_{ti_2}, contains no P-invariants and for this

reason, ti_2 is per definition also a Manatee invariant,

$$mi_2 = ti_2 = \{SynE, DegE\}.$$

The algorithm for the contruction of Manatee invariants can be found in Amstein *et al.* [148].

In silico knockout based on Manatee invariants

The advantage of performing *in silico* knockouts based on Manatee invariants in contrast to T-invariants can be illustrated by the small PN depicted in Figure 4.20. For the *in silico* knockout analysis, additional output transitions, *OutS*, *OutE*, *OutES*, and *OutP*, are added to the places included in the knockout matrix, see Figure 4.21A.

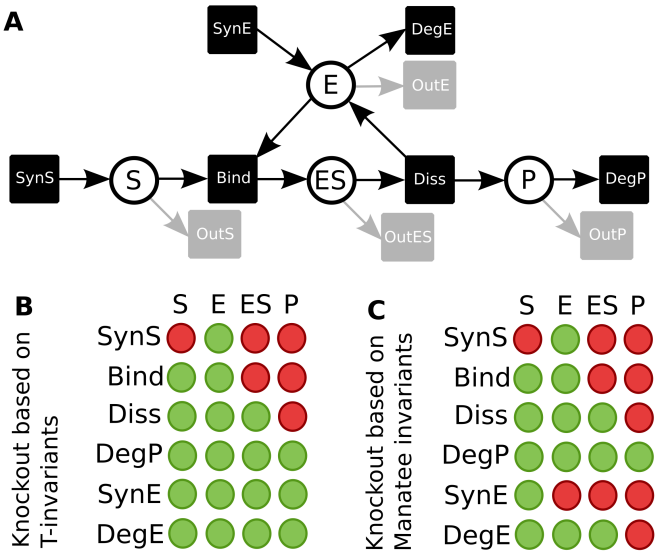

Figure 4.21 The Petri net of an enzyme-catalyzed reaction and its *in silico* knockout matrices. (A) The PN depicted in Figure 4.20 with additional output transitions, *OutS*, *OutE*, *OutES*, and *OutP*. (B) The *in silico* knockout matrix based on T-invariants of the PN in part A. (C) The *in silico* knockout matrix based on Manatee invariants of the PN in part A.

The T-invariants of the PN depicted in Figure 4.21A are

$ti_1 = \{Bind,\ Diss,\ SynS,\ DegP\}$,
$ti_2 = \{SynE,\ DegE\}$,
$ti_3 = \{SynS,\ OutS\}$,

$ti_4 = \{SynE,\ OutE\}$,
$ti_5 = \{Bind,\ Diss,\ SynS,\ OutP\}$, and
$ti_6 = \{Bind,\ SynS,\ SynE,\ OutES\}$.

The T-invariants ti_1 and ti_2 are equivalent to the T-invariants ti_1 and ti_2 of the original PN without output transitions, see Figure 4.20. The additional output transitions generate four further T-invariants, ti_3-ti_6.

We knocked out all transitions of the PN, *SynS*, *Bind*, *Diss*, *DegP*, *SynE*, and *DegE*. Figure 4.21B shows the resulting knockout matrix based on the T-invariants. For example, the knockout of transition *SynS* affects the places *S*, *ES*, and *P*. Place *E* is unaffected by this knockout. The knockout behavior is in accordance with the expected biological knockout effects. The experimental knockout of the production of a substrate S would affect the substrate S itself, the enyzme-substrate complex ES can not be formed, and product P can not be produced. In contrast, the knockout of transition *SynE* is in contradiction with the expected experimental knockout behavior, by not affecting any place of the PN. One would expect that the experimental knockout of the synthesis of enzyme E affects the enzyme E itself, the enzyme-substrate complex ES can not be formed, and product P can not be produced. This misleading result is caused by the deficiency of T-invariants to reflect all biological dependencies.

The Manatee invariants of the PN shown in Figure 4.21A are

$mi_1 = \quad ti_2 \quad = \{SynE,\ DegE\}$,
$mi_2 = \quad ti_3 \quad = \{SynS,\ OutS\}$,
$mi_3 = \quad ti_4 \quad = \{SynE,\ OutE\}$,
$mi_4 = \quad ti_6 \quad = \{Bind,\ SynS,\ SynE,\ OutES\}$,
$mi_5 = ti_1 + ti_2 = \{Bind,\ Diss,\ SynS,\ DegP,\ SynE,\ DegE\}$,
$mi_6 = ti_1 + ti_4 = \{Bind,\ Diss,\ SynS,\ DegP,\ SynE,\ OutE\}$,
$mi_7 = ti_1 + ti_6 = \{2{*}Bind,\ Diss,\ DegP,\ 2{*}SynS,\ SynE,\ OutES\}$,
$mi_8 = ti_5 + ti_2 = \{Bind,\ Diss,\ SynS,\ SynE,\ DegE,\ OutP\}$,
$mi_9 = ti_5 + ti_4 = \{Bind,\ Diss,\ SynS,\ SynE,\ OutE,\ OutP\}$, and
$mi_{10} = ti_5 + ti_6 = \{2{*}Bind,\ Diss,\ 2{*}SynS,\ SynE,\ OutES,\ OutP\}$.

The T-invariants ti_2, ti_3, ti_4, and ti_6 are also Manatee invariants, mi_1-mi_4, because the induced subnets of these T-invariants contain no P-invari-

ants. In contrast, both ti_1 and ti_5 comprise the P-invariant $pi_1 = \{E, ES\}$ and thereby do not fulfill the property of a Manatee invariant. The linear combination of either ti_1 or ti_5 with ti_2, ti_4, or ti_6 abolish pi_1 by coupling the synthesis of the enzyme E, transition *SynE*, with the catalyzation of the substrate S. The resulting T-invariant-induced subnets $PN_{ti_1+ti_2}$, $PN_{ti_1+ti_4}$, $PN_{ti_1+ti_6}$, $PN_{ti_5+ti_2}$, $PN_{ti_5+ti_4}$, and $PN_{ti_5+ti_6}$ exhibit no P-invariants. In each case, they fulfill the property of a Manatee invariant and form the Manatee invariants mi_5-mi_{10}.

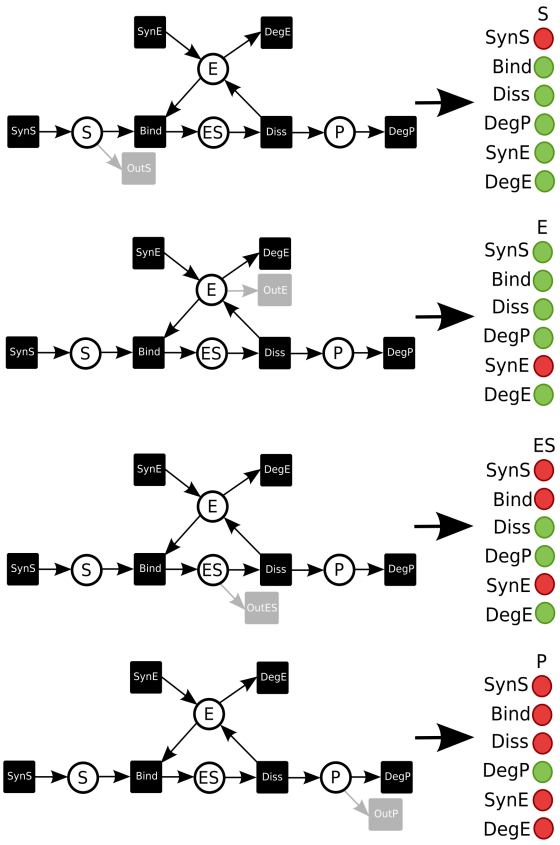

Figure 4.22 Column-wise computation of the knockout matrix. Four PN are generated from the PN shown in Figure 4.20. Each PN contains an additional output transition, *OutS*, *OutE*, *OutES*, or *OutP*. For each PN, a matrix is computed and then combined to the knockout matrix in Figure 4.21C.

Figure 4.21C illustrates the resulting knockout matrix based on the Manatee invariants. In comparison to the knockout of transition *SynE* based on T-invariants, see Figure 4.21B, the knockout of *SynE* based on Manatee invariants does not affect place *S* but affects places *ES*, *E*, and *P*. From the

biological perspective, we would expect that the knockout of the synthesis of an enzyme E affects the enzyme E itself, the formation of the enzyme-substrate complex ES, and the production of the product P. In contrast to the knockout based on T-invariants, the knockout based on Manatee invariants correctly reveals the expected biological knockout behavior.

For some PN topologies, the additional output transitions may lead to invariants with more than one output transition included. To prevent such side-effects caused by multiple output transitions, the computation of the knockout matrix is performed column by column, see Figure 4.22. For each of the four places, a PN that contains one additional output transition is generated. Now, a knockout matrix with one column is computed for each of the four PN. The resulting four matrices can be combined to the knockout matrix in Figure 4.21C.

In silico knockout of Petri net models with P-invariants

The influence of P-invariants on the knockout behavior is illustrated by the small PN depicted in Figure 4.23A. The PN describes the same process of an enzyme-catalyzed reaction as depicted in Figure 4.20, except the transitions *SynE* and *DegE*. Here, it is assumed that the enzyme E is always present in the cell and need not to be produced or consumed. For the simulation of the PN, at least one token has to be assigned to the places *E* or *ES*. The lack of *SynE* and *DegE* cause a P-invariant, pi_1, containing the places *E* and *ES*. The PN exhibits one T-invariant and an equivalent Manatee invariant, $mi_1 = ti_1 = \{SynS, Bind, Diss, DegP\}$.

For the computation of *in silico* knockouts, an additional output transitions is added to each place, see Figure 4.23B. The additional output transitions generate two further T-invariants, $ti_2 = \{SynS, OutS\}$ and $ti_3 = \{Bind, Diss, SynS, OutP\}$. The additional output transitions *OutE* and *OutES* of the places *E* and *ES*, which are contained in pi_1, are both not part of any T-invariant. Therefore, the PN does not fulfill the CTI property.

Resulting from the constant marking of the places that are part of a P-invariant, the pathway components that represent the P-invariant are not

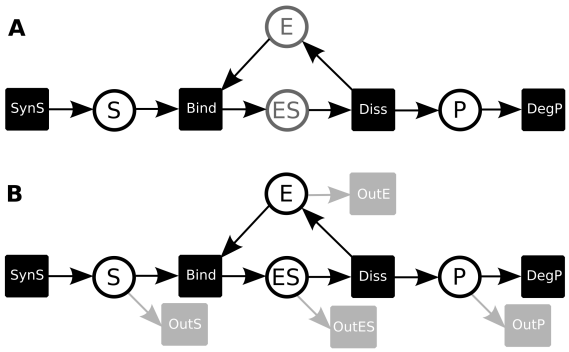

Figure 4.23 The PN of an enzyme-catalyzed reaction with a P-invariant. (A) The PN consists of one T-invariant, $ti_1 = \{SynS, Bind, Diss, DegP\}$, one Manatee invariant, $mi_1 = ti_1$, and one P-invariant, $pi_1 = \{E, ES\}$ (gray-colored). (B) The PN from A with additional output transitions, *OutS*, *OutE*, *OutES*, and *OutP*.

produced or degraded. In other words, places of a P-invariant have no input or output transitions, which produce or degrade tokens, respectively. The addition of output transitions on places that are part of a P-invariant leads to a consumption of the tokens on these places, thus the marking of these places is not constant anymore and as a consequence the P-invariant dissolves. Furthermore, the additional output transition, which consumes the pathway component, is not part of any T-invariant, because the pathway component is never produced in the network.

The PN in Figure 4.23B exhibits one Manatee invariant $mi_1 = ti_2 = \{SynS, OutS\}$. ti_1 and ti_3 are no Manatee invariants, because their induced subnets, PN_{ti_1} and PN_{ti_3}, each contains the P-invariant $pi_{1'} = \{E, ES\}$ that is no P-invariant of the PN. A linear combination of the T-invariants can not resolve $pi_{1'}$ and hence does not result in further Manatee invariants.

Thus, additional output transitions for places that are part of a P-invariant induce a PN that does not fulfill the CTI property. Due to the fact that the *in silico* knockout analysis operates on T-invariants or Manatee invariants, additional output transitions on places that are part of a P-invariant can produce misleading results. Figure 4.24A shows the PN with additional output transitions only for the places that are not part of any P-invariant, *OutS* and *OutP*. The places E and ES of pi_1 have not received additional output transitions. The omission of additional output transitions for places that are part of a P-invariant is equivalent to the de-

termination of Manatee invariants only for the parts of the PN that fulfills the CTI property.

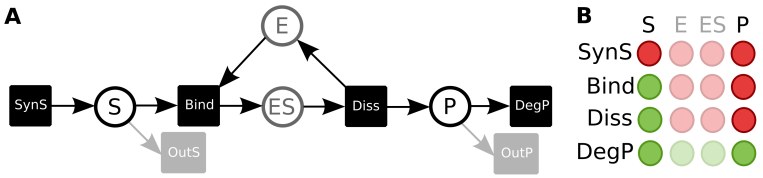

Figure 4.24 The Petri net of an enzyme-catalyzed reaction with a P-invariant and its *in silico* knockout matrix. (A) The PN in Figure 4.20 with additional output transitions, *OutS* and *OutP*. The PN contains three T-invariants, three Manatee invariants, and one P-invariant (gray-colored). (B) The *in silico* knockout matrix based on T-invariants or Manatee invariants of the PN from part A. The columns of the places *E* and *ES*, which are part of the P-invariant, are grayed out.

The PN contains three T-invariants and the equivalent Manatee invariants,

$ti_1 = mi_1 = \{\text{Bind, Diss, SynS, DegP}\},$
$ti_2 = mi_2 = \{\text{SynS, OutS}\}$, and
$ti_3 = mi_3 = \{\text{Bind, Diss, SynS, OutP}\}.$

The corresponding knockout matrix, which is the same for T-invariants and Manatee invariants, is depicted in Figure 4.24B. The places *E* and *ES* differ from the knockout behavior shown in Figure 4.21C, which is based on the PN without P-invariants and includes the transitions *SynE* and *DegE*. For example, the knockout of transition *Diss* affects the places *E* and *ES*. For the PN that does not model the synthesis of the enzyme E, this knockout behavior is correct, enzyme E can only be produced by the dissociation of the enzyme-substrate complex ES and in consequence, if enzyme E is affected, the enzyme-substrate complex ES is affected too. But under experimental conditions, such a knockout behavior can not be observed. The knockout of the dissociation of the enzyme-substrate complex ES would only affect product P and not E or the complex ES, because in the cell, the enzyme can still be produced and bind to substrate S. For this reason, we recommend to build PN models that are free of P-invariants or to exclude places of a P-invariant from the knockout analysis, because they can cause knockout predictions that contradict the expected experimental knockout behavior.

4.3.3 The software isiKnock

To automate *in silico* knockout analyses, we developed a software called isiKnock. The software is open source and is available on sourceforge `https://sourceforge.net/projects/molbi-isiknock/`. The software concept and design as well as the software verification and preparation of the tutorial was my contribution to this work. Heiko Giese performed the implementation of isiKnock, based on a prototype, which was developed in the Bachelor thesis of Börje Schweizer [196]. The algorithms used for the determination of T-invariants and Manatee invariants was implemented by Jörg Ackermann and has been presented in Koch and Ackermann [131] and Amstein *et al.* [148], respectively.

The general flowchart depicted in Figure 4.25 illustrates the workflow of the software. In the following, we outline the functionalities of isiKnock. For a comprehensive explanation of the functionalities based on a example PN, we refer to the tutorial on `http://www.bioinformatik.uni-frankfurt.de/tools/isiKnock/index.php`.

At first, the user can load a PN in the file formats systems biology markup language (SBML, Level 3 Version 1) [197] or PNT from the software Integrated Net Analyzer (INA) [198]. A PN editor that allows the export of PNT or SBML files is, e.g., MonaLisa [84]. When loading the file, the P-invariants and the parts of the PN that fulfill the CTI property are computed. The *in silico* knockout analysis can also be applied to PN that are not CTI. Places and transitions of parts of the PN that are not CTI can not be included in the analysis.

Once the PN is loaded, the properties of the PN, such as the name of the file, number of transitions (named reactions), and places (named species) are displayed. When the knockout panel is enabled, the user can change the settings, and select the transitions and places for the *in silico* knockouts via the GUI, see Figure 4.26.

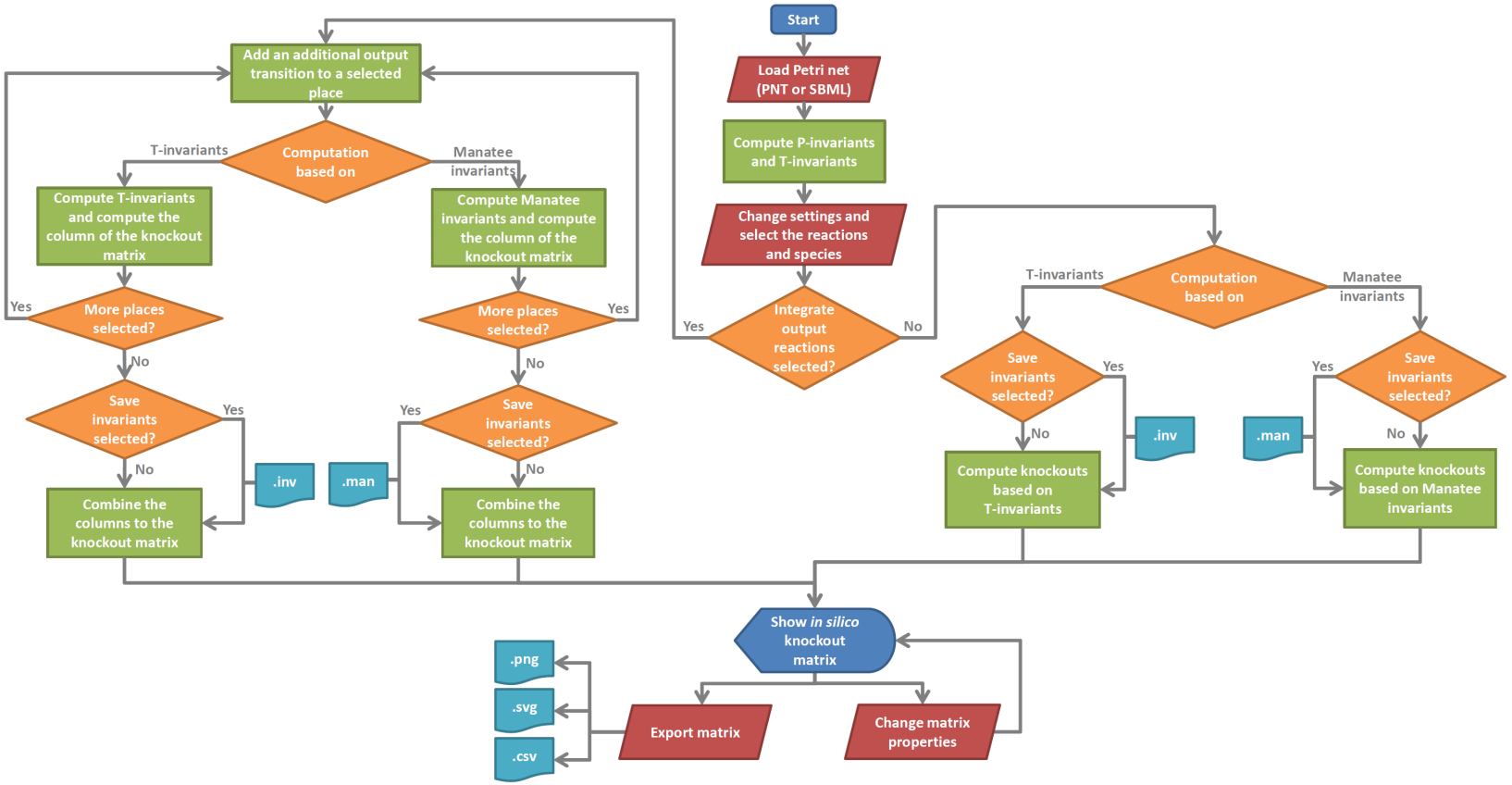

Figure 4.25 Flowchart of the software isiKnock. The flowchart illustrates the workflow of the software from starting the tool to the generation of the *in silico* knockout matrix and its export.

We provide two algorithms for the computation of Manatee invariants, *Manatee invariants (fast search)* and *Manatee invariants (exhaustive search)*. By default, the *Manatee invariants (fast search)* is selected. This efficient algorithm provides much faster knockout results, but may not find all Manatee invariants. Therefore, the predicted knockout behavior may not reflect all biological dependencies. However, for our tested PN of the xenophagic capturing of *Salmonella* in epithelial cells, the results of the fast search and the exhaustive search were the same. By selecting *Manatee invariants (exhaustive search)*, a brute force algorithm searches all possible Manatee invariants by covering the whole search space. The user has the option to perform the analysis based on Manatee invariants or on T-invariants. The T-invariants and Manatee invariants can be saved in text files with the file extensions ".inv" and ".man", respectively. For networks that contain cyclic structures, we recommend to perform the computation based on Manatee invariants. However, it should be noted that the computation of *in silico* knockouts based on Manatee invariants is computationally hard for PN exhibiting a huge number of T-invariants. As the determination of T-invariants requires exponential space [132, 133], the computation of Manatee invariants, in the worst case, takes at least exponential space.

The default setting selects all transitions and places of the PN. However, the places that are part of a P-invariant, transitions that are not part of any T-invariant, and places that have only pre-transitions, which are not included in a T-invariant, are deactivated and can not be selected. The user has the option to re-enable the places that are part of a P-invariant. Besides these deactivated transitions and places, the remaining transitions and places can be individually selected or deselected by the user. There is the option to select all transitions or all places of the PN at once or to select all the input transitions of the PN, which often represent protein syntheses. All selected transitions will be knocked out and are included, together all the selected places, in the *in silico* knockout matrix. In the default settings, the software adds additional output transitions to the selected places.

After all settings are defined and the transitions and places that should be displayed in the matrix are selected, the computation of the knockout analysis can be started. An additional output transition is added to one of

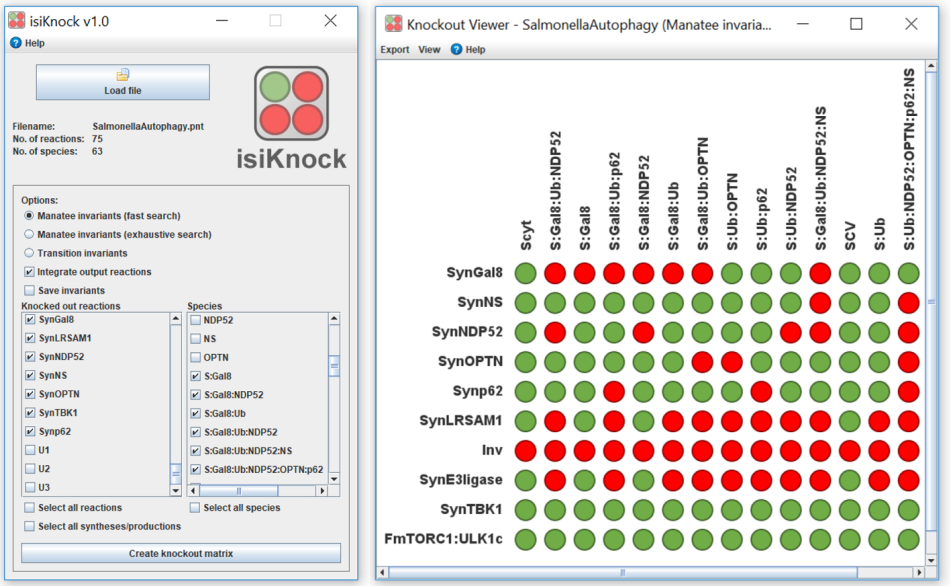

Figure 4.26 The GUI of the software isiKnock. The left part shows the start window of isiKnock. The right part depicts the *in silico* knockout matrix for the PN of the xenophagic capturing of *Salmonella* in epithelial cells, illustrated in Figure 4.2.

the selected places. Then, the invariants of the modified PN are computed and the knockout matrix column for the selected place is generated. For each of the selected places, a PN is created, invariants are computed, and a matrix column is generated. At the end of the column-wise computation, all columns are combined to form the knockout matrix. There is also an option to compute the knockout matrix without additional output transitions. When the computation terminates, a new window opens showing the *in silico* knockout matrix.

The layout of the matrix can be adjusted by the user; the names of places and transitions can be edited, the colors can be adapted, and the order of the matrix entries can be changed. By default, a matrix entry is green, if the place is unaffected by the knockout and red if the place is affected. Moreover, the matrix entries can be clustered to detect groups of transitions that effect the system or places that are influenced by the system in a similar manner. Furthermore, a multiple knockout can be included by an additional row in the matrix, representing the combined knockout of all transitions in the matrix. The performance of multiple perturbations in experimental systems biology has been reviewed by Jansen to obtain the greatest knowledge with

the lowest costs [206]. The user can export the matrix as comma-separated values (CSV) file with the extension ".csv" or as a picture in the graphics file format portable network graphics (PNG) with the extension ".png" or scalable vector graphics (SVG) with the the extension ".svg".

Chapter 5

Conclusion and Outlook

This chapter summarizes the main findings of this thesis, which are

1. the PN model of the xenophagic capturing of *Salmonella enterica* serovar Typhimurium in epithelial cells and predictions of the knockout behavior,

2. the SPN of an infected epithelial cell with *Salmonella enterica* serovar Typhimurium and predictions of the quantitative dynamics of *Salmonella* infections,

3. the novel model analysis techniques of *in silico* knockouts and Manatee invariants, and

4. the software isiKnock to automatically perform *in silico* knockouts.

In the following, the achievements as well as the limitations of these studies are stated and suggestions for further research are described.

The first contribution was the PN of the xenophagic capturing of *Salmonella*, which was manually compiled by collecting information from literature sources into a consensus model, representing the first realization of a computational model of this pathway. During the process of model development, we found a missing part in the knowledge about the source of TBK1 activation upon Salmonella infection. We suggested a new mechanism of autoactivation of TBK1 around *Salmonella* by oligomerization triggered by high local concentration of TBK1 dimers. Future work will reveal whether the

autoactivation of TBK1, controlled by its intracellular localization around the bacterium, results in an enhanced xenophagic degradation of *Salmonella*.

We demonstrated the consistency and the correctness of the PN model, by the analyses of T-invariants, P-invariants, Manatee invariants, and *in silico* knockouts. We found experimental perturbation data for 52 of 450 predictions. These data match in all of the cases with the *in silico* knockout predictions. The PN reflects the current knowledge of the xenophagic capturing of *Salmonella*, which is partly based on these perturbation studies and hence is in accordance with existing experimental data. Nevertheless, potential inconsistencies and errors in either the network topology or the knowledge of the pathway would have revealed by the knockout analysis. The complete accordance of the *in silico* knockout predictions with the experimental perturbations verifies the correctness and the biological credibility of the PN model and provides a proof of principle for the new concept of *in silico* knockouts. Also, the complete accordance demonstrates the accuracy of the reference papers by not presenting conflicting experimental perturbation effects and underlines the correctness of the state-of-the-art knowledge of the pathway. Additionally, the 344 knockout predictions, for which no experimental perturbation have been published and which are not biologically obvious, can be validated in future experiments. Thus, the results from the *in silico* knockout analysis provided a basis for future investigations of the pathway.

The field of xenophagy is subject of ongoing research. Therefore, the presented model depicts not a complete representation of this biological system. Many interactions are still unknown and thereby not part of the model. Some interactions have been proven in multiple experiments and reported in diverse references, others have only been presented in a single paper. Additionally, the experiments are performed under different conditions. We included those interactions that have been proven in mammalian epithelial cell lines, mainly HeLa cells. The pathway of xenophagic capturing of *Salmonella in vivo*, e.g., in the intestinal epithelium, may differ from the interactions found in the HeLa cell model [193]. However, since *in vivo* data are not available so far, the variety of experiments of HeLa cells infected with *Salmonella* Typhimurium allows to gather valuable insights into

mechanisms involved in bacterial infections.

The presented PN provides a holistic, mathematical representation of the xenophagic recognition of *Salmonella* inside epithelial cells. In future work, new and undiscovered interactions can be extended to the PN. For example, in our model, we assumed the existence of further E3 ubiquitin ligases, in addition to LRSAM1. Recently, two further E3 ubiquitin ligases, ARIH1 [179] and HOIP [180], have been identified to play a role in the ubiquitination of *Salmonella*. Other interesting points to extend the PN in the future will be, e.g., the detection of further eat-me signals, in addition to galectin-8 and ubiquitin, and the identification of further autophagy receptors, in addition to p62, NDP52, and OPTN. Furthermore, the PN can be expanded by modeling the processes of phagophore formation or by the inclusion of other pathways that interconnect with the proteins involved in the xenophagic capturing of *Salmonella*, like the nuclear factor-κB (NF-κB) signaling pathway, which is connected with TBK1 [199, 200]. In this context, it has recently been reported that the ubiquitin coat around cytosolic *Salmonella* serves as a platform, which triggers NF-κB signaling [180, 181]. If quantitative data in form of kinetic parameters and concentrations become available, the PN or parts of the PN can be extended to model the quantitative system's behavior.

The second contribution was the SPN of an infected epithelial cell with *Salmonella*, which was manually compiled and parameterized by a set of experimental data derived from different literature sources. The SPN predicts the time evolution of an epithelial cell infected with *Salmonella* at different stages of the infection and thereby captures the stochastic variation and heterogeneity of the cytosolic and vacuolar *Salmonella* population. The simulations indicate that intracellular, vacuolar bacteria in the first period of the infection become outnumbered by fast-replicating, cytosolic bacteria at later time points of the infection. In the SPN, it is assumed that the late onset of bacterial proliferation inside the cytosol is caused by xenophagic degradation and not by a long lag phase of cytosolic *Salmonella*. This suggestion is encouraged, by the detection of bacterial growth of cytosolic bacteria as early as 4 h p.i. in NDP52-depleted cells [31]. In some of the simulated cells, xenophagy succeed by recognizing all cytosolic *Salmonella* and in other cells,

xenophagy was predicted to fail. The simulation of the SPN indicates that at late time points of the infection, i.e., 16 h p.i., *Salmonella* inside the SCV can also result in more than 50-100 bacteria per cell. Per definition, these cells would be termed as hyper-replicative [14,17], which would imply the presence of cytosolic *Salmonella* in these cells. We demonstrated that the term *hyper-replication* defined by the number of intracellular bacteria to describe cells with cytosolic *Salmonella* is valid at 8 h p.i., but not at 2 h p.i. and 16 h p.i. Furthermore, the SPN can be applied to improve experimental design, e.g., we predicted the infection efficiency of epithelial cells with *Salmonella*, depending on the factors incubation time and MOI.

The parameterization of the SPN is based on experiments with the commonly used human epithelial cell line of HeLa cells. The question arises whether *in vitro* studies using this cell line as a model system can elucidate the processes that occur under *in vivo* conditions. Some of the processes have been observed to occur in polarized epithelial cells and *in vivo* in a similar way. For example, the cooperative invasion has also been detected in polarized epithelial cells [183] and in the intestinal epithelium of guinea pigs [201]. The clustering of multiple bacteria on a single ruffle has been observed in cultured IEC [187]. The behavior of swimming close to the cell surface, has been shown by *in vivo* live microscopy in the cecum of infected mice [202]. A further study in polarized human IEC presented that *Salmonella* in the cytosol proliferate with higher rates than in the SCV [14]. The extrusion of these cells from the monolayer is associated with pyroptosis, an inflammatory form of programmed cell death, and results in dissemination of bacteria into neighboring cells. *In vivo* imaging of IEC is still an experimental challenge. When *in vivo* data from *Salmonella*-infected cells become available, the adaption of the model parameters will be an interesting objective for future research. Likewise, the adaption of the SPN to model the infection by other pathogens, such as *Shigella flexneri* [203], which shows a similar behavior as *Salmonella* inside epithelial cells, will be an important issue for future studies.

The SPN is in agreement with real experimental outcomes and allows for the examination and prediction of the dynamics of *Salmonella* infections in epithelial cells. First estimations for the kinetic parameters of a

Salmonella infection were provided. In future work, in an iterative way of model predictions and experimental validation, the parameters can be further adjusted. The optimal choice would be quantitative single cell experiments in combination with live-cell imaging and computational image analysis to precisely monitor when a bacterium invades, proliferates, and is destroyed by xenophagy. Here, the use of markers for the bacterium's intracellular localization will be essential, e.g., lysosome-associated membrane protein 1 (LAMP1) [204] or dextran [193] to visualize the SCV. In particular, for the open question of the effect of xenophagy on the *Salmonella* population inside the cytosol, it is essential to shift away from population-based studies towards single-cell analysis or even single-bacterium analysis [205].

The third contribution of this work was the development of novel computational methods that allow to reveal the entire dependencies between the components of a signaling pathway. The state-of-the-art methods for *in silico* knockout analyses detect dependencies between T-invariants, EFM, or extreme pathways, but the knockout effects are not comparable to those of experimental perturbations. We established a novel computational method that facilitates *in silico* knockouts considering the biological dependencies for mathematical models in the PN formalism. The proposed *in silico* knockout analysis ensures the maintenance of the turnover of pathway components under knockout conditions, thus predicts knockout behavior that is comparable with experimental perturbation data. In this context, we developed and applied the concept of Manatee invariants. We demonstrated the suitability of Manatee invariants for the knockout analysis by revealing all possible ways of signal flow in pathways.

In signaling pathways, which are in the most cases densely and highly interconnected, even for experts of the particular area, it is challenging to forecast the effects of knockouts on the pathway components. Here, the computational predictions by the presented knockout analysis provide valuable hints, which enable to address important issues. The biological functional dependencies of signaling pathways can be uncovered. The PN model can be verified by the comparison of the knockout predictions with experimental perturbation studies. Errors in PN model or inconsistencies in the present knowledge of the pathway can be detected. *In silico* knockouts can also be

used for network validation by predicting knockout behavior that can be tested in future experiments. Furthermore, components can be identified to which the pathway is particularly sensitive or insensitive. These predictions can improve the knowledge of the pathway and give worthwhile hints, e.g., for the development of potential therapeutic treatments. While we focus on signaling pathways, the method may also be applied to other biological systems. The future application of *in silico* knockouts to, e.g., models of metabolic pathways will confirm the usefulness of the method for other biological systems.

To generate knockout predictions that can be compared with experimental data, the PN of a signaling pathway has to be modeled at a high level of detail. Here, it is often necessary, e.g., to model all orders of binding events in which protein complexes form. The modeling of all possible combinations leads to huge networks due to combinatorial complexity [174]. The construction of PN for signaling pathways at such a high level of detail requires a lot of information about these processes. The iterative process of model development of such detailed networks can be elaborating and time-consuming. Moreover, the determination of T-invariants for such huge PN can become computationally hard [132,133]. The development of efficient algorithms for the computation of T-invariants or Manatee invariants was out of scope of this work but is an important issue for future research and will facilitate the application of *in silico* knockouts for huge networks with large number of T-invariants.

The knockout analysis provides qualitative information about whether pathway components are affected by a knockout and which parts of the pathway are not functional. No information can be given about the quantitative amount of pathway components after the knockout. An idea for future work would be to quantify the number of unaffected Manatee invariants that still produce a specific pathway component after the knockout. However, this would only give an impression about the redundancy by which the pathway component is generated and how this redundancy is affected by the knockout. Only a kinetic model with the knowledge of a sufficiently large set of kinetic constants and concentrations can predict such quantitative knockout effects.

The presented knockout analysis represents a new method to predict the effects of experimental perturbations. The examination of the model behavior to perturbations enables to address important issues, such as dependencies of biological pathways, identification of potential targets for drug treatment, and predictions of unknown effects of perturbations. The knockout matrix summarizes the global dependencies of pathways and elucidates a multiplicity of predictions about the effects of *in silico* knockouts. As a proof of principle, we demonstrated the usefulness of the proposed concept of *in silico* knockout by its application to the PN of the xenophagic capturing of *Salmonella*. The application of knockout analysis to other biological pathways represents a possible way to further validate the novel method.

The last contribution was the development of the software isiKnock to automatically and systematically explore the knockout behavior of signaling pathways expressed as PN models and to enable the application of the new theoretical method for researchers. The software isiKnock visualizes the knockout predictions in form of the *in silico* knockout matrix and provides a user-friendly GUI.

Taken together, we studied bacterial infections at different levels of abstraction with approaches from computational systems biology. The knockout analysis uncovers the biological functional dependencies of the xenophagic capturing of *Salmonella*, and the SPN simulates the quantitative behavior of a *Salmonella*-infected cell. Both approaches contribute to a better understanding of bacterial infections and support the research on antimicrobial-resistance of bacteria. Moreover, the presented methods of *in silico* knockout and Manatee invariants, including the software isiKnock, provide valuable verification and validation techniques in computational systems biology.

Chapter 6

Appendix

Table A1

Places of the PN of the xenophagic capturing of *Salmonella*

Place	Description
SCV	*Salmonella* inside the SCV
SdamagedSCV	*Salmonella* inside a damaged SCV
Scyt	*Salmonella* inside the cytosol
Gal8	Galectin-8
LRSAM1	Ubiquitin ligase LRSAM1
E3ligase	Unknown E3 ligase or E3 ligases
NDP52	Autophagy receptor NDP52
SigNDP52	Signal of NDP52 binding to galectin-8-positive and ubiquitin-positive *Salmonella*
SigNDP52i	Signal of NDP52 binding to ubiquitin-positive *Salmonella*
OPTN	Autophagy receptor OPTN
SigOPTN	Signal of OPTN binding to galectin-8-positive and ubiquitin-positive *Salmonella*
SigOPTNi	Signal of OPTN binding to ubiquitin-positive *Salmonella*
p62	Autophagy receptor p62
Sigp62	Signal of p62 binding to galectin-8-positive and ubiquitin-positive *Salmonella*
Sigp62i	Signal of p62 binding to ubiquitin-positive *Salmonella*
diTBK1	Dimeric TBK1
SigdiTBK1	Signal of TBK1 dimer binding to galectin-8-positive and ubiquitin-positive *Salmonella*
SigdiTBK1i	Signal of another TBK1 dimer binding to galectin-8-positive and ubiquitin-positive *Salmonella*

Place	Description
SigdiTBK1ii	Signal of TBK1 dimer binding to ubiquitin-positive *Salmonella*
SigdiTBK1iii	Signal of another TBK1 dimer binding to ubiquitin-positive *Salmonella*
NS	NAP1 or SINTBAD
SigNS	Signal of NAP1/SINTBAD binding to galectin-8-positive and ubiquitin-positive *Salmonella*
SigNSi	Signal of NAP1/SINTBAD binding to ubiquitin-positive *Salmonella*
S:Gal8	Complex of *Salmonella* and galectin-8
S:Gal8:NDP52	Complex of *Salmonella*, galectin-8, and NDP52
S:Gal8:Ub	Complex of *Salmonella*, galectin-8, and ubiquitin
S:Gal8:Ub:p62	Complex of *Salmonella*, galectin-8, ubiquitin, and p62
S:Gal8:Ub:OPTN	Complex of *Salmonella*, galectin-8, ubiquitin, and OPTN
S:Gal8:Ub:NDP52	Complex of *Salmonella*, galectin-8, ubiquitin, and NDP52
S:Gal8:Ub:NDP52:NS	Complex of *Salmonella*, galectin-8, ubiquitin, NDP52, and NAP1/SINTBAD
S:Gal8:Ub:NDP52:OPTN:p62	Complex of *Salmonella*, galectin-8, ubiquitin, NDP52, OPTN, and p62
S:Gal8:Ub:NDP52:OPTN:p62:NS	Complex of *Salmonella*, galectin-8, ubiquitin, NDP52, OPTN, p62, and NAP1/SINTBAD
S:Gal8:Ub:NDP52:OPTN:p62:NS:-diTBK1	Complex of *Salmonella*, galectin-8, ubiquitin, NDP52, OPTN, p62, NAP1/SINTBAD, and dimeric TBK1
S:Gal8:Ub:NDP52:OPTN:p62:NS:-diTBK1i	Complex of *Salmonella*, galectin-8, ubiquitin, NDP52, OPTN, p62, NAP1/SINTBAD, and another dimeric TBK1
S:Gal8:Ub:NDP52:OPTNp:p62:NS:-OligoTBK1	Complex of *Salmonella*, galectin-8, ubiquitin, NDP52, phosphorylated OPTN, p62, NAP1/SINTBAD, and oligomerized TBK1 dimers
S:Ub	Complex of *Salmonella* and ubiquitin
S:Ub:p62	Complex of *Salmonella*, ubiquitin, and p62
S:Ub:OPTN	Complex of *Salmonella*, ubiquitin, and OPTN
S:Ub:NDP52	Complex of *Salmonella*, ubiquitin, and NDP52
S:Ub:NDP52:NS	Complex of *Salmonella*, ubiquitin, NDP52, and NAP1/SINTBAD
S:Ub:NDP52:OPTN:p62	Complex of *Salmonella*, ubiquitin, NDP52, OPTN, and p62
S:Ub:NDP52:OPTN:p62:NS	Complex of *Salmonella*, ubiquitin, NDP52, OPTN, p62, and NAP1/SINTBAD
S:Ub:NDP52:OPTN:p62:NS:diTBK1	Complex of *Salmonella*, ubiquitin, NDP52, OPTN, p62, NAP1/SINTBAD, and dimeric TBK1

Place	Description
S:Ub:NDP52:OPTN:p62:NS:diTBK1i	Complex of *Salmonella*, ubiquitin, NDP52, OPTN, p62, NAP1/SINTBAD, and another dimeric TBK1
S:Ub:NDP52:OPTNp:p62:NS:-OligoTBK1	Complex of *Salmonella*, ubiquitin, NDP52, phosphorylated OPTN, p62, NAP1/SINTBAD, and oligomerized TBK1 dimers
LC3/GABARAP:AM	LC3/GABARAP-positive autophagosomal membrane
SCVdamage	Signal of the SCV damage
AA	Normal AA level in the cell
AAstarvation	AA starvation in the cell
mTORC1:ULK1c	Complex of activated mTORC1 and the inactivated ULK1 complex
mTORC1:ULK1c:SCV	Complex of activated mTORC1 on the SCV and the inactivated ULK1 complex
mTORC1inactive	Inactivated mTORC1 (formed by mTOR, Raptor, and mLST8)
ULK1c	Activated ULK1 complex (formed by ULK1, FIP200, ATG13, and ATG101)
SigAAstarvation	Signal of AA starvation
SigAA	Signal of normalized AA level
SigAutophagyInduction	Signal of the autophagy induction
Ap:S:Gal8:NDP52	*Salmonella* trapped by the LC3/GABARAP-positive autophagosomal membrane, including galectin-8, and NDP52
Ap:S:Gal8:Ub:NDP52:OPTN:p62	*Salmonella* trapped by the LC3/GABARAP-positive autophagosomal membrane, including galectin-8, ubiquitin, NDP52, OPTN, and p62
Ap:S:Gal8:Ub:NDP52:OPTN:p62:NS	*Salmonella* trapped by the LC3/GABARAP-positive autophagosomal membrane, including galectin-8, ubiquitin, NDP52, OPTN, p62, and NAP1/SINTBAD
Ap:S:Gal8:Ub:NDP52:OPTNp:p62:-NS:TBK1	*Salmonella* trapped by the LC3/GABARAP-positive autophagosomal membrane, including galectin-8, ubiquitin, NDP52, phosphorylated OPTN, p62, NAP1/SINTBAD, and TBK1 dimers
Ap:S:Ub:NDP52:OPTN:p62	*Salmonella* trapped by the LC3/GABARAP-positive autophagosomal membrane, including ubiquitin, NDP52, OPTN, and p62
Ap:S:Ub:NDP52:OPTN:p62:NS	*Salmonella* trapped by the LC3/GABARAP-positive autophagosomal membrane, including ubiquitin, NDP52, OPTN, p62, and NAP1/SINTBAD
Ap:S:Ub:NDP52:OPTNp:p62:NS:TBK1	*Salmonella* trapped by the LC3/GABARAP-positive autophagosomal membrane, including ubiquitin, NDP52, phosphorylated OPTN, p62, NAP1/SINTBAD, and TBK1 dimers

Table A2

Transitions of the PN of the xenophagic capturing of *Salmonella*

Transition	Description	Reference
Inv	Invasion of *Salmonella* into the epithelial cell	[23, 26]
SCVdamage	Disruption of the SCV	[11, 15]
U1	Binding of LRSAM1 and other unknown E3 ligases to galectin-8-positive *Salmonella* and ubiquitination of *Salmonella*	[12, 150, 151]
U2	Binding of LRSAM1 and other unknown E3 ligases to galectin-8-positive and NDP52-positive *Salmonella* and ubiquitination of *Salmonella*	[12, 150, 151]
U3	Binding of LRSAM1 to cytosolic *Salmonella* and ubiquitination of *Salmonella*	[12, 150, 151]
R1	Recruitment of galectin-8 to host glycans exposed on SCV	[36]
R2	Recruitment of NDP52 to galectin-8	[36, 149]
R3	Recruitment of NDP52 to galectin-8-positive and ubiquitin-positive *Salmonella*	[31, 36, 149]
R4	Recruitment of OPTN to ubiquitin-positive and galectin-8-positive *Salmonella*	[30]
R5	Recruitment of p62 to ubiquitin-positive and galectin-8-positive *Salmonella*	[29]
R6	Recruitment of p62 to ubiquitin-positive *Salmonella*	[29]
R7	Recruitment of OPTN to ubiquitin-positive *Salmonella*	[30]
R8	Recruitment of NDP52 to ubiquitin-positive *Salmonella*	[31]
R9	Recruitment of NAP1/SINTBAD to galectin-8-positive, ubiquitin-positive, and NDP52-positive *Salmonella*	[31]
R10	Recruitment of NAP1/SINTBAD to ubiquitin-positive and NDP52-positive *Salmonella*	[31]
R11	Recruitment of NAP1/SINTBAD to galectin-8-positive, ubiquitin-positive, NDP52-positive, p62-positive, and OPTN-positive *Salmonella*	[31]
R12	Recruitment of NAP1/SINTBAD to ubiquitin-positive, NDP52-positive, p62-positive, and OPTN-positive *Salmonella*	[31]
R13	Recruitment of dimeric TBK1 to OPTN and NDP52 via NAP1/SINTBAD	[31, 161, 163, 207]
R14	Recruitment of another dimeric TBK1 to OPTN and NDP52 via NAP1/SINTBAD	[31, 161, 163, 207]
R15	Recruitment of dimeric TBK1 to OPTN-positive and NDP52-positive cytosolic *Salmonella* via NAP1/SINTBAD	[31, 161, 163, 207]

Transition	Description	Reference
R16	Recruitment of another dimeric TBK1 to OPTN-positive and NDP52-positive cytosolic *Salmonella* via NAP1/SINTBAD	[31, 161, 163, 207]
R17	Recruitment of LC3/GABARAP proteins to the autophagosomal membrane to galectin-8-positive and NDP52-positive *Salmonella*, leading to autophagosome formation	[34, 36, 149]
R18	Recruitment of LC3/GABARAP proteins to the autophagosomal membrane to galectin-8-positive, ubiquitin-positive, NDP52-positive, p62-positive, phosphorylated OPTN-positive, NAP1/SINTBAD-positive, and TBK1-positive *Salmonella*, leading to autophagosome formation	[30, 34, 158, 159]
R19	Recruitment of LC3/GABARAP proteins to the autophagosomal membrane to galectin-8-positive, ubiquitin-positive, NDP52-positive, p62-positive, OPTN-positive, NAP1/SINTBAD-positive *Salmonella*, leading to autophagosome formation	[34]
R20	Recruitment of LC3/GABARAP proteins to the autophagosomal membrane to galectin-8-positive, ubiquitin-positive, NDP52-positive, p62-positive, and OPTN-positive *Salmonella*, leading to autophagosome formation	[34]
R21	Recruitment of LC3/GABARAP proteins to the autophagosomal membrane to ubiquitin-positive, NDP52-positive, p62-positive, and OPTN-positive *Salmonella*, leading to autophagosome formation	[34]
R22	Recruitment of LC3/GABARAP proteins to the autophagosomal membrane to ubiquitin-positive, NDP52-positive, p62-positive, OPTN-positive, and NAP1/SINTBAD-positive *Salmonella*, leading to autophagosome formation	[34]
R23	Recruitment of LC3/GABARAP proteins to the autophagosomal membrane to ubiquitin-positive, NDP52-positive, p62-positive, phosphorylated OPTN-positive, NAP1/SINTBAD-positive, and TBK1-positive *Salmonella*, leading to autophagosome formation	[30, 158, 159]
S1	Signal of NDP52 binding to galectin-8-positive and ubiquitin-positive *Salmonella*	[31, 36, 149]
S2	Signal of OPTN binding to galectin-8-positive and ubiquitin-positive *Salmonella*	[30]
S3	Signal of p62 binding to galectin-8-positive and ubiquitin-positive *Salmonella*	[29]
S4	Signal of p62 binding to ubiquitin-positive *Salmonella*	[29]

Transition	Description	Reference
S5	Signal of OPTN binding to ubiquitin-positive *Salmonella*	[30]
S6	Signal of NDP52 binding to ubiquitin-positive *Salmonella*	[31]
S7	Signal of NAP1/SINTBAD binding to galectin-8-positive, ubiquitin-positive, and NDP52-positive *Salmonella*	[31]
S8	Signal of NAP1/SINTBAD binding to ubiquitin-positive and NDP52-positive cytosolic *Salmonella*	[31]
S9	Signal of dimeric TBK1 binding to OPTN and NDP52 via NAP1/SINTBAD	[31, 161, 163, 207]
S10	Signal of another dimeric TBK1 binding to OPTN and NDP52 via NAP1/SINTBAD	[31, 161, 163, 207]
S11	Signal of dimeric TBK1 binding to OPTN-positive and NDP52-positive cytosolic *Salmonella* via NAP1/SINTBAD	[31, 161, 163, 207]
S12	Signal of another dimeric TBK1 binding to OPTN-positive and NDP52-positive cytosolic *Salmonella* via NAP1/SINTBAD	[31, 161, 163, 207]
S13	Signal of SCV damage triggers AA starvation	[171, 172]
S14	Activated ULK1 complex induces autophagy	[173]
S15	Activated ULK1 complex induces formation of phagophores	[173]
S16	Signal of AA starvation triggers mTORC1 inactivation	[171–173]
S17	Signal of normalized AA level triggers mTORC1 reactivation	[171–173]
F1	Complex formation of the three autophagy receptors, p62, OPTN, and NDP52, with galectin-8-positive and ubiquitin-positive *Salmonella*	[29–31, 36, 149]
F2	Complex formation of the three autophagy receptors, p62, OPTN, and NDP52, with ubiquitin-positive *Salmonella*	[29–31, 36, 149]
F3	Complex formation of the autophagy receptors, p62 and OPTN, with galectin-8-positive and ubiquitin-positive *Salmonella* complex, including the NDP52-NAP1/SINTBAD complex	[29, 30]
F4	Complex formation of the autophagy receptors, p62 and OPTN, with ubiquitin-positive *Salmonella* complex, including the NDP52-NAP1/SINTBAD complex	[29, 30]
F5	Oligomerization of TBK1 leads to autoactivation and phosphorylation of OPTN at cytosolic *Salmonella* inside the damaged SCV	[155, 162–164, 166]
F6	Oligomerization of TBK1 leads to autoactivation and phosphorylation of OPTN at cytosolic *Salmonella*	[155, 162–164, 166]
Cyt	*Salmonella* escape from the damaged SCV and get cytosolic access	[34, 188]

Transition	Description	Reference
A1	Normalization of the AA level leads to mTORC1 reactivation and mTORC1 localizes to the surface of the SCV, resulting in inactivation of the ULK1 complex	[171–173]
I1	AA starvation leads to the inactivation of mTORC1 and its dissociation of the ULK1 complex	[171–173]
Deg1	Degradation of the autophagosome through fusion with the lysosome	[23, 26]
Deg2	Degradation of the autophagosome through fusion with the lysosome	[23, 26]
Deg2i	Degradation of the autophagosome through fusion with the lysosome	[23, 26]
Deg2ii	Degradation of the autophagosome through fusion with the lysosome	[23, 26]
Deg3	Degradation of the autophagosome through fusion with the lysosome	[23, 26]
Deg3i	Degradation of the autophagosome through fusion with the lysosome	[23, 26]
Deg3ii	Degradation of the autophagosome through fusion with the lysosome	[23, 26]
DegAA	AA degradation	
Out	Removal of the complex between mTORC1 and the ULK1 complex	
Norm	Normalization of the AA level	[171, 172]
SynAA	AA generation	
SynGal8	Synthesis of galectin-8	
SynLRSAM1	Synthesis of LRSAM1	
SynE3ligase	Synthesis of other E3-ligases	
Synp62	Synthesis of p62	
SynNDP52	Synthesis of NDP52	
SynOPTN	Synthesis of OPTN	
SynNS	Synthesis of NAP1/SINTBAD	
SynTBK1	Synthesis of TBK1 and its dimerization	
FmTORC1:-ULK1c	Formation of active mTORC1 and the inactivated ULK1 complex	[173]
Esc	Escape of *Salmonella* from the damaged SCV	

Table A3

P-invariants of the PN of the xenophagic capturing of *Salmonella*

Places	Biological Meaning
$\boldsymbol{pi_1}$	
SigAutophagyInduction, mTORC1:ULK1c:SCV, mTORC1:ULK1c, ULK1c	Conservation of the ULK1 complex
$\boldsymbol{pi_2}$	
Ap:S:Ub:NDP52:OPTN:p62, S:Ub:OPTN, S:Ub:NDP52:OPTNp:p62:NS:-OligoTBK1, S:Ub:NDP52:OPTN:p62:NS:diTBK1i, S:Ub:NDP52:OPTN:-p62:NS:diTBK1, SigOPTNi, Ap:S:Gal8:Ub:NDP52:p62:OPTNp:NS:TBK1, S:Gal8:Ub:NDP52:p62:OPTNp:NS:OligoTBK1, Ap:S:Ub:NDP52:OPTNp:-p62:NS:TBK1, SigOPTN, Ap:S:Ub:NDP52:OPTN:p62:NS, S:Gal8:Ub:-NDP52:OPTN:p62:NS:diTBK1, S:Gal8:Ub:NDP52:OPTN:p62:NS, S:Ub:-NDP52:OPTN:p62:NS, S:Gal8:Ub:OPTN, OPTN, S:Ub:NDP52:OPTN:p62, S:Gal8:Ub:NDP52:OPTN:p62, S:Gal8:Ub:NDP52:OPTN:p62:NS:diTBK1i, Ap:S:Gal8:Ub:NDP52:OPTN:p62:NS, Ap:S:Gal8:Ub:NDP52:OPTN:p62	Conservation of OPTN
$\boldsymbol{pi_3}$	
AA, AAstarvation, SigAA, SigAAstarvation	Conservation of the AA signal
$\boldsymbol{pi_4}$	
Ap:S:Ub:NDP52:OPTN:p62, S:Ub:NDP52:OPTNp:p62:NS:OligoTBK1, S:-Ub:NDP52:OPTN:p62:NS:diTBK1i, SigNDP52, S:Ub:NDP52:OPTN:p62:NS:-diTBK1, S:Gal8:Ub:NDP52, Ap:S:Ub:NDP52:OPTNp:p62:NS:TBK1, Ap:S:Ub:-NDP52:OPTN:p62:NS, S:Gal8:NDP52, S:Ub:NDP52:OPTN:p62:NS, S:Gal8:Ub:-NDP52:OPTN:p62:NS, S:Ub:NDP52:OPTN:p62, S:Gal8:Ub:NDP52:OPTN:p62, Ap:Gal8:NDP52, S:Ub:NDP52, Ap:S:Gal8:Ub:NDP52:p62:OPTNp:NS:TBK1, S:Gal8:Ub:NDP52:p62:OPTNp:NS:OligoTBK1, S:Ub:NDP52:NS, SigNSi, NDP52, S:Gal8:Ub:NDP52:OPTN:p62:NS:diTBK1, SigNDP52i, S:Gal8:-Ub:NDP52:OPTN:p62:NS:diTBK1i, Ap:S:Gal8:Ub:NDP52:OPTN:p62:NS, Ap:S:Gal8:Ub:NDP52:OPTN:p62, S:Gal8:Ub:NDP52:NS, SigNS	Conservation of NDP52

Places	Biological Meaning
pi_5	
Ap:S:Ub:NDP52:OPTN:p62, S:Ub:NDP52:OPTNp:p62:NS:OligoTBK1, S:Ub:NDP52:OPTN:p62:NS:diTBK1i, S:Ub:NDP52:OPTN:p62:NS:diTBK1, S:Gal8:Ub:NDP52, LRSAM1, S:Gal8:Ub:p62, Ap:S:Ub:NDP52:OPTNp:p62:NS:TBK1, Ap:S:Ub:NDP52:OPTN:p62:NS, S:Gal8:Ub, S:Ub:NDP52:OPTN:p62:NS, S:Gal8:Ub:NDP52:OPTN:p62:NS, S:Gal8:Ub:OPTN, S:Ub:NDP52:OPTN:p62, S:Gal8:Ub:NDP52:OPTN:p62, S:Ub:OPTN, S:Ub:p62, S:Ub:NDP52, Ap:S:Gal8:Ub:NDP52:p62:OPTNp:NS:TBK1, S:Gal8:Ub:NDP52:p62:OPTNp:NS:OligoTBK1, S:Ub:NDP52:NS, S:Gal8:Ub:NDP52:OPTN:p62:NS:diTBK1, S:Gal8:Ub:NDP52:OPTN:p62:NS:diTBK1i, Ap:S:Gal8:Ub:NDP52:OPTN:p62:NS, Ap:S:Gal8:Ub:NDP52:OPTN:p62, S:Gal8:Ub:NDP52:NS, S:Ub	Conservation of LRSAM1
pi_6	
S:Ub:NDP52:OPTNp:p62:NS:OligoTBK1, S:Ub:NDP52:OPTN:p62:NS:diTBK1i, S:Ub:NDP52:OPTN:p62:NS:diTBK1, Ap:S:Gal8:Ub:NDP52:p62:OPTNp:NS:TBK1, S:Gal8:Ub:NDP52:p62:OPTNp:NS:OligoTBK1, Ap:S:Ub:NDP52:OPTNp:p62:NS:TBK1, Ap:S:Ub:NDP52:OPTN:p62:NS, S:Ub:NDP52:NS, S:Gal8:Ub:NDP52:OPTN:p62:NS:diTBK1, SigNSi, S:Ub:NDP52:OPTN:p62:NS, NS, S:Gal8:Ub:NDP52:OPTN:p62:NS, S:Gal8:Ub:NDP52:OPTN:p62:NS:diTBK1i, Ap:S:Gal8:Ub:NDP52:OPTN:p62:NS, S:Gal8:Ub:NDP52:NS, SigNS	Conservation of NAP1/-SINTBAD
pi_7	
Ap:S:Ub:NDP52:OPTN:p62, S:Ub:NDP52:OPTNp:p62:NS:OligoTBK1, SdamagedSCV, Scyt, S:Ub:NDP52:OPTN:p62:NS:diTBK1i, S:Ub:NDP52:OPTN:p62:NS:diTBK1, S:Gal8:Ub:NDP52, S:Gal8, S:Gal8:Ub:p62, Ap:S:Ub:NDP52:OPTNp:p62:NS:TBK1, Ap:S:Ub:NDP52:OPTN:p62:NS, S:Gal8:NDP52, S:Gal8:Ub, S:Gal8:Ub:NDP52:OPTN:p62:NS, S:Ub:NDP52:OPTN:p62:NS, S:Gal8:Ub:OPTN, S:Ub:NDP52:OPTN:p62, S:Gal8:Ub:NDP52:OPTN:p62, S:Ub:OPTN, S:Ub:p62, S:Ub:NDP52, Ap:Gal8:NDP52, Ap:S:Gal8:Ub:NDP52:p62:OPTNp:NS:TBK1, S:Gal8:Ub:NDP52:p62:OPTNp:NS:OligoTBK1, S:Ub:NDP52:NS, S:Gal8:Ub:NDP52:OPTN:p62:NS:diTBK1, S:Gal8:Ub:NDP52:OPTN:p62:NS:diTBK1i, Ap:S:Gal8:Ub:NDP52:OPTN:p62:NS, Ap:S:Gal8:Ub:NDP52:OPTN:p62, S:Gal8:Ub:NDP52:NS, SCV, S:Ub	Conservation of *Salmonella*
pi_8	
mTORC1:ULK1c:SCV, mTORC1:ULK1c, mTORC1inactive	Conservation of mTORC1

Places	Biological Meaning
pi_9	
Ap:S:Ub:NDP52:OPTN:p62, S:Ub:NDP52:OPTNp:p62:NS:OligoTBK1, S:Ub:NDP52:OPTN:p62:NS:diTBK1i, S:Ub:NDP52:OPTN:p62:NS:diTBK1, E3ligase, S:Gal8:Ub:NDP52, S:Gal8:Ub:p62, Ap:S:Ub:NDP52:OPTNp:p62:NS:TBK1, Ap:S:Ub:NDP52:OPTN:p62:NS, S:Gal8:Ub, S:Ub:NDP52:OPTN:p62:NS, S:Gal8:Ub:NDP52:OPTN:p62:NS, S:Gal8:Ub:OPTN, S:Ub:NDP52:OPTN:p62, S:Gal8:Ub:NDP52:OPTN:p62, S:Ub:OPTN, S:Ub:p62, S:Ub:NDP52, Ap:S:Gal8:Ub:NDP52:p62:OPTNp:NS:TBK1, S:Gal8:Ub:NDP52:p62:OPTNp:NS:OligoTBK1, S:Ub:NDP52:NS, S:Gal8:Ub:NDP52:OPTN:p62:NS:diTBK1, S:Gal8:Ub:NDP52:OPTN:p62:NS:diTBK1i, Ap:S:Gal8:Ub:NDP52:OPTN:p62:NS, Ap:S:Gal8:Ub:NDP52:OPTN:p62, S:Gal8:Ub:NDP52:NS, S:Ub	Conservation of E3ligase
pi_{10}	
Ap:Gal8:NDP52, Gal8, S:Gal8, S:Gal8:Ub:NDP52, Ap:S:Gal8:Ub:NDP52:p62:OPTNp:NS:TBK1, S:Gal8:Ub:p62, S:Gal8:Ub:NDP52:p62:OPTNp:NS:OligoTBK1, S:Gal8:NDP52, S:Gal8:Ub:NDP52:OPTN:p62:NS:diTBK1, S:Gal8:Ub, S:Gal8:Ub:NDP52:OPTN:p62:NS, S:Gal8:Ub:OPTN, S:Gal8:Ub:NDP52:OPTN:p62, S:Gal8:Ub:NDP52:OPTN:p62:NS:diTBK1i, Ap:S:Gal8:Ub:NDP52:OPTN:p62:NS, Ap:S:Gal8:Ub:NDP52:OPTN:p62, S:Gal8:Ub:NDP52:NS	Conservation of galectin-8
pi_{11}	
Ap:S:Ub:NDP52:OPTN:p62, S:Ub:NDP52:OPTNp:p62:NS:OligoTBK1, S:Ub:p62, S:Ub:NDP52:OPTN:p62:NS:diTBK1i, S:Ub:NDP52:OPTN:p62:NS:diTBK1, p62, Ap:S:Gal8:Ub:NDP52:p62:OPTNp:NS:TBK1, S:Gal8:Ub:p62, Sigp62, S:Gal8:Ub:NDP52:p62:OPTNp:NS:OligoTBK1, Ap:S:Ub:NDP52:OPTNp:p62:NS:TBK1, Ap:S:Ub:NDP52:OPTN:p62:NS, S:Gal8:Ub:NDP52:OPTN:p62:NS:diTBK1, S:Gal8:Ub:NDP52:OPTN:p62:NS, S:Ub:NDP52:OPTN:p62:NS, Sigp62i, S:Ub:NDP52:OPTN:p62, S:Gal8:Ub:NDP52:OPTN:p62, S:Gal8:Ub:NDP52:OPTN:p62:NS:diTBK1i, Ap:S:Gal8:Ub:NDP52:OPTN:p62:NS, Ap:S:Gal8:Ub:NDP52:OPTN:p62	Conservation of p62
pi_{12}	
2*S:Ub:NDP52:OPTNp:p62:NS:OligoTBK1, SigdiTBK1iii, SigdiTBK1ii, S:Ub:NDP52:OPTN:p62:NS:diTBK1i, S:Ub:NDP52:OPTN:p62:NS:diTBK1, 2*Ap:S:Gal8:Ub:NDP52:p62:OPTNp:NS:TBK1, 2*S:Gal8:Ub:NDP52:p62:OPTNp:NS:OligoTBK1, 2*Ap:S:Ub:NDP52:OPTNp:p62:NS:TBK1, diTBK1, S:Gal8:Ub:NDP52:OPTN:p62:NS:diTBK1, SigdiTBK1, SigdiTBK1i, S:Gal8:Ub:NDP52:OPTN:p62:NS:diTBK1i	Conservation of the TBK1 dimer

Table A4

T-invariants of the PN of the xenophagic capturing of *Salmonella*

Transitions	Biological Meaning
ti_1	
Disr, Deg3, S13, S6, S5, S4, U3, S14, SynNS, SynNDP52, R15, R12, SynOPTN, F2, R23, S12, F6, R16, S11, R7, R8, R6, Synp62, Inv, SynLRSAM1, Cyt, SynE3ligase, S15, 2*SynTBK1, Norm	Ubiquitin-dependent xenophagy of cytosolic *Salmonella*, including phosphorylation of OPTN
ti_2	
Disr, Deg3i, S13, S6, S5, S4, U3, S14, SynNS, SynNDP52, R12, SynOPTN, F2, R22, R7, R8, R6, Synp62, Inv, SynLRSAM1, Cyt, SynE3ligase, S15, Norm	Ubiquitin-dependent xenophagy of cytosolic *Salmonella*, including NAP1/SINTBAD
ti_3	
Disr, R1, SynGal8, S13, S2, S3, S14, SynNS, SynNDP52, SynOPTN, U1, R3, R5, R4, Synp62, Inv, SynLRSAM1, SynE3ligase, S15, R9, S7, R19, Deg2i, F3, Norm	Galectin-8-dependent and ubiquitin-dependent xenophagy of vacuolar *Salmonella*, including NAP1/SINTBAD
ti_4	
Disr, R1, F1, SynGal8, S1, S13, S2, S3, S14, SynNS, SynNDP52, SynOPTN, U1, R3, R5, R4, R11, Synp62, Inv, SynLRSAM1, SynE3ligase, S15, R19, Deg2i, Norm	Galectin-8-dependent and ubiquitin-dependent xenophagy of vacuolar *Salmonella*, including NAP1/SINTBAD
ti_5	
Disr, R1, F1, SynGal8, S1, S13, S2, S3, S14, SynNDP52, SynOPTN, U1, R3, R5, R4, Synp62, Inv, SynLRSAM1, S15, SynE3ligase, R20, Deg2ii, Norm	Galectin-8-dependent and ubiquitin-dependent xenophagy of vacuolar *Salmonella*
ti_6	
Disr, R1, SynGal8, S13, S2, S3, S14, SynNS, SynNDP52, SynOPTN, U1, R3, R5, R4, R13, Deg2, R18, Synp62, Inv, SynLRSAM1, S9, R14, SynE3ligase, S15, S10, F5, 2*SynTBK1, R9, S7, F3, Norm	Galectin-8-dependent and ubiquitin-dependent xenophagy of vacuolar *Salmonella*, including phosphorylation of OPTN
ti_7	
Disr, Deg3, S13, S5, S4, U3, S14, SynNS, R15, SynNDP52, SynOPTN, R23, S12, F6, R16, S11, R7, R8, R6, Synp62, Inv, SynLRSAM1, Cyt, R10, SynE3ligase, S15, S8, 2*SynTBK1, F4, Norm	Ubiquitin-dependent xenophagy of cytosolic *Salmonella*, including phosphorylation of OPTN

Transitions	Biological Meaning
ti_8	
Disr, R1, SynGal8, R2, S13, S2, S3, S14, SynNS, SynNDP52, SynOPTN, U2, R5, R4, Synp62, Inv, SynLRSAM1, SynE3ligase, S15, R9, S7, R19, Deg2i, F3, Norm	Galectin-8-dependent and ubiquitin-dependent xenophagy of vacuolar *Salmonella*, including NAP1/SINTBAD
ti_9	
Disr, S13, S6, S5, S4, U3, S14, SynNDP52, SynOPTN, F2, Deg3ii, R21, R7, R8, R6, Synp62, Inv, SynLRSAM1, Cyt, SynE3ligase, S15, Norm	Ubiquitin-dependent xenophagy of cytosolic *Salmonella*
ti_{10}	
Disr, Deg3i, S13, S5, S4, U3, S14, SynNS, SynNDP52, SynOPTN, R22, R7, R8, R6, Synp62, Inv, SynLRSAM1, R10, Cyt, SynE3ligase, S15, S8, F4, Norm	Ubiquitin-dependent xenophagy of cytosolic *Salmonella*, including NAP1/SINTBAD
ti_{11}	
Disr, R1, F1, SynGal8, S1, R2, S13, S2, S3, S14, SynNS, SynNDP52, SynOPTN, U2, R5, R4, R11, Synp62, Inv, SynLRSAM1, SynE3ligase, S15, R19, Deg2i, Norm	Galectin-8-dependent and ubiquitin-dependent xenophagy of vacuolar *Salmonella*, including NAP1/SINTBAD
ti_{12}	
Disr, R1, F1, SynGal8, S1, R2, S13, S2, S3, S14, SynNDP52, SynOPTN, U2, R5, R4, Synp62, Inv, SynLRSAM1, S15, SynE3ligase, R20, Deg2ii, Norm	Galectin-8-dependent and ubiquitin-dependent xenophagy of vacuolar *Salmonella*
ti_{13}	
Disr, R17, R1, Deg1, SynGal8, R2, S13, S14, Inv, SynNDP52, S15, Norm	Galectin-8-dependent xenophagy of vacuolar *Salmonella*
ti_{14}	
Disr, R1, F1, SynGal8, S1, R2, S13, S2, S3, S14, SynNS, SynNDP52, SynOPTN, U2, R5, R4, R11, R13, Deg2, R18, Synp62, Inv, SynLRSAM1, S9, SynE3ligase, R14, S15, S10, F5, 2*SynTBK1, Norm	Galectin-8-dependent and ubiquitin-dependent xenophagy of vacuolar *Salmonella*, including phosphorylation of OPTN
ti_{15}	
Disr, R1, F1, SynGal8, S1, S13, S2, S3, S14, SynNS, SynNDP52, SynOPTN, U1, R3, R5, R4, R11, R13, Deg2, R18, Synp62, Inv, SynLRSAM1, S9, SynE3ligase, R14, S15, S10, F5, 2*SynTBK1, Norm	Galectin-8-dependent and ubiquitin-dependent xenophagy of vacuolar *Salmonella*, including phosphorylation of OPTN

Transitions	Biological Meaning
$\boldsymbol{ti_{16}}$	
Disr, R1, SynGal8, R2, S13, S2, S3, S14, SynNS, SynNDP52, SynOPTN, U2, R5, R4, R13, Deg2, R18, Synp62, Inv, SynLRSAM1, S9, R14, SynE3ligase, S15, S10, F5, 2*SynTBK1, R9, S7, F3, Norm	Galectin-8-dependent and ubiquitin-dependent xenophagy of vacuolar *Salmonella*, including phosphorylation of OPTN
$\boldsymbol{ti_{17}}$	
Inv, Disr, S13, Norm, Esc	Escape of *Salmonella* from the damaged SCV without the recognition to the xenophagy pathway
$\boldsymbol{ti_{18}}$	
S16, S17, I1, A1, FmTORC1:ULK1c, Out	Regulation of mTORC1 by AA level
$\boldsymbol{ti_{19}}$	
SynAA, DegAA	Regulation of the AA level inside the cytosol

Table A5

Manatee invariants of the PN of the xenophagic capturing of *Salmonella*

Composition	Transitions
$\boldsymbol{mi_1}$	
$ti_1 + ti_{18} + ti_{19}$	Disr, Deg3, S13, S6, S5, S4, U3, S14, SynNS, SynNDP52, R15, R12, SynOPTN, F2, R23, S12, F6, R16, S11, R7, R8, R6, Synp62, Inv, SynLRSAM1, Cyt, SynE3ligase, S15, 2*SynTBK1, Norm, S16, S17, I1, A1, FmTORC1:ULK1c, Out, SynAA, DegAA
$\boldsymbol{mi_2}$	
$ti_2 + ti_{18} + ti_{19}$	Disr, Deg3i, S13, S6, S5, S4, U3, S14, SynNS, SynNDP52, R12, SynOPTN, F2, R22, R7, R8, R6, Synp62, Inv, SynLRSAM1, Cyt, SynE3ligase, S15, Norm, S16, S17, I1, A1, FmTORC1:ULK1c, Out, SynAA, DegAA
$\boldsymbol{mi_3}$	
$ti_3 + ti_{18} + ti_{19}$	Disr, R1, SynGal8, S13, S2, S3, S14, SynNS, SynNDP52, SynOPTN, U1, R3, R5, R4, Synp62, Inv, SynLRSAM1, SynE3ligase, S15, R9, S7, R19, Deg2i, F3, Norm, S16, S17, I1, A1, FmTORC1:ULK1c, Out, SynAA, DegAA

Composition	Transitions
$\boldsymbol{mi_4}$	
$ti_4 + ti_{18} + ti_{19}$	Disr, R1, F1, SynGal8, S1, S13, S2, S3, S14, SynNS, SynNDP52, SynOPTN, U1, R3, R5, R4, R11, Synp62, Inv, SynLRSAM1, SynE3ligase, S15, R19, Deg2i, Norm, S16, S17, I1, A1, FmTORC1:ULK1c, Out, SynAA, DegAA
$\boldsymbol{mi_5}$	
$ti_5 + ti_{18} + ti_{19}$	Disr, R1, F1, SynGal8, S1, S13, S2, S3, S14, SynNDP52, SynOPTN, U1, R3, R5, R4, Synp62, Inv, SynLRSAM1, S15, SynE3ligase, R20, Deg2ii, Norm, S16, S17, I1, A1, FmTORC1:ULK1c, Out, SynAA, DegAA
$\boldsymbol{mi_6}$	
$ti_6 + ti_{18} + ti_{19}$	Disr, R1, SynGal8, S13, S2, S3, S14, SynNS, SynNDP52, SynOPTN, U1, R3, R5, R4, R13, Deg2, R18, Synp62, Inv, SynLRSAM1, S9, R14, SynE3ligase, S15, S10, F5, 2*SynTBK1, R9, S7, F3, Norm, S16, S17, I1, A1, FmTORC1:ULK1c, Out, SynAA, DegAA
$\boldsymbol{mi_7}$	
$ti_7 + ti_{18} + ti_{19}$	Disr, Deg3, S13, S5, S4, U3, S14, SynNS, R15, SynNDP52, SynOPTN, R23, S12, F6, R16, S11, R7, R8, R6, Synp62, Inv, SynLRSAM1, Cyt, R10, SynE3ligase, S15, S8, 2*SynTBK1, F4, Norm, S16, S17, I1, A1, FmTORC1:ULK1c, Out, SynAA, DegAA
$\boldsymbol{mi_8}$	
$ti_8 + ti_{18} + ti_{19}$	Disr, R1, SynGal8, R2, S13, S2, S3, S14, SynNS, SynNDP52, SynOPTN, U2, R5, R4, Synp62, Inv, SynLRSAM1, SynE3ligase, S15, R9, S7, R19, Deg2i, F3, Norm, S16, S17, I1, A1, FmTORC1:ULK1c, Out, SynAA, DegAA
$\boldsymbol{mi_9}$	
$ti_9 + ti_{18} + ti_{19}$	Disr, S13, S6, S5, S4, U3, S14, SynNDP52, SynOPTN, F2, Deg3ii, R21, R7, R8, R6, Synp62, Inv, SynLRSAM1, Cyt, SynE3ligase, S15, Norm, S16, S17, I1, A1, FmTORC1:ULK1c, Out, SynAA, DegAA
$\boldsymbol{mi_{10}}$	
$ti_{10} + ti_{18} + ti_{19}$	Disr, Deg3i, S13, S5, S4, U3, S14, SynNS, SynNDP52, SynOPTN, R22, R7, R8, R6, Synp62, Inv, SynLRSAM1, R10, Cyt, SynE3ligase, S15, S8, F4, Norm, S16, S17, I1, A1, FmTORC1:ULK1c, Out, SynAA, DegAA
$\boldsymbol{mi_{11}}$	
$ti_{11} + ti_{18} + ti_{19}$	Disr, R1, F1, SynGal8, S1, R2, S13, S2, S3, S14, SynNS, SynNDP52, SynOPTN, U2, R5, R4, R11, Synp62, Inv, SynLRSAM1, SynE3ligase, S15, R19, Deg2i, Norm, S16, S17, I1, A1, FmTORC1:ULK1c, Out, SynAA, DegAA

Composition	Transitions
$\boldsymbol{mi_{12}}$	
$ti_{12} + ti_{18} + ti_{19}$	Disr, R1, F1, SynGal8, S1, R2, S13, S2, S3, S14, SynNDP52, SynOPTN, U2, R5, R4, Synp62, Inv, SynLRSAM1, S15, SynE3ligase, R20, Deg2ii, Norm, S16, S17, I1, A1, FmTORC1:ULK1c, Out, SynAA, DegAA
$\boldsymbol{mi_{13}}$	
$ti_{13} + ti_{18} + ti_{19}$	Disr, R17, R1, Deg1, SynGal8, R2, S13, S14, Inv, SynNDP52, S15, Norm, S16, S17, I1, A1, FmTORC1:ULK1c, Out, SynAA, DegAA
$\boldsymbol{mi_{14}}$	
$ti_{14} + ti_{18} + ti_{19}$	Disr, R1, F1, SynGal8, S1, R2, S13, S2, S3, S14, SynNS, SynNDP52, SynOPTN, U2, R5, R4, R11, R13, Deg2, R18, Synp62, Inv, SynLRSAM1, S9, SynE3ligase, R14, S15, S10, F5, 2*SynTBK1, Norm, S16, S17, I1, A1, FmTORC1:ULK1c, Out, SynAA, DegAA
$\boldsymbol{mi_{15}}$	
$ti_{15} + ti_{18} + ti_{19}$	Disr, R1, F1, SynGal8, S1, S13, S2, S3, S14, SynNS, SynNDP52, SynOPTN, U1, R3, R5, R4, R11, R13, Deg2, R18, Synp62, Inv, SynLRSAM1, S9, SynE3ligase, R14, S15, S10, F5, 2*SynTBK1, Norm, S16, S17, I1, A1, FmTORC1:ULK1c, Out, SynAA, DegAA
$\boldsymbol{mi_{16}}$	
$ti_{16} + ti_{18} + ti_{19}$	Disr, R1, SynGal8, R2, S13, S2, S3, S14, SynNS, SynNDP52, SynOPTN, U2, R5, R4, R13, Deg2, R18, Synp62, Inv, SynLRSAM1, S9, R14, SynE3ligase, S15, S10, F5, 2*SynTBK1, R9, S7, F3, Norm, S16, S17, I1, A1, FmTORC1:ULK1c, Out, SynAA, DegAA
$\boldsymbol{mi_{17}}$	
$ti_{17} + ti_{18} + ti_{19}$	Inv, Disr, S13, Norm, Esc, S16, S17, I1, A1, FmTORC1:ULK1c, Out, SynAA, DegAA
$\boldsymbol{mi_{18}}$	
$ti_{17} + ti_{19}$	Inv, Disr, S13, Norm, Esc, SynAA, DegAA
$\boldsymbol{mi_{19}}$	
ti_{19}	SynAA, DegAA

Table A6

Places of the SPN of a *Salmonella*-infected cell

Place	Description	M_0
MediumGen	Maximal possible number of bacteria to infect an individual cell	2000
SalMediumStart	Actual number of *Salmonella* in the medium to infect an individual cell	0
SalMedium	Adapted bacteria in the medium	0

Place	**Description**	M_0
WashIni	Signal for the one-time initiation of the washing process	1
WashCounter	Time counter of the washing process	0
WashSig	Signal for the onset of the washing process	0
SalSurface	Number of bacteria swimming on the cell surface	0
SalRuffle	Total number of bacteria located in ruffles	0
SalCyt	Total number of *Salmonella* with cytosolic access	0
SalVac	Total number of *Salmonella* inside SCV	0
DeathSigCyt	Signal that the cell undergoes cell death due to a high number of cytosolic *Salmonella*	0
DeathSigVac	Signal that the cell undergoes cell death due to a high number of vacuolar *Salmonella*	0
NrRuffle	Counter for the number of ruffle on the cell surface	0
CapSurface	Signal for the capability of the cell surface to accept additional *Salmonella*	1
SigCyt1	Signal for the presence of *Salmonella* in the cytosol	1
SigVac	Signal for the presence of *Salmonella* in the vacuole	1
AdaIniCyt	Signal for the initiation of the adaptability process of *Salmonella* in the cytosol	0
AdaIniVac	Signal for the initiation of the adaptability process of *Salmonella* in the SCV	0
CapCyt	Capacity of the cytosol	700
AdaCyt	Adaptability to the cytosol	0
DiviCyt	Divisibility of *Salmonella* in the cytosol	0
CapVac	Capacity of the SCV	150
AdaVac	Adaptability to the SCV	0
DiviVac	Divisibility of *Salmonella* in the SCV	0
Decision	Cell before the decision to become a cytosolic-capable or cytosolic-incapable cell	1
CellCyt	Cytosolic-capable cell	0
CellVac	Cytosolic-incapable cell	0
SigCyt2	Signal for the presence of *Salmonella* in the cytosol to initiate and terminate xenophagy	1
XenoIni	Signal for the initiation of xenophagy	0
XenoIniCounter	Time counter for the initiation of xenophagy	0
XenoEnd	Signal for the termination of xenophagy	0
XenoEndCounter	Time counter for the termination of xenophagy	0
XenoSig	Signal for xenophagic capturing and degradation	0

Table A7

Transitions of the SPN of a *Salmonella*-infected cell

Transition	Description	c [1/sec]
remove	Removes one *Salmonella* from the infection medium	Depending on the MOI, see Table 4.3
add	Adds one *Salmonella* to the infection medium	Depending on the MOI, see Table 4.3
wash_count	Increases the time counter of the washing process, i.e., place *WashCounter*	Depending on the incubation time, see Table 4.4
wash_start	Generates the signal for the onset of the washing process	1000
washing1	Washing to remove non-invasive *Salmonella* in the medium	1000
washing2	Washing to remove non-invasive *Salmonella* in the medium	1000
washing3	Washing to remove non-invasive *Salmonella* on the cell surface	1000
firstlanding	First landing of *Salmonella* on the cell surface	0.0019
landing	Landing of adapted *Salmonella* on the cell surface	0.00384
take_off	Take off of *Salmonella* from the cell surface	0.67
initiation	formation of a new ruffle on the cell surface	0.0005
joining	*Salmonella* swims and docks to a preexisting ruffle	0.005
cap_reached	Capacity of the surface is reached, no further ruffle can be initiated or bacteria can join	1000
enter_cyt	*Salmonella* enters the cytosol	0.004
stay_vac	*Salmonella* stays in the SCV	0.006
adasig_cyt	Signal that *Salmonella* is inside the cytosol to induce the adaptability to the cytosol	1000
adasig_vac	Signal that *Salmonella* is inside the vacuole to induce the adaptability to the vacuole	1000
ada_cyt	Increases the adaptability of *Salmonella* to the cytosol	0.167
ada_vac	Increases the adaptability of *Salmonella* to the SCV	0.036
pro_cyt	Proliferation of *Salmonella* inside the cytosol	0.000000595
pro_vac	Proliferation of *Salmonella* inside the vacuole	0.000000411
divi_cyt	Increases the divisibility of *Salmonella* in the cytosol	1000
divi_vac	Increases the divisibility of *Salmonella* inside the SCV	1000
death_cyt1	Cell undergoes cell death due to a high number of cytosolic *Salmonella*	1000
death_cyt2	Removal of cytosolic *Salmonella* in cells that undergo cell death	1000
death_vac1	Cell undergoes cell death due to a high number of vacuolar *Salmonella*	1000
death_vac2	Removes vacuolar *Salmonella* in cells that undergo cell death	1000
death1	Removes vacuolar *Salmonella* in cells that undergo cell death, due to a high number of cytosolic bacteria	1000

Transition	**Description**	**c [1/sec]**
death2	Removes cytosolic *Salmonella* in cells that undergo cell death, due to a high number of vacuolar bacteria	1000
cell_cyt	Cell gets cytosolic-capable	350
cell_vac	Cell gets cytosolic-incapable	650
xeno_sig	Induces signals for the initiation and termination of xenophagy	1000
xeno_ini_count	Increases the time counter of the initiation of xenophagy, i.e., place *XenoIniCounter*	0.56
xeno_ini	Initiation of xenophagy	1000
xeno_end_count	Increases the time counter of the termination of xenophagy, i.e., place *XenoEndCounter*	0.069
xeno_end	Termination of xenophagy	1000
xeno_deg	Removes one bacterium from the cytosol via xenophagy	0.00037

Bibliography

[1] M. E. Ohl and S. I. Miller, "*Salmonella*: a model for bacterial pathogenesis," *Annual Review of Medicine*, vol. 52, pp. 259–274, 2001.

[2] P. Garai, D. P. Gnanadhas, and D. Chakravortty, "*Salmonella enterica* serovars Typhimurium and Typhi as model organisms: revealing paradigm of host-pathogen interactions," *Virulence*, vol. 3, no. 4, pp. 377–388, 2012.

[3] D. J. Vugia, M. Samuel, M. M. Farley, R. Marcus, B. Shiferaw, S. Shallow, K. Smith, F. J. Angulo, and E. I. P. F. W. Group, "Invasive *Salmonella* infections in the United States, FoodNet, 1996-1999: incidence, serotype distribution, and outcome," *Clinical InfectiousDiseases*, vol. 38, no. 3, pp. 149–156, 2004.

[4] L. A. Lee, N. D. Puhr, E. K. Maloney, N. H. Bean, and R. V. Tauxe, "Increase in antimicrobial-resistant *Salmonella* infections in the United States, 1989-1990," *The Journal of Infectious Diseases*, vol. 170, no. 1, pp. 128–134, 1994.

[5] S. Kariuki, M. A. Gordon, N. Feasey, and C. M. Parry, "Antimicrobial resistance and management of invasive *Salmonella* disease," *Vaccine*, vol. 33, pp. C21–C29, 2015.

[6] *WHO estimates of the global burden of foodborne diseases: foodborne disease burden epidemiology reference group 2007-2015*. World Health Organization, 2015.

[7] S. E. Majowicz, J. Musto, E. Scallan, F. J. Angulo, M. Kirk, S. J. O'Brien, T. F. Jones, A. Fazil, and R. M. Hoekstra, "The global bur-

den of nontyphoidal *Salmonella* gastroenteritis," *Clinical Infectious Diseases*, vol. 50, no. 6, pp. 882–889, 2010.

[8] B. B. Finlay, S. Ruschkowski, and S. Dedhar, "Cytoskeletal rearrangements accompanying *Salmonella* entry into epithelial cells," *Journal of Cell Science*, vol. 99, pp. 283–296, 1991.

[9] F. García-del Portillo and B. B. Finlay, "Targeting of *Salmonella* Typhimurium to vesicles containing lysosomal membrane glycoproteins bypasses compartments with mannose 6-phosphate receptors," *The Journal of Cell Biology*, vol. 129, no. 1, pp. 81–97, 1995.

[10] C. R. Beuzón, S. Méresse, K. E. Unsworth, J. Ruíz-Albert, S. Garvis, S. R. Waterman, T. A. Ryder, E. Boucrot, and D. W. Holden, "*Salmonella* maintains the integrity of its intracellular vacuole through the action of SifA," *The EMBO Journal*, vol. 19, no. 13, pp. 3235–3249, 2000.

[11] J. H. Brumell, P. Tang, M. L. Zaharik, and B. B. Finlay, "Disruption of the *Salmonella*-containing vacuole leads to increased replication of *Salmonella enterica* serovar Typhimurium in the cytosol of epithelial cells," *Infection and Immunity*, vol. 70, no. 6, pp. 3264–3270, 2002.

[12] A. J. Perrin, X. Jiang, C. L. Birmingham, N. S. So, and J. H. Brumell, "Recognition of bacteria in the cytosol of mammalian cells by the ubiquitin system," *Current Biology*, vol. 14, no. 9, pp. 806–811, 2004.

[13] D. Roy, D. R. Liston, V. J. Idone, A. Di, D. J. Nelson, C. Pujol, J. B. Bliska, S. Chakrabarti, and N. W. Andrews, "A process for controlling intracellular bacterial infections induced by membrane injury," *Science*, vol. 304, no. 5676, pp. 1515–1518, 2004.

[14] L. A. Knodler, B. A. Vallance, J. Celli, S. Winfree, B. Hansen, M. Montero, and O. Steele-Mortimer, "Dissemination of invasive *Salmonella* via bacterial-induced extrusion of mucosal epithelia," *Proceedings of the National Academy of Sciences*, vol. 107, no. 41, pp. 17733–17738, 2010.

[15] C. R. Beuzón, S. P. Salcedo, and D. W. Holden, "Growth and killing of a *Salmonella enterica* serovar Typhimurium *sifA* mutant strain in the cytosol of different host cell lines," *Microbiology*, vol. 148, no. 9, pp. 2705–2715, 2002.

[16] P. Malik-Kale, S. Winfree, and O. Steele-Mortimer, "The bimodal lifestyle of intracellular *Salmonella* in epithelial cells: replication in the cytosol obscures defects in vacuolar replication," *PLoS ONE*, vol. 7, no. 6, p. e38732, 2012.

[17] L. A. Knodler, V. Nair, and O. Steele-Mortimer, "Quantitative assessment of cytosolic *Salmonella* in epithelial cells," *PLoS ONE*, vol. 9, no. 1, p. e84681, 2014.

[18] B. Coburn, G. A. Grassl, and B. B. Finlay, "*Salmonella*, the host and disease: a brief review," *Immunology and Cell Biology*, vol. 85, no. 2, pp. 112–118, 2007.

[19] H. K. de Jong, C. M. Parry, T. van der Poll, and W. J. Wiersinga, "Host-pathogen interaction in invasive Salmonellosis," *PLoS Pathogens*, vol. 8, no. 10, p. e1002933, 2012.

[20] A. Orvedahl and B. Levine, "Eating the enemy within: autophagy in infectious diseases," *Cell Death & Differentiation*, vol. 16, pp. 57–69, 2009.

[21] L. A. Knodler and J. Celli, "Eating the strangers within: host control of intracellular bacteria via xenophagy," *Cellular Microbiology*, vol. 13, no. 9, pp. 1319–1327, 2011.

[22] E.-K. Jo, J.-M. Yuk, D.-M. Shin, and C. Sasakawa, "Roles of autophagy in elimination of intracellular bacterial pathogens," *Frontiers in Immunology*, vol. 4, p. 97, 2013.

[23] L. C. Gomes and I. Dikic, "Autophagy in antimicrobial immunity," *Molecular Cell*, vol. 54, no. 2, pp. 224–233, 2014.

[24] J. Huang and J. H. Brumell, "Bacteria-autophagy interplay: a battle for survival," *Nature Reviews Microbiology*, vol. 12, pp. 101–114, 2014.

[25] S. Shaid, C. Brandts, H. Serve, and I. Dikic, "Ubiquitination and selective autophagy," *Cell Death & Differentiation*, vol. 20, pp. 21–30, 2013.

[26] A. Stolz, A. Ernst, and I. Dikic, "Cargo recognition and trafficking in selective autophagy," *Nature Cell Biology*, vol. 16, pp. 495–501, 2014.

[27] A. Khaminets, C. Behl, and I. Dikic, "Ubiquitin-dependent and independent signals in selective autophagy," *Trends in Cell Biology*, vol. 26, no. 1, pp. 6–16, 2016.

[28] Z. Xie and D. J. Klionsky, "Autophagosome formation: core machinery and adaptations," *Nature Cell Biology*, vol. 9, pp. 1102–1109, 2007.

[29] Y. T. Zheng, S. Shahnazari, A. Brech, T. Lamark, T. Johansen, and J. H. Brumell, "The adaptor protein p62/SQSTM1 targets invading bacteria to the autophagy pathway," *The Journal of Immunology*, vol. 183, no. 9, pp. 5909–5916, 2009.

[30] P. Wild, H. Farhan, D. G. McEwan, S. Wagner, V. V. Rogov, N. R. Brady, B. Richter, J. Korac, O. Waidmann, C. Choudhary, *et al.*, "Phosphorylation of the autophagy receptor optineurin restricts *Salmonella* growth," *Science*, vol. 333, no. 6039, pp. 228–233, 2011.

[31] T. L. Thurston, G. Ryzhakov, S. Bloor, N. von Muhlinen, and F. Randow, "The TBK1 adaptor and autophagy receptor NDP52 restricts the proliferation of ubiquitin-coated bacteria," *Nature Immunology*, vol. 10, pp. 1215–1221, 2009.

[32] C. Grabbe, K. Husnjak, and I. Dikic, "The spatial and temporal organization of ubiquitin networks," *Nature Reviews Molecular Cell Biology*, vol. 12, pp. 295–307, 2011.

[33] M. Akutsu, I. Dikic, and A. Bremm, "Ubiquitin chain diversity at a glance," *Journal of Cell Science*, vol. 129, pp. 875–880, 2016.

[34] C. L. Birmingham, A. C. Smith, M. A. Bakowski, T. Yoshimori, and J. H. Brumell, "Autophagy controls *Salmonella* infection in response

to damage to the *Salmonella*-containing vacuole," *Journal of Biological Chemistry*, vol. 281, pp. 11374–11383, 2006.

[35] J. L. Benjamin, R. Sumpter, B. Levine, and L. V. Hooper, "Intestinal epithelial autophagy is essential for host defense against invasive bacteria," *Cell Host & Microbe*, vol. 13, no. 6, pp. 723–734, 2013.

[36] T. L. Thurston, M. P. Wandel, N. von Muhlinen, Á. Foeglein, and F. Randow, "Galectin 8 targets damaged vesicles for autophagy to defend cells against bacterial invasion," *Nature*, vol. 482, pp. 414–418, 2012.

[37] I. Nakagawa, A. Amano, N. Mizushima, A. Yamamoto, H. Yamaguchi, T. Kamimoto, A. Nara, J. Funao, M. Nakata, K. Tsuda, *et al.*, "Autophagy defends cells against invading group A *Streptococcus*," *Science*, vol. 306, no. 5698, pp. 1037–1040, 2004.

[38] M. G. Gutierrez, S. S. Master, S. B. Singh, G. A. Taylor, M. I. Colombo, and V. Deretic, "Autophagy is a defense mechanism inhibiting BCG and *Mycobacterium tuberculosis* survival in infected macrophages," *Cell*, vol. 119, no. 6, pp. 753–766, 2004.

[39] H. Kitano, "Computational systems biology," *Nature*, vol. 420, pp. 206–210, 2002.

[40] B. Schoeberl, C. Eichler-Jonsson, E. D. Gilles, and G. Müller, "Computational modeling of the dynamics of the MAP kinase cascade activated by surface and internalized EGF receptors," *Nature Biotechnology*, vol. 20, pp. 370–375, 2002.

[41] H. M. Sauro and B. N. Kholodenko, "Quantitative analysis of signaling networks," *Progress in Biophysics and Molecular Biology*, vol. 86, no. 1, pp. 5–43, 2004.

[42] Z.-R. Zhang, J. S. Bonifacino, and R. S. Hegde, "Deubiquitinases sharpen substrate discrimination during membrane protein degradation from the ER," *Cell*, vol. 154, no. 3, pp. 609–622, 2013.

[43] I. Koch, W. Reisig, and F. Schreiber, *Modeling in systems biology: the Petri net approach*, vol. 16. Springer, 2011.

[44] T. Murata, "Petri nets: properties, analysis and applications," vol. 77, pp. 541–580, IEEE, 1989.

[45] S. Schuster and C. Hilgetag, "On elementary flux modes in biochemical reaction systems at steady state," *Journal of Biological Systems*, vol. 2, no. 2, pp. 165–182, 1994.

[46] R. Alur, C. Belta, F. Ivančić, V. Kumar, M. Mintz, G. J. Pappas, H. Rubin, and J. Schug, "Hybrid modeling and simulation of biomolecular networks," in *International Workshop on Hybrid Systems: Computation and Control*, pp. 19–32, Springer, 2001.

[47] V. N. Reddy, M. L. Mavrovouniotis, and M. N. Liebman, "Petri net representations in metabolic pathways," in *ISMB*, vol. 93, pp. 328–336, 1993.

[48] R. Hofestädt, "A Petri net application to model metabolic processes," *Systems Analysis Modelling Simulation*, vol. 16, no. 2, pp. 113–122, 1994.

[49] H. Genrich, R. Küffner, and K. Voss, "Executable Petri net models for the analysis of metabolic pathways," *International Journal on Software Tools for Technology Transfer (STTT)*, vol. 3, no. 4, pp. 394–404, 2001.

[50] I. Koch, B. H. Junker, and M. Heiner, "Application of Petri net theory for modelling and validation of the sucrose breakdown pathway in the potato tuber," *Bioinformatics*, vol. 21, no. 7, pp. 1219–1226, 2005.

[51] G. Minervini, E. Panizzoni, M. Giollo, A. Masiero, C. Ferrari, and S. C. Tosatto, "Design and analysis of a Petri net model of the Von Hippel-Lindau (VHL) tumor suppressor interaction network," *PLoS ONE*, vol. 9, no. 6, p. e96986, 2014.

[52] K. Voss, M. Heiner, and I. Koch, "Steady state analysis of metabolic pathways using Petri nets," *In Silico Biology*, vol. 3, no. 3, pp. 367–387, 2003.

[53] J. S. Oliveira, C. G. Bailey, J. B. Jones-Oliveira, D. A. Dixon, D. W. Gull, and M. L. Chandler, "A computational model for the identification of biochemical pathways in the Krebs cycle," *Journal of Computational Biology*, vol. 10, no. 1, pp. 57–82, 2004.

[54] A. Sackmann, M. Heiner, and I. Koch, "Application of Petri net based analysis techniques to signal transduction pathways," *BMC Bioinformatics*, vol. 7, no. 482, pp. 1–17, 2006.

[55] S. Hardy and P. N. Robillard, "Petri net-based method for the analysis of the dynamics of signal propagation in signaling pathways," *Bioinformatics*, vol. 24, no. 2, pp. 209–217, 2007.

[56] J. Scheidel, K. Lindauer, J. Ackermann, and I. Koch, "Quasi-steady-state analysis based on structural modules and timed Petri net predict system's dynamics: the life cycle of the insulin receptor," *Metabolites*, vol. 5, no. 4, pp. 766–793, 2015.

[57] J. Scheidel, L. Amstein, J. Ackermann, I. Dikic, and I. Koch, "*In silico* knockout studies of xenophagic capturing of *Salmonella*," *PLoS Computational Biology*, vol. 12, no. 12, p. e1005200, 2016.

[58] D.-Y. Lee, R. Zimmer, S.-Y. Lee, D. Hanisch, and S. Park, "Knowledge representation model for systems-level analysis of signal transduction networks," *Genome Informatics*, vol. 15, no. 2, pp. 234–243, 2004.

[59] S. Grunwald, A. Speer, J. Ackermann, and I. Koch, "Petri net modelling of gene regulation of the Duchenne muscular dystrophy," *BioSystems*, vol. 92, no. 2, pp. 189–205, 2008.

[60] W. Marwan, A. Sujatha, and C. Starostzik, "Reconstructing the regulatory network controlling commitment and sporulation in *Physarum polycephalum* based on hierarchical Petri net modelling and simula-

tion," *Journal of Theoretical Biology*, vol. 236, no. 4, pp. 349–365, 2005.

[61] T. Dandekar, F. Astrid, P. Jasmin, and M. Hensel, "*Salmonella enterica*: a surprisingly well-adapted intracellular lifestyle," *Frontiers in Microbiology*, vol. 3, no. 164, pp. 1–11, 2012.

[62] I. Thiele, D. R. Hyduke, B. Steeb, G. Fankam, D. K. Allen, S. Bazzani, P. Charusanti, F.-C. Chen, R. M. Fleming, C. A. Hsiung, *et al.*, "A community effort towards a knowledge-base and mathematical model of the human pathogen *Salmonella* Typhimurium LT2," *BMC Systems Biology*, vol. 5, no. 8, pp. 1–9, 2011.

[63] E. Fiskin, T. Bionda, I. Dikic, and C. Behrends, "Global analysis of host and bacterial ubiquitinome in response to *Salmonella* Typhimurium infection," *Molecular Cell*, vol. 62, no. 6, pp. 967–981, 2016.

[64] P. K. Dhal, R. K. Barman, S. Saha, and S. Das, "Dynamic modularity of host protein interaction networks in *Salmonella* Typhi infection," *PLoS One*, vol. 9, no. 8, p. e104911, 2014.

[65] The Gene Ontology Consortium, "Expansion of the Gene Ontology knowledgebase and resources," *Nucleic Acids Research*, vol. 45, no. D1, pp. D331–D338, 2016.

[66] C. Das, A. Dutta, H. Rajasingh, and S. S. Mande, "Understanding the sequential activation of Type III and Type VI Secretion Systems in *Salmonella* Typhimurium using Boolean modeling," *Gut Pathogens*, vol. 5, no. 28, pp. 1–12, 2013.

[67] R. W. Kasinskas and N. S. Forbes, "*Salmonella* Typhimurium specifically chemotax and proliferate in heterogeneous tumor tissue in vitro," *Biotechnology and Bioengineering*, vol. 94, no. 4, pp. 710–721, 2006.

[68] S. P. Brown, S. J. Cornell, M. Sheppard, A. J. Grant, D. J. Maskell, B. T. Grenfell, and P. Mastroeni, "Intracellular demography and the

dynamics of *Salmonella enterica* infections," *PLoS Biology*, vol. 4, no. 11, p. e349, 2006.

[69] A. J. Grant, O. Restif, T. J. McKinley, M. Sheppard, D. J. Maskell, and P. Mastroeni, "Modelling within-host spatiotemporal dynamics of invasive bacterial disease," *PLoS Biology*, vol. 6, no. 4, p. e74, 2008.

[70] R. Ivanek, E. L. Snary, A. J. Cook, and Y. T. Groehn, "A mathematical model for the transmission of *Salmonella* Typhimurium within a grower-finisher pig herd in Great Britain," *Journal of Food Protection*, vol. 67, no. 11, pp. 2403–2409, 2004.

[71] V. K. Juneja, M. V. Melendres, L. Huang, J. Subbiah, and H. Thippareddi, "Mathematical modeling of growth of *Salmonella* in raw ground beef under isothermal conditions from 10 to 45 C," *International Journal of Food Microbiology*, vol. 131, no. 2, pp. 106–111, 2009.

[72] P. R. Velugoti, L. K. Bohra, V. K. Juneja, L. Huang, A. L. Wesseling, J. Subbiah, and H. Thippareddi, "Dynamic model for predicting growth of *Salmonella* spp. in ground sterile pork," *Food Microbiology*, vol. 28, no. 4, pp. 796–803, 2011.

[73] S. Andrés, L. Giannuzzi, and N. Zaritzky, "Mathematical modeling of microbial growth in packaged refrigerated orange juice treated with chemical preservatives," *Journal of Food Science*, vol. 66, no. 5, pp. 724–728, 2001.

[74] W. Pan and D. W. Schaffner, "Modeling the growth of *Salmonella* in cut red round tomatoes as a function of temperature," *Journal of Food Protection*, vol. 73, no. 8, pp. 1502–1505, 2010.

[75] T. McMeekin, J. Olley, D. Ratkowsky, and T. Ross, "Predictive microbiology: towards the interface and beyond," *International Journal of Food Microbiology*, vol. 73, no. 2, pp. 395–407, 2002.

[76] K. McDonald and D.-W. Sun, "Predictive food microbiology for the meat industry: a review," *International Journal of Food Microbiology*, vol. 52, no. 1, pp. 1–27, 1999.

[77] B. Misselwitz, N. Barrett, S. Kreibich, P. Vonaesch, D. Andritschke, S. Rout, K. Weidner, M. Sormaz, P. Songhet, P. Horvath, *et al.*, "Near surface swimming of *Salmonella* Typhimurium explains target-site selection and cooperative invasion," *PLoS Pathogens*, vol. 8, no. 7, p. e1002810, 2012.

[78] T. Dunn, "Image segmentation and modelling of host-pathogen dynamics of *Salmonella*," *Master thesis*, 2016.

[79] B. Misselwitz, S. Dilling, P. Vonaesch, R. Sacher, B. Snijder, M. Schlumberger, S. Rout, M. Stark, C. Von Mering, L. Pelkmans, *et al.*, "RNAi screen of *Salmonella* invasion shows role of COPI in membrane targeting of cholesterol and Cdc42," *Molecular Systems Biology*, vol. 7, no. 474, pp. 1–19, 2011.

[80] A. C. Y. Ng, "Integrative systems biology and networks in autophagy," in *Seminars in Immunopathology*, vol. 32, pp. 355–361, Springer, 2010.

[81] C. Behrends, M. E. Sowa, S. P. Gygi, and J. W. Harper, "Network organization of the human autophagy system," *Nature*, vol. 466, pp. 68–76, 2010.

[82] M. H. Kramer, J.-C. Farre, K. Mitra, M. K. Yu, K. Ono, B. Demchak, K. Licon, M. Flagg, R. Balakrishnan, J. M. Cherry, *et al.*, "Active interaction mapping reveals the hierarchical organization of autophagy," *Molecular Cell*, vol. 65, no. 4, pp. 761–774, 2017.

[83] Z. Yao, J. Petschnigg, R. Ketteler, and I. Stagljar, "Application guide for omics approaches to cell signaling," *Nature Chemical Biology*, vol. 11, pp. 387–397, 2015.

[84] J. Einloft, J. Ackermann, J. Nöthen, and I. Koch, "MonaLisa – visualization and analysis of functional modules in biochemical networks," *Bioinformatics*, vol. 29, no. 11, pp. 1469–1470, 2013.

[85] D. Formanowicz, M. Radom, P. Zawierucha, and P. Formanowicz, "Petri net-based approach to modeling and analysis of selected aspects

of the molecular regulation of angiogenesis," *PLoS ONE*, vol. 12, no. 3, p. e0173020, 2017.

[86] S. Schuster, T. Dandekar, and D. A. Fell, "Detection of elementary flux modes in biochemical networks: a promising tool for pathway analysis and metabolic engineering," *Trends in Biotechnology*, vol. 17, no. 2, pp. 53–60, 1999.

[87] S. Schuster, D. A. Fell, and T. Dandekar, "A general definition of metabolic pathways useful for systematic organization and analysis of complex metabolic networks," *Nature Biotechnology*, vol. 18, pp. 326–332, 2000.

[88] C. H. Schilling, D. Letscher, and B. Ø. Palsson, "Theory for the systemic definition of metabolic pathways and their use in interpreting metabolic function from a pathway-oriented perspective," *Journal of Theoretical Biology*, vol. 203, no. 3, pp. 229–248, 2000.

[89] I. Zevedei-Oancea and S. Schuster, "Topological analysis of metabolic networks based on Petri net theory," *In Silico Biology*, vol. 3, no. 3, pp. 323–345, 2003.

[90] S. Schuster, C. Hilgetag, J. H. Woods, and D. A. Fell, "Reaction routes in biochemical reaction systems: algebraic properties, validated calculation procedure and example from nucleotide metabolism," *Journal of Mathematical Biology*, vol. 45, no. 2, pp. 153–181, 2002.

[91] S. Schuster, T. Pfeiffer, F. Moldenhauer, I. Koch, and T. Dandekar, "Exploring the pathway structure of metabolism: decomposition into subnetworks and application to *Mycoplasma pneumoniae*," *Bioinformatics*, vol. 18, no. 2, pp. 351–361, 2002.

[92] S. Klamt and J. Stelling, "Two approaches for metabolic pathway analysis?," *Trends in Biotechnology*, vol. 21, no. 2, pp. 64–69, 2003.

[93] B. Ø. Palsson, N. D. Price, and J. A. Papin, "Development of network-based pathway definitions: the need to analyze real metabolic networks," *Trends in Biotechnology*, vol. 21, no. 5, pp. 195–198, 2003.

[94] T. Çakır, B. Kırdar, Z. Önsan, K. Ö. Ülgen, and J. Nielsen, "Effect of carbon source perturbations on transcriptional regulation of metabolic fluxes in *Saccharomyces cerevisiae*," *BMC Systems Biology*, vol. 1, no. 18, pp. 1–10, 2007.

[95] J. I. Kim, J. D. Varner, and D. Ramkrishna, "A hybrid model of anaerobic *E. coli* GJT001: combination of elementary flux modes and cybernetic variables," *Biotechnology Progress*, vol. 24, no. 5, pp. 993–1006, 2008.

[96] S. J. Jol, A. Kümmel, M. Terzer, J. Stelling, and M. Heinemann, "System-level insights into yeast metabolism by thermodynamic analysis of elementary flux modes," *PLoS Computational Biology*, vol. 8, no. 3, p. e1002415, 2012.

[97] S. J. Wiback and B. Ø. Palsson, "Extreme pathway analysis of human red blood cell metabolism," *Biophysical Journal*, vol. 83, no. 2, pp. 808–818, 2002.

[98] N. D. Price, J. A. Papin, and B. Ø. Palsson, "Determination of redundancy and systems properties of the metabolic network of *Helicobacter pylori* using genome-scale extreme pathway analysis," *Genome Research*, vol. 12, pp. 760–769, 2002.

[99] I. Koch, J. Nöthen, and E. Schleiff, "Modeling the metabolism of *Arabidopsis thaliana*: Application of network decomposition and network reduction in the context of Petri nets," *Frontiers in Genetics*, vol. 8, no. 85, pp. 1–22, 2017.

[100] T. Wilhelm, J. Behre, and S. Schuster, "Analysis of structural robustness of metabolic networks," *Systems Biology*, vol. 1, no. 1, pp. 114–120, 2004.

[101] J. Stelling, S. Klamt, K. Bettenbrock, S. Schuster, and E. D. Gilles, "Metabolic network structure determines key aspects of functionality and regulation," *Nature*, vol. 420, pp. 190–193, 2002.

[102] T. Çakır, B. Kırdar, and K. Ö. Ülgen, "Metabolic pathway analysis of yeast strengthens the bridge between transcriptomics and metabolic networks," *Biotechnology and Bioengineering*, vol. 86, no. 3, pp. 251–260, 2004.

[103] J. Behre, T. Wilhelm, A. von Kamp, E. Ruppin, and S. Schuster, "Structural robustness of metabolic networks with respect to multiple knockouts," *Journal of Theoretical Biology*, vol. 252, no. 3, pp. 433–441, 2008.

[104] Y. Min, X. Jin, M. Chen, Z. Pan, Y. Ge, and J. Chang, "Pathway knockout and redundancy in metabolic networks," *Journal of Theoretical Biology*, vol. 270, no. 1, pp. 63–69, 2011.

[105] C.-M. Ghim, K.-I. Goh, and B. Kahng, "Lethality and synthetic lethality in the genome-wide metabolic network of *Escherichia coli*," *Journal of Theoretical Biology*, vol. 237, no. 4, pp. 401–411, 2005.

[106] D. Deutscher, I. Meilijson, M. Kupiec, and E. Ruppin, "Multiple knockout analysis of genetic robustness in the yeast metabolic network," *Nature Genetics*, vol. 38, pp. 993–998, 2006.

[107] S. Klamt and E. D. Gilles, "Minimal cut sets in biochemical reaction networks," *Bioinformatics*, vol. 20, no. 2, pp. 226–234, 2004.

[108] S. Klamt, J. Saez-Rodriguez, J. A. Lindquist, L. Simeoni, and E. D. Gilles, "A methodology for the structural and functional analysis of signaling and regulatory networks," *BMC Bioinformatics*, vol. 7, no. 56, pp. 1–26, 2006.

[109] S. N. Steinway, M. B. Biggs, T. P. Loughran Jr, J. A. Papin, and R. Albert, "Inference of network dynamics and metabolic interactions in the gut microbiome," *PLoS Computational Biology*, vol. 11, no. 6, p. e1004338, 2015.

[110] A. Saadatpour, R.-S. Wang, A. Liao, X. Liu, T. P. Loughran, I. Albert, and R. Albert, "Dynamical and structural analysis of a T cell survival

network identifies novel candidate therapeutic targets for large granular lymphocyte leukemia," *PLoS Computational Biology*, vol. 7, no. 11, p. e1002267, 2011.

[111] M. K. Padwal, U. Sarma, and B. Saha, "Comprehensive logic based analyses of Toll-like receptor 4 signal transduction pathway," *PLoS ONE*, vol. 9, no. 4, p. e92481, 2014.

[112] A. Naldi, D. Berenguier, A. Fauré, F. Lopez, D. Thieffry, and C. Chaouiya, "Logical modelling of regulatory networks with GINsim 2.3," *BioSystems*, vol. 97, no. 2, pp. 134–139, 2009.

[113] C. Müssel, M. Hopfensitz, and H. A. Kestler, "BoolNet – an R package for generation, reconstruction and analysis of Boolean networks," *Bioinformatics*, vol. 26, no. 10, pp. 1378–1380, 2010.

[114] R. Samaga and S. Klamt, "Modeling approaches for qualitative and semi-quantitative analysis of cellular signaling networks," *Cell Communication and Signaling*, vol. 11, no. 43, 2013.

[115] S. Klamt, J. Saez-Rodriguez, and E. D. Gilles, "Structural and functional analysis of cellular networks with CellNetAnalyzer," *BMC Systems Biology*, vol. 1, no. 2, pp. 1–13, 2007.

[116] J. Saez-Rodriguez, L. Simeoni, J. A. Lindquist, R. Hemenway, U. Bommhardt, B. Arndt, U.-U. Haus, R. Weismantel, E. D. Gilles, S. Klamt, *et al.*, "A logical model provides insights into T cell receptor signaling," *PLoS Computational Biology*, vol. 3, no. 8, p. e163, 2007.

[117] R. Samaga, J. Saez-Rodriguez, L. G. Alexopoulos, P. K. Sorger, and S. Klamt, "The logic of EGFR/ErbB signaling: theoretical properties and analysis of high-throughput data," *PLoS Computational Biology*, vol. 5, no. 8, p. e1000438, 2009.

[118] T. Ideker, V. Thorsson, J. A. Ranish, R. Christmas, J. Buhler, J. K. Eng, R. Bumgarner, D. R. Goodlett, R. Aebersold, and L. Hood, "Integrated genomic and proteomic analyses of a systematically per-

turbed metabolic network," *Science*, vol. 292, no. 5518, pp. 929–934, 2001.

[119] I. S. Peter and E. H. Davidson, "A gene regulatory network controlling the embryonic specification of endoderm," *Nature*, vol. 474, pp. 635–639, 2011.

[120] E. J. Molinelli, A. Korkut, W. Wang, M. L. Miller, N. P. Gauthier, X. Jing, P. Kaushik, Q. He, G. Mills, D. B. Solit, *et al.*, "Perturbation biology: inferring signaling networks in cellular systems," *PLoS Computational Biology*, vol. 9, no. 12, p. e1003290, 2013.

[121] K. Sachs, O. Perez, D. Pe'er, D. A. Lauffenburger, and G. P. Nolan, "Causal protein-signaling networks derived from multiparameter single-cell data," *Science*, vol. 308, no. 5721, pp. 523–529, 2005.

[122] R. Albert, "Network inference, analysis, and modeling in systems biology," *The Plant Cell Online*, vol. 19, pp. 3327–3338, 2007.

[123] F. Markowetz and R. Spang, "Inferring cellular networks – a review," *BMC Bioinformatics*, vol. 8, no. 6, pp. 1–17, 2007.

[124] V. Chandrasekaran, N. Srebro, and P. Harsha, "Complexity of inference in graphical models," in *Proceedings of the Twenty-Fourth Conference on Uncertainty in Artificial Intelligence*, pp. 70–78, AUAI Press, 2008.

[125] P. H. Starke, *Analyse von Petri-Netz-Modellen.* Springer, 1990.

[126] W. Reisig, *Petri nets: an introduction.* Springer, 1985.

[127] D. J. Wilkinson, *Stochastic modelling for systems biology, Second Edition.* CRC press, 2011.

[128] B. P. Ingalls, *Mathematical modeling in systems biology: an introduction.* MIT press, 2013.

[129] C. A. Petri, *Kommunikation mit Automaten.* PhD thesis, Technische Hochschule Darmstadt, 1962.

[130] K. Lautenbach, "Exakte Bedingungen der Lebendigkeit für eine Klasse von Petri-Netzen," *Berichte der Gesellschaft für Mathematik und Datenverarbeitung*, vol. 82, 1973.

[131] I. Koch and J. Ackermann, "On functional module detection in metabolic networks," *Metabolites*, vol. 3, no. 3, pp. 673–700, 2013.

[132] R. Lipton, "The reachability problem requires exponential space," *Research Report 62. Department of Computer Science, Yale University*, 1976.

[133] J. Esparza, "Decidability and complexity of Petri net problems – an introduction," *Lectures on Petri nets I: Basic Models*, pp. 374–428, 1998.

[134] C. Chaouiya, "Petri net modelling of biological networks," *Briefings in Bioinformatics*, vol. 8, no. 4, pp. 210–219, 2007.

[135] J. Behre and S. Schuster, "Modeling signal transduction in enzyme cascades with the concept of elementary flux modes," *Journal of Computational Biology*, vol. 16, no. 6, pp. 829–844, 2009.

[136] L. Michaelis and M. L. Menten, "Die Kinetik der Invertinwirkung," *Biochemische Zeitschrift*, vol. 49, pp. 333–369, 1913.

[137] D. T. Gillespie, "A general method for numerically simulating the stochastic time evolution of coupled chemical reactions," *Journal of Computational Physics*, vol. 22, no. 4, pp. 403–434, 1976.

[138] D. T. Gillespie, "Exact stochastic simulation of coupled chemical reactions," *The Journal of Physical Chemistry*, vol. 81, no. 25, pp. 2340–2361, 1977.

[139] M. Kanehisa and S. Goto, "KEGG: Kyoto encyclopedia of genes and genomes," *Nucleic Acids Research*, vol. 28, no. 1, pp. 27–30, 2000.

[140] N. Juty, R. Ali, M. Glont, S. Keating, N. Rodriguez, M. Swat, S. Wimalaratne, H. Hermjakob, N. Le Novère, C. Laibe, *et al.*,

"BioModels: content, features, functionality, and use," *CPT: Pharmacometrics & Systems Pharmacology*, vol. 4, no. 2, pp. 55–68, 2015.

[141] A. Fabregat, K. Sidiropoulos, P. Garapati, M. Gillespie, K. Hausmann, R. Haw, B. Jassal, S. Jupe, F. Korninger, S. McKay, *et al.*, "The Reactome pathway knowledgebase," *Nucleic Acids Research*, vol. 44, no. D1, pp. D481–D487, 2016.

[142] S. Placzek, I. Schomburg, A. Chang, L. Jeske, M. Ulbrich, J. Tillack, and D. Schomburg, "BRENDA in 2017: new perspectives and new tools in BRENDA," *Nucleic Acids Research*, vol. 45, no. D1, pp. D380–D388, 2016.

[143] A. Gupta and J. B. Rawlings, "Comparison of parameter estimation methods in stochastic chemical kinetic models: examples in systems biology," *AIChE Journal*, vol. 60, no. 4, pp. 1253–1268, 2014.

[144] L. A. Knodler, "*Salmonella enterica*: living a double life in epithelial cells," *Current Opinion in Microbiology*, vol. 23, pp. 23–31, 2015.

[145] S. Castanheira and F. García-del Portillo, "*Salmonella* populations inside host cells," *Frontiers in Cellular and Infection Microbiology*, vol. 7, p. 432, 2017.

[146] P. Balazki, K. Lindauer, J. Einloft, J. Ackermann, and I. Koch, "MONALISA for stochastic simulations of Petri net models of biochemical systems," *BMC Bioinformatics*, vol. 16, no. 215, pp. 1–11, 2015.

[147] R Development Core Team, *R: A Language and Environment for Statistical Computing*. R Foundation for Statistical Computing, Vienna, Austria, 2008. ISBN 3-900051-07-0.

[148] L. Amstein, J. Ackermann, J. Scheidel, S. Fulda, I. Dikic, and I. Koch, "Manatee invariants reveal functional pathways in signaling networks," *BMC Systems Biology*, vol. 11, no. 72, pp. 1–11, 2017.

[149] S. Li, M. P. Wandel, F. Li, Z. Liu, C. He, J. Wu, Y. Shi, and F. Randow, "Sterical hindrance promotes selectivity of the autophagy

cargo receptor NDP52 for the danger receptor galectin-8 in antibacterial autophagy," *Science Signaling*, vol. 6, no. 261, pp. 1–6, 2013.

[150] A. Huett, R. J. Heath, J. Begun, S. O. Sassi, L. A. Baxt, J. M. Vyas, M. B. Goldberg, and R. J. Xavier, "The LRR and RING domain protein LRSAM1 is an E3 ligase crucial for ubiquitin-dependent autophagy of intracellular *Salmonella* Typhimurium," *Cell Host & Microbe*, vol. 12, no. 6, pp. 778–790, 2012.

[151] A. C. Ng, J. M. Eisenberg, R. J. Heath, A. Huett, C. M. Robinson, G. J. Nau, and R. J. Xavier, "Human leucine-rich repeat proteins: a genome-wide bioinformatic categorization and functional analysis in innate immunity," *Proceedings of the National Academy of Sciences*, vol. 108, pp. 4631–4638, 2011.

[152] S. J. Van Wijk, E. Fiskin, M. Putyrski, F. Pampaloni, J. Hou, P. Wild, T. Kensche, H. E. Grecco, P. Bastiaens, and I. Dikic, "Fluorescence-based sensors to monitor localization and functions of linear and K63-linked ubiquitin chains in cells," *Molecular Cell*, vol. 47, no. 5, pp. 797–809, 2012.

[153] N. Fujita, E. Morita, T. Itoh, A. Tanaka, M. Nakaoka, Y. Osada, T. Umemoto, T. Saitoh, H. Nakatogawa, S. Kobayashi, *et al.*, "Recruitment of the autophagic machinery to endosomes during infection is mediated by ubiquitin," *The Journal of Cell Biology*, vol. 203, no. 1, pp. 115–128, 2013.

[154] M. Cemma, P. K. Kim, and J. H. Brumell, "The ubiquitin-binding adaptor proteins p62/SQSTM1 and NDP52 are recruited independently to bacteria-associated microdomains to target *Salmonella* to the autophagy pathway," *Autophagy*, vol. 7, no. 3, pp. 341–345, 2011.

[155] C. E. Gleason, A. Ordureau, R. Gourlay, J. S. C. Arthur, and P. Cohen, "Polyubiquitin binding to optineurin is required for optimal activation of TANK-binding kinase 1 and production of interferon β," *Journal of Biological Chemistry*, vol. 286, no. 41, pp. 35663–35674, 2011.

[156] B. Richter, D. A. Sliter, L. Herhaus, A. Stolz, C. Wang, P. Beli, G. Zaffagnini, P. Wild, S. Martens, S. A. Wagner, *et al.*, "Phosphorylation of OPTN by TBK1 enhances its binding to Ub chains and promotes selective autophagy of damaged mitochondria," *Proceedings of the National Academy of Sciences*, vol. 113, no. 15, pp. 4039–4044, 2016.

[157] N. von Muhlinen, M. Akutsu, B. J. Ravenhill, Á. Foeglein, S. Bloor, T. J. Rutherford, S. M. Freund, D. Komander, and F. Randow, "LC3C, bound selectively by a noncanonical LIR motif in NDP52, is required for antibacterial autophagy," *Molecular Cell*, vol. 48, no. 3, pp. 329–342, 2012.

[158] S. Morton, L. Hesson, M. Peggie, and P. Cohen, "Enhanced binding of TBK1 by an optineurin mutant that causes a familial form of primary open angle glaucoma," *FEBS Letters*, vol. 582, no. 6, pp. 997–1002, 2008.

[159] V. V. Rogov, H. Suzuki, E. Fiskin, P. Wild, A. Kniss, A. Rozenknop, R. Kato, M. Kawasaki, D. G. McEwan, F. Löhr, *et al.*, "Structural basis for phosphorylation-triggered autophagic clearance of *Salmonella*," *Biochemical Journal*, vol. 454, no. 3, pp. 459–466, 2013.

[160] A. L. Radtke, L. M. Delbridge, S. Balachandran, G. N. Barber, and M. X. D. O'Riordan, "TBK1 protects vacuolar integrity during intracellular bacterial infection," *PLoS Pathogens*, vol. 3, no. 3, p. e29, 2007.

[161] D. Tu, Z. Zhu, A. Y. Zhou, C.-h. Yun, K.-E. Lee, A. V. Toms, Y. Li, G. P. Dunn, E. Chan, T. Thai, *et al.*, "Structure and ubiquitination-dependent activation of TANK-binding kinase 1," *Cell Reports*, vol. 3, no. 3, pp. 747–758, 2013.

[162] X. Ma, E. Helgason, Q. T. Phung, C. L. Quan, R. S. Iyer, M. W. Lee, K. K. Bowman, M. A. Starovasnik, and E. C. Dueber, "Molecular basis of TANK-binding kinase 1 activation by transautophosphorylation,"

Proceedings of the National Academy of Sciences, vol. 109, no. 24, pp. 9378–9383, 2012.

[163] A. Larabi, J. M. Devos, S.-L. Ng, M. H. Nanao, A. Round, T. Maniatis, and D. Panne, "Crystal structure and mechanism of activation of TANK-binding kinase 1," *Cell Reports*, vol. 3, no. 3, pp. 734–746, 2013.

[164] C. Shu, B. Sankaran, C. T. Chaton, A. B. Herr, A. Mishra, J. Peng, and P. Li, "Structural insights into the functions of TBK1 in innate antimicrobial immunity," *Structure*, vol. 21, no. 7, pp. 1137–1148, 2013.

[165] E. Helgason, Q. T. Phung, and E. C. Dueber, "Recent insights into the complexity of TANK-binding kinase 1 signaling networks: the emerging role of cellular localization in the activation and substrate specificity of TBK1," *FEBS Letters*, vol. 587, no. 8, pp. 1230–1237, 2013.

[166] F. Fujita, Y. Taniguchi, T. Kato, Y. Narita, A. Furuya, T. Ogawa, H. Sakurai, T. Joh, M. Itoh, M. Delhase, *et al.*, "Identification of NAP1, a regulatory subunit of IκB kinase-related kinases that potentiates NF-κB signaling," *Molecular and Cellular Biology*, vol. 23, no. 21, pp. 7780–7793, 2003.

[167] G. Matsumoto, K. Wada, M. Okuno, M. Kurosawa, and N. Nukina, "Serine 403 phosphorylation of p62/SQSTM1 regulates selective autophagic clearance of ubiquitinated proteins," *Molecular Cell*, vol. 44, no. 2, pp. 279–289, 2011.

[168] M. Pilli, J. Arko-Mensah, M. Ponpuak, E. Roberts, S. Master, M. A. Mandell, N. Dupont, W. Ornatowski, S. Jiang, S. B. Bradfute, *et al.*, "TBK-1 promotes autophagy-mediated antimicrobial defense by controlling autophagosome maturation," *Immunity*, vol. 37, no. 2, pp. 223–234, 2012.

[169] M. T. Abreu, "Toll-like receptor signalling in the intestinal epithelium: how bacterial recognition shapes intestinal function," *Nature Reviews Immunology*, vol. 10, pp. 131–144, 2010.

[170] J.-M. Otte, E. Cario, and D. K. Podolsky, "Mechanisms of cross hyporesponsiveness to Toll-like receptor bacterial ligands in intestinal epithelial cells," *Gastroenterology*, vol. 126, no. 4, pp. 1054–1070, 2004.

[171] I. Tattoli, M. T. Sorbara, D. Vuckovic, A. Ling, F. Soares, L. A. Carneiro, C. Yang, A. Emili, D. J. Philpott, and S. E. Girardin, "Amino acid starvation induced by invasive bacterial pathogens triggers an innate host defense program," *Cell Host & Microbe*, vol. 11, no. 6, pp. 563–575, 2012.

[172] I. Tattoli, D. J. Philpott, and S. E. Girardin, "The bacterial and cellular determinants controlling the recruitment of mTOR to the *Salmonella*-containing vacuole," *Biology Open*, vol. 1, no. 12, pp. 1215–1225, 2012.

[173] N. Mizushima, "The role of the Atg1/ULK1 complex in autophagy regulation," *Current Opinion in Cell Biology*, vol. 22, no. 2, pp. 132–139, 2010.

[174] W. S. Hlavacek, J. R. Faeder, M. L. Blinov, A. S. Perelson, and B. Goldstein, "The complexity of complexes in signal transduction," *Biotechnology and Bioengineering*, vol. 84, no. 7, pp. 783–794, 2003.

[175] S. Shahnazari, W.-L. Yen, C. L. Birmingham, J. Shiu, A. Namolovan, Y. T. Zheng, K. Nakayama, D. J. Klionsky, and J. H. Brumell, "A diacylglycerol-dependent signaling pathway contributes to regulation of antibacterial autophagy," *Cell Host & Microbe*, vol. 8, no. 2, pp. 137–146, 2010.

[176] M. A. Sanjuan, C. P. Dillon, S. W. Tait, S. Moshiach, F. Dorsey, S. Connell, M. Komatsu, K. Tanaka, J. L. Cleveland, S. Withoff, *et al.*, "Toll-like receptor signalling in macrophages links the autophagy pathway to phagocytosis," *Nature*, vol. 450, pp. 1253–1257, 2007.

[177] J. Martinez, J. Almendinger, A. Oberst, R. Ness, C. P. Dillon, P. Fitzgerald, M. O. Hengartner, and D. R. Green, "Microtubule-associated protein 1 light chain 3 alpha (LC3)-associated phagocytosis is required for the efficient clearance of dead cells," *Proceedings of*

the National Academy of Sciences, vol. 108, no. 42, pp. 17396–17401, 2011.

[178] D. A. Tumbarello, P. T. Manna, M. Allen, M. Bycroft, S. D. Arden, J. Kendrick-Jones, and F. Buss, "The autophagy receptor TAX1BP1 and the molecular motor myosin VI are required for clearance of *Salmonella* Typhimurium by autophagy," *PLoS Pathogens*, vol. 12, no. 1, p. e1005174, 2015.

[179] M. Polajnar, M. S. Dietz, M. Heilemann, and C. Behrends, "Expanding the host cell ubiquitylation machinery targeting cytosolic *Salmonella*," *EMBO Reports*, vol. 18, pp. 1572–1585, 2017.

[180] J. Noad, A. von der Malsburg, C. Pathe, M. A. Michel, D. Komander, and F. Randow, "LUBAC-synthesized linear ubiquitin chains restrict cytosol-invading bacteria by activating autophagy and NF-κB," *Nature Microbiology*, vol. 2, no. 17063, 2017.

[181] S. J. van Wijk, F. Fricke, L. Herhaus, J. Gupta, K. Hötte, F. Pampaloni, P. Grumati, M. Kaulich, Y. Sou, M. Komatsu, *et al.*, "Linear ubiquitination of cytosolic *Salmonella* Typhimurium activates NF-κB and restricts bacterial proliferation," *Nature Microbiology*, vol. 2, no. 17066, 2017.

[182] R. Ganesan, N. J. Hos, S. Gutierrez, J. Fischer, J. M. Stepek, E. Daglidu, M. Krönke, and N. Robinson, "*Salmonella* Typhimurium disrupts Sirt1/AMPK checkpoint control of mTOR to impair autophagy," *PLoS Pathogens*, vol. 13, no. 2, p. e1006227, 2017.

[183] M. Lorkowski, A. Felipe-López, C. A. Danzer, N. Hansmeier, and M. Hensel, "*Salmonella enterica* invasion of polarized epithelial cells is a highly cooperative effort," *Infection and Immunity*, vol. 82, no. 6, pp. 2657–2667, 2014.

[184] B. Misselwitz, S. K. Kreibich, S. Rout, B. Stecher, B. Periaswamy, and W.-D. Hardt, "*Salmonella enterica* serovar Typhimurium binds to HeLa cells via Fim-mediated reversible adhesion and irreversible type

three secretion system 1-mediated docking," *Infection and Immunity*, vol. 79, no. 1, pp. 330–341, 2011.

[185] X.-Z. Huang, B. Tall, W. R. Schwan, and D. J. Kopecko, "Physical limitations on *Salmonella* Typhi entry into cultured human intestinal epithelial cells," *Infection and Immunity*, vol. 66, no. 6, pp. 2928–2937, 1998.

[186] J. Kusters, G. Mulders-Kremers, C. Van Doornik, and B. Van Der Zeijst, "Effects of multiplicity of infection, bacterial protein synthesis, and growth phase on adhesion to and invasion of human cell lines by *Salmonella* Typhimurium," *Infection and Immunity*, vol. 61, no. 12, pp. 5013–5020, 1993.

[187] D. Zhou, L.-M. Chen, L. Hernandez, S. B. Shears, and J. E. Galán, "A *Salmonella* inositol polyphosphatase acts in conjunction with other bacterial effectors to promote host cell actin cytoskeleton rearrangements and bacterial internalization," *Molecular Microbiology*, vol. 39, no. 2, pp. 248–260, 2001.

[188] B. H. Yu, M. A. Croxen, A. M. Marchiando, R. B. Ferreira, K. Cadwell, L. J. Foster, and B. B. Finlay, "Autophagy facilitates *Salmonella* replication in HeLa cells," *mBio*, vol. 5, no. 2, 2014.

[189] H. Cypionka, *Grundlagen der Mikrobiologie*. Springer, 2010.

[190] M. Madigan, J. Martinko, K. Bender, D. Buckley, and D. Stahl, *Brock Biology of Microorganisms*. Pearson, 2015.

[191] L. Zhao, C. D. Kroenke, J. Song, D. Piwnica-Worms, J. J. H. Ackerman, and J. J. Neil, "Intracellular water-specific MR of microbead-adherent cells: the HeLa cell intracellular water exchange lifetime," *NMR in Biomedicine*, vol. 21, no. 2, pp. 159–164, 2008.

[192] A. Fàbrega and J. Vila, "*Salmonella enterica* serovar Typhimurium skills to succeed in the host: virulence and regulation," *Clinical Microbiology Reviews*, vol. 26, no. 2, pp. 308–341, 2013.

[193] D. Drecktrah, L. A. Knodler, D. Howe, and O. Steele-Mortimer, "*Salmonella* trafficking is defined by continuous dynamic interactions with the endolysosomal system," *Traffic*, vol. 8, no. 3, pp. 212–225, 2007.

[194] R. A. Harvey and D. R. Ferrier, *Biochemistry, Fifth Edition*. Lippincott Williams & Wilkins, 2011.

[195] R. Thomas and R. d'Ari, *Biological feedback*. CRC press, 1990.

[196] S. Börje, "Implementierung von *Mauritius maps* zur graphischen Evaluierung der Interpendenz von T-Invarianten in biochemischen Netzwerken," *Bachelor thesis*, 2017.

[197] M. Hucka, A. Finney, H. M. Sauro, H. Bolouri, J. C. Doyle, H. Kitano, A. P. Arkin, B. J. Bornstein, D. Bray, A. Cornish-Bowden, *et al.*, "The systems biology markup language (SBML): a medium for representation and exchange of biochemical network models," *Bioinformatics*, vol. 19, no. 4, pp. 524–531, 2003.

[198] S. Roch and P. H. Starke, "INA: integrated net analyzer," 1999.

[199] K. A. Fitzgerald, S. M. McWhirter, K. L. Faia, D. C. Rowe, E. Latz, D. T. Golenbock, A. J. Coyle, S.-M. Liao, and T. Maniatis, "Ikkε and TBK1 are essential components of the IRF3 signaling pathway," *Nature Immunology*, vol. 4, p. 491, 2003.

[200] H. Weidberg and Z. Elazar, "TBK1 mediates crosstalk between the innate immune response and autophagy," *Science Signaling*, vol. 4, no. 187, p. pe39, 2011.

[201] A. Takeuchi, "Electron microscope studies of experimental *Salmonella* infection. I. penetration into the intestinal epithelium by *Salmonella* Typhimurium," *The American Journal of Pathology*, vol. 50, no. 1, pp. 109–136, 1967.

[202] A. J. Müller, P. Kaiser, K. E. Dittmar, T. C. Weber, S. Haueter, K. Endt, P. Songhet, C. Zellweger, M. Kremer, H.-J. Fehling, *et al.*,

"*Salmonella* gut invasion involves TTSS-2-dependent epithelial traversal, basolateral exit, and uptake by epithelium-sampling lamina propria phagocytes," *Cell Host & Microbe*, vol. 11, no. 1, pp. 19–32, 2012.

[203] K. Ray, B. Marteyn, P. J. Sansonetti, and C. M. Tang, "Life on the inside: the intracellular lifestyle of cytosolic bacteria," *Nature Reviews Microbiology*, vol. 7, pp. 333–340, 2009.

[204] F. García-del Portillo, M. B. Zwick, K. Y. Leung, and B. B. Finlay, "*Salmonella* induces the formation of filamentous structures containing lysosomal membrane glycoproteins in epithelial cells," *Proceedings of the National Academy of Sciences*, vol. 90, no. 22, pp. 10544–10548, 1993.

[205] H. Xin, Y. Li, D. Xu, Y. Zhang, C.-H. Chen, and B. Li, "Single upconversion nanoparticle – bacterium cotrapping for single-bacterium labeling and analysis," *Small*, vol. 13, no. 14, 2017.

[206] R. C. Jansen, "Studying complex biological systems using multifactorial perturbation," *Nature Reviews Genetics*, vol. 4, pp. 145–151, 2003.

[207] G. Ryzhakov and F. Randow, "SINTBAD, a novel component of innate antiviral immunity, shares a TBK1-binding domain with NAP1 and TANK," *The EMBO Journal*, vol. 26, no. 13, pp. 3180–3190, 2007.